



DYNAMICS OF ENTANGLED POLYMER CHAIN IN A
GRID OF OBSTACLES

THE THESIS IS SUBMITTED FOR THE
DEGREE OF DOCTOR OF PHILOSOPHY

Mohamad Shukor Talib

Department of Mathematics and Statistics
School of Mathematical and Physical Sciences

Contents

Acknowledgement	vi
Declaration	vii
List of Tables	ix
List of Figures	xviii
List of Abbreviations	xix
List of Symbols	xx
Abstract	xxiii
1 Introduction	1
1.1 Introduction	1
1.2 Background	2
1.3 Motivation	4
1.4 Aim and objectives	5
1.5 Polymer chain	5
1.6 The Gaussian chain	7
1.7 The Rouse model	8

1.7.1	Normal modes	9
1.8	Mean square displacement of beads	11
1.9	Stress relaxation	12
1.9.1	Macroscopic viscosity and stress tensor	12
1.9.2	Maxwell model	13
1.9.3	Microscopic expressions for the viscosity and stress tensor	14
1.9.4	Calculation for the Rouse model	15
1.10	The tube model	16
1.10.1	Definition of the tube model	17
1.10.2	Pure reptation	19
1.10.3	Tube segment occupation function	19
1.10.4	Segmental diffusion	21
1.10.5	Bead diffusion in the tube	22
1.10.6	Contour length fluctuations	24
1.11	Outline of Thesis	26
2	The Computer Simulation Model	28
2.1	Introduction	28
2.2	Brownian dynamics model	29
2.2.1	Euler integration algorithm	30
2.2.2	Predictor-corrector integration algorithm	30
2.3	Uncrossability constraints	31
2.4	The grid model	36
2.4.1	Implementation of the Brownian dynamics integration scheme	36
2.5	The computer program: Generic Polymer Simulation	38
2.6	Discussion	39
2.6.1	Brownian dynamics step	39

2.6.2	Integration step	39
2.6.3	Number of attempts	46
2.7	Conclusions	50
3	Static analysis of the Tube	51
3.1	Introduction	51
3.2	Tube-like region	51
3.2.1	Construction of the tube-like region	52
3.2.2	Tube axis	58
3.2.3	Primitive Path	59
3.3	Probability distribution of the tube length	63
3.4	Analysis and Discussion	66
3.4.1	Probability distribution of the tube length	66
3.4.2	Mean square spatial distance	71
3.4.3	Average tube length and its fluctuations	72
3.5	Comparison with the lattice model	76
3.6	Conclusions	79
4	Dynamic Analysis of the Tube	80
4.1	Introduction	80
4.2	Tube mapping	80
4.3	Tube segment occupation function	82
4.4	Bead diffusion along the tube axis	86
4.4.1	Mean square displacement in real space	87
4.5	Results and discussions	88
4.5.1	Main results for the grid model	88
4.5.2	The tube theory predictions	90

4.5.3	Fitting with the tube theory	93
4.5.4	Bead diffusion inside the tube	95
4.6	Comparison with the tube simulation model	102
4.7	Conclusions	105
5	Conclusions	106
5.1	Conclusions	106
5.1.1	Static analysis of the tube	107
5.1.2	Dynamics analysis	107
5.2	Future directions	108
5.2.1	Other architectures of polymer	108
5.2.2	Definition of $\mu(t)$	108
5.2.3	Effects of CR	108
A	Monte Carlo simulation	110
A.1	Monte Carlo algorithm	110
A.1.1	Implementation of the Monte Carlo model	111
A.1.2	Monte Carlo step	112
B	Algorithm for tube mapping	119
B.0.1	Validation of the algorithm	124
	Bibliography	125

Acknowledgement

In the name of God, the Most Gracious and the Most Merciful. All praises to God for the strength and blessing in completing this thesis. This thesis would not have been possible without the guidance and support of many individuals. I am deeply grateful to my supervisor, Prof. Alexei Likhtman for his guidance, motivation and endless support throughout this thesis. Not forgotten, my appreciation to my co-supervisors, Dr. Jorge Ramirez and Dr. Bart Vorselaars for their effort and knowledge regarding this topic. Many thanks to my monitoring committee, Prof. Mark Matsen and Prof. Peter Grindrod. The computer simulation would not efficiently complete with help by my co-supervisors and Dr. Pawel Stasiak. I also thank to members of the Polymer Theory group, University of Reading, for simulating discussions about technical and non-technical stuffs. I'm grateful to the department secretaries for assisting me in many different ways. I am indebted to the Malaysian government and University Teknologi Malaysia who has faith in me to pursue my study. Many thanks to my friends in UK and Malaysia, were sources of laughter, joy and support. Finally, I'm forever grateful to my family, my beloved wife Nazmona Mat Ali and my son, Nazeem Sabir for your understanding, endless patience and encouragement when it was most required.

Declaration

I confirm that this is my own work and the use of material from other sources has been properly and fully acknowledged.

Mohamad Shukor Talib

University of Reading

September 2012

List of Tables

3.1	Number beads per cell for each grid sizes with $N = 128$ based on statistics of 300 chains.	62
3.2	Parameters c and β from the grid model	70
3.3	The extrapolated value of a and b_{1D} for each grid size from the tube axis and the primitive path.	75
3.4	Average number of beads per entanglement, N_e for each grid size from the tube axis and the primitive path.	76
3.5	Parameters under study	77
3.6	The product of a and b_{1D} from the tube axis and the primitive path.	79
4.1	The tube parameters obtained from fitting the simulation results with the tube theory, LM2002.	94
4.2	Extrapolated values of the tube parameters from the $g_s(t)$ and $g_{1,\text{mid}}(t)$	105
4.3	Extrapolated values of the tube parameters from the static analysis .	105
A.1	The efficiency analysis for the MC steps obtained from $N = 32$, $g' = 1$ and different sizes of the time step, Δt	116
A.2	Comparison analyses of the MC and BD simulations for $N = 32$, $g' = 1$ with $\Delta t = 0.05$ and 0.01 , respectively. t_{eff} , is the efficiency of the simulation, t_{sim} is the simulation time, τ_d is the disengagement time.	117

B.1	Elements of array eS , vertex 1, 2, 5 and 6. Consist two of tube's vertices are located in the same cell with the reference cell, i .	120
B.2	List of indices	121
B.3	The S of tube \mathbf{V}^p .	121
B.4	Mapped element of tube \mathbf{V}^p with tube \mathbf{V}^c .	122
B.5	Array S	123
B.6	Series of the mapped elements.	123
B.7	Percentage of location the unique element of cells	124

List of Figures

1.1	A large circle represents a massless bead and the connecting bond vectors are presented by the black arrows	6
1.2	The $g_{1,\text{mid}}(t)$ for the Rouse model that is normalised by $t^{1/2}$, shows a plateau region as predicted by expression 1.19. The plots are for $N = 16, 32, 64, 128$	12
1.3	The stress relaxation, $G(t)$ for the Rouse model with $N = 16, 32, 64, 128$ are shown in Fig. 1.3(a) and the scaling of $G'(\omega)$ and $G''(\omega)$ are in Fig. 1.3(b).	16
1.4	The Rouse chain and the obstacles, representing the other chains . . .	18
1.5	A schematic plot of $G(t)$ for different chain lengths as measured in entangled polymer chains.	21
1.6	Motion of bead n along the primitive path	22
1.7	The MSD of the tube segments consist of several regimes which is determined by its characteristic time.	22
2.1	Bond \mathbf{r}_i connects beads \mathbf{R}_i and \mathbf{R}_{i+1} , and line obstacle \mathbf{L}_i connects point \mathbf{l}_i and \mathbf{l}_{i+1}	32
2.2	Bead $\mathbf{R}_i(t)$ moves into a new position $\mathbf{R}'_i(t + \Delta t)$, it forms two triangles. The first triangle is constructed by $\mathbf{R}_i(t)$, $\mathbf{R}_{i-1}(t)$, $\mathbf{R}'_i(t + \Delta t)$ and the second triangle is by $\mathbf{R}_i(t)$, $\mathbf{R}_{i+1}(t)$, $\mathbf{R}'_i(t + \Delta t)$	33

2.3	The plane is constructed by the three position vectors $\mathbf{R}_i(t)$, $\mathbf{R}_{i-1}(t)$ and $\mathbf{R}'_i(t + \Delta t)$, with \mathbf{n} a normal vector of the plane. The line \mathbf{L}_i intersects with the plane at position \mathbf{p} . $\mathbf{r}_p(t)$ is a vector connecting $\mathbf{R}_{i-1}(t)$ and \mathbf{p}	34
2.4	The Rouse chain in an array of point obstacles for 2D model (2.4(a)) and the chain in 3D cubic lattice (2.4(b)).	37
2.5	A snapshot of the 3D model of the computer simulation, consisting of chain with 13 beads located in a grid, $g' = 1$	37
2.6	Average rejection rate γ_{rej} versus different sizes of time steps, Δt for $N = 20, 40, 60$ and 160 . The open symbols are for $g' = 1$ and filled for $g' = 2$. The dotted lines are the linear fitting of the data, which scale approximately with $\sqrt{\Delta t}$	40
2.7	The $d(s)$ for 4 beads distance of the free Rouse chain from the EIS and PC algorithms with $N = 16$ as a function of time steps Δt (in Fig. (a)) and Δt^2 (in Fig. (b)). The solid lines are the $d(s)$ for the Gaussian chain statistics.	41
2.8	The $G(t)$ at $t = 9.6$ of the free Rouse chain with $N = 16$ from the EIS and PC algorithms as a function of Δt (in Fig. (a)) and Δt^2 (in Fig. (b)). The solid lines are the exact values for $G(t = 9.6)$ obtained from expression 1.31.	41
2.9	The $g_{1,\text{mid}}(t)$ at $t = 8.0$ from the PC and EIS algorithms with $N = 16$ as a function of Δt (in Fig. (a)) and Δt^2 (in Fig. (b)). The solid lines are the exact values for $g_{1,\text{mid}}(t = 8.0)$ obtained from expression 1.18.	42
2.10	The $G(t)$ as a function of t with $N = 16$, $\Delta t = 0.08$ for EIS and PC.	43

2.11	The $d(s)$ for $N = 32$ and $g' = 1$ from the EIS (a) and PC (b) algorithms with different sizes of the time steps. The solid lines are the $d(s)$ for ideal random walk statistics of the chain.	44
2.12	The $d(8)$ from the EIS and PC algorithms for $N = 32$, $g' = 1$ with Δt (in Fig. (a)) and Δt^2 (in Fig. (b)).	44
2.13	The $d(3)$ from the EIS and PC algorithms with $N = 64$, $g' = 2$ as a function of Δt (in Fig. (a)) and Δt^2 (in Fig. (b)).	45
2.14	The $G(t)$ from the EIS and PC algorithms are in dotted lines and symbols, respectively. The data from $N = 32$, $g' = 1$ and different sizes of the time step, Δt . The inset shows an enlargement of the intermediate-time regions.	45
2.15	The intermediate-time regions of the $g_{1,\text{mid}}(t)$ from the EIS (in lines) and PC (in symbols) algorithms with $N = 32$, $g' = 1$ and different sizes of the time step.	46
2.16	The $d(s)$ over the s beads distance with $N = 32$, $g = 1$, $\Delta t = 0.01$ and different number of attempts N_{att} in Fig. (a). The $d(8)$ for each N_{att} as a function of time steps which obtained from Fig. (a) are in Fig. (b). The solid lines in both graphs are the $d(s)$ for Gaussian chain statistics.	47
2.17	The intermediate-time regions for the $g_{1,\text{mid}}(t)$ with $N = 32$, $g = 1$, $\Delta t = 0.01$ and different number of attempts, N_{att}	48
2.18	The $G(t)$ for $N = 32$, $g' = 1$ and $\Delta t = 0.01$ with different number of attempts, N_{att} . The inset presents an enlargement of the intermediate-time regions.	49
3.1	Definition of the tube parameters where the tube consist of three segments, $Z^s = 3$	53

3.2	Steps in constructing the tube like region.	54
3.3	(a) Determine the skipped cell. (b) bead $\mathbf{R}_{i+1}(t)$ is added at the skipped cell.	55
3.4	Flow chart of recursive middle point calculation. Firstly, two adjacent beads are copied into new variables \mathbf{R}_A and \mathbf{R}_B . Calculating the middle coordinate between \mathbf{R}_A and \mathbf{R}_B gives \mathbf{R}_{mid} and converted to grid base coordinate, $\tilde{\mathbf{V}}_{r,mid}$. If the $\tilde{\mathbf{V}}_{r,mid}$ is located in the same cell with $\tilde{\mathbf{V}}_A$, then the A variables are replaced by <i>mid</i> variables. If the checked false then if $\tilde{\mathbf{V}}_{r,mid}$ is in cell $\tilde{\mathbf{V}}_B$, then the B variables are replaced by <i>mid</i> . This process is repeated until the mid bead is located neither in $\tilde{\mathbf{V}}_A$ nor $\tilde{\mathbf{V}}_B$. Finally, the skipped bead $\mathbf{R}_{skipped}$ is added between bead \mathbf{R}_i and \mathbf{R}_{i+1} by shift bead \mathbf{R}_{i+1} into \mathbf{R}_{i+2}	56
3.5	Tube axis connected by the middle point of a tube cell with its neigh- bour. The Rouse chain is given in 3.2(a).	59
3.6	Example of adding $n_b = 3$ per tube cell. The cell is divided into n_b sub-segments (Fig. (a)). The beads are added into the sub-segments, Fig (b).	61
3.7	Primitive path of the tube. The Rouse chain is given in 3.2(a). . . .	62
3.8	The natural logarithm of the data for $P(Z^s, N)$ with $N = 512$, $g' =$ 4 , $\langle Z^s \rangle = 50.18$. The solid and dashed lines are the regions to obtain the $P(0, N)$. The dashed line is the fitting at the peak region of the distribution.	64
3.9	$P(Z = 0, N)$ as a function of N for $g' = 1$ (Fig. 3.9(a)) and $g' = 2$ (Fig. 3.9(b)). The dashed lines are the data fitting with Eq. 3.10. . .	65

3.10	Semi-log scale, normalised distribution of number of tube segments \widehat{Z}^s for $g' = 1, 2, 4, 8, 16$ with $N = 16, 64, 256, 1024, 4096$, respectively. The dashed line is the normalised Gaussian distribution. The data are based on 1×10^6 configurations.	66
3.11	Semi-log scale, normalised distribution function of the primitive path length, \widehat{L}^{PP} for $g' = 1, 2, 4$ with $N = 16, 64, 256$, respectively. The dashed line is the normalised Gaussian distribution. The data are based on 1000 configurations.	67
3.12	β^{T} and c^{T} as a function of $1/N$ for $g' = 1$ and $g' = 2$ are in 3.12(a) and 3.12(b), respectively. These are based on the tube axis statistics.	69
3.13	Parameter β from the grid and lattice model by Zheligovskaya et al as a function of $1/g'^{1/2}$. In the limit of a very large g , β in both models approximately equals to 0.6.	70
3.14	Two dimensional representation of a chain on the lattice model. The chain consist of 5 segments.	71
3.15	Mean square spatial distance of the tube axis as a function of cell separation s for various grid sizes in Fig. 3.15(a) and normalised by g^2 , in 3.15(b)	71
3.16	Natural logarithm of the data for $P(Z^s, N)$ with $N = 512$ and $g' = 4$. The solid line is the fitted region. The Gaussian parameters obtained from the fitting are $\widehat{Z}^s = 50.184$ and $\Delta\widehat{Z}^s = 10.04$	73
3.17	Tube Kuhn step for the tube axis, a^g as a function of g^2/N where the asymptotic value, $N \rightarrow \infty$ for each grid size is obtained in Fig. 3.17(a). The same procedure is applied for the $b_{1\text{D}}^g$, Fig. 3.17(b). . . .	74

3.18	Kuhn step for the primitive path, a^{PP} as a function of g^2/N where the asymptotic value, $N \rightarrow \infty$ for each grid size is obtained in Fig. 3.18(a). The same procedure is applied for b_{1D}^{PP} , Fig. 3.18(b).	74
3.19	The Kuhn segment length from the tube axis, a^g and the primitive path, a^{PP} normalised by g' as a function of g' are in Fig. 3.19(a). The ratio of these Kuhn segments versus $1/g$ is shown in Fig. 3.19(b). . .	75
3.20	The extrapolate value for b_{1D}^g and b_{1D}^{PP} in Fig. 3.20(a) and 3.20(b), respectively.	76
3.21	Tube Kuhn step normalised by g from the grid and the lattice models as a function $1/g^{1/2}$ in Fig. 3.21(a). b_{1D} from the models show they approximately scale with $g^{1/4}$ in Fig. 3.21(b).	78
4.1	Living time of cells for $Z^s=10, 20$ and 30 , grid=1	81
4.2	Steps in calculating $\mu(t)$ where t_i^c and t_i^l are the creation time and living time for cell i respectively.	83
4.3	The $\mu(t)$ for $g' = 1$ with $N = 16, 32, 64, 128$ in symbols, whereas $g' = 2$ is shown in solid lines for $N = 32, 64, 128, 256$ and the dashed lines are for $g' = 4$ with $N = 64, 128, 256, 512$. Fig. 4.3(b) shows the normalised derivative of $\mu(t)$ for g' and N as in Fig. 4.3(a), while for $g' = 4$, the chain lengths are $N = 128$ and 256	85
4.4	Main results for the grid model. Symbols correspond to $g = 1$ with $N = 16, 32, 64, 128$, lines for $g = 2$ with $N = 32, 64, 128, 256$ and the dotted lines for $g' = 4$ with $N = 64, 128, 256, 512$	89

4.5	Diffusion coefficient in 3D space, D_{3D} normalised by N^2 as a function of N/g'^2 for $g' = 1, 2$ and 4 in Fig. 4.5(a). The normalised disengagement time, τ_d by N^3 which is obtained from $G(t)$, $\Phi(t)$ and $\mu(t)$ for $g' = 1, 2, 4$ and the dashed lines are the Rouse time, τ_R for each grid size are shown in Fig. 4.5(b).	90
4.6	Normalised derivative of the end-to-end vector relaxation function, $-Nt^{3/4}\Phi(t)'$ for different g' and N	91
4.7	The vertically shifted $G(t)$ until they collapse upon $\mu(t)$ and $\Phi(t)$ for $g' = 2$ with $N = 32, 64, 128, 256$	92
4.8	Ratio between τ_d from $\Phi(t)$ and $G(t)$ and τ_d from $\mu(t)$ in Fig. 4.8(a). The normalised disengagement time, τ_d by N^3 for $\mu(t)$ which are obtained by using the Maxwell modes and calculate the gradient of the semi-log plot in Fig. 4.8(b).	92
4.9	The $G'(\omega)$ and $G''(\omega)$ from the simulation results (symbols) and the tube theory, LM2002 (symbols) for $g' = 2$ with $N = 32, 64, 128, 256$	94
4.10	The normalised $g_s(t)$ by $t^{1/2}$ for $g' = 1$ with $N = 32, 64, 128$ are presented in solid lines, whereas the dashed lines for $g = 2$ with $N = 64, 128, 256$ and symbols for $g' = 4$ with $N = 128$ are shown in Fig. 4.10(a). The $g_{1,\text{mid}}(t)$ are based on the continuous (lines) and discrete (symbols) coordinate of the beads for $N = 16, 64$ and 256 for free Rouse chain is shown in Fig.4.10(b).	96
4.11	The time normalised by τ_R for $g' = 1$ and 2 are shown in Figs 4.11(a) and 4.11(b), respectively. The chain lengths are the same as shown in Fig. 4.10(a).	96
4.12	The normalised $g_{1,\text{mid}}(t)$ by $t^{1/4}$ from the simulation results (symbols) and predicted by Eq. 4.10 (dashed lines) for $g' = 1$ and $g' = 2$	97

4.13	The $g_{1,\text{mid}}(t)$ and $\sqrt{2/\pi g_s(t)}$ for $g' = 1$ and $g' = 2$ are shown in Figs. 4.13(a) and 4.13(c). The vertical shifted of the $a\sqrt{2/\pi g_s(t)}$ in both grid sizes are shown in Figs. 4.13(b) and 4.13(d).	98
4.14	The tube Kuhn step, a which obtained from the tube axis and dynamics fitting (as in Fig. 4.13) for $g' = 1$ and 2.	99
4.15	ab_{1D} obtained from the tube axis, primitive path and dynamics fitting for $g' = 1, 2$ and 4. The extrapolated ab_{1D} from Figs. (a), (b) and (c) as a function of g' are shown in Fig. 4.15(d).	100
4.16	ζ_{1D} for $g' = 1, 2$ and 4 as a function of $(g')^2/N$ (Fig. 4.16(a)) and the extrapolated ζ_{1D} for each grid size is shown in Fig. 4.16(b). . . .	101
4.17	The ratio between the $\tau_{R,1D}$ from the tube axis and τ_R for each grid size as a function of $(g')^2/N$ is shown in Fig. 4.17(a). The extrapolated value of the ratio is presented in Fig. 4.17(b)	101
4.18	Diffusion coefficient of the 1D Rouse motion normalised by the chain length, N as a function of N/g'^2 . The dotted lines are the $1/\zeta_{1D}$ from the tube axis	102
4.19	The comparison between the grid model (symbols) for $g' = 2$ with $N = 64, 128, 256$ and 512 and the tube simulation model (solid lines) where the input parameters are $a = 4.812, b_{1D} = 0.833, \zeta_{1D} = 3.964$	104
A.1	The stress relaxation modulus, $G(t)$ from the Monte Carlo with $N = 32, g = 1$ and different sizes of the time step, Δt . The solid line and filled symbol (in the inset) are obtained from the Brownian dynamics simulation with the same parameters as in the Monte Carlo and $\Delta t = 0.01$	113

A.2	The $G(t)$ at $t = 32$ from the Monte Carlo and Brownian dynamics with $N = 32$, $g' = 1$ as a function of $\sqrt{\Delta t}$ is shown in Fig. A.2(a). Fig. A.2(b) shows the horizontal shifted of the $G(t)$ in Fig. A.1 until they collapse upon each other.	113
A.3	The mean square displacement of the middle bead, $g_{1,\text{mid}}(t)$ from the MC simulation with $N = 32$, $g' = 1$ and different sizes of the time step, Δt . The inset presents the $g_{1,\text{mid}}(t)$ at $t = 32$ as a function of \sqrt{t} . The solid line and filled symbol (in the inset) are obtained from the Brownian dynamics simulation with the same parameters as in the Monte Carlo and $\Delta t = 0.01$	114
A.4	The $\Phi(t)$ from the Monte Carlo with $N = 32$, $g' = 1$ and various time steps as indicated in the legend. The inset shows the $\Phi(t)$ at $t = 32$ over the Δt . The solid line and filled symbol (in the inset) are the data from the Brownian dynamics with the same parameters as in the Monte Carlo and $\Delta t = 0.01$	115
B.1	Two dimensional view, the previous time step tube \mathbf{V}^p is denoted by a dotted line and the current tube \mathbf{V}^c by a dashed line. The circles show the index of cells for these tubes.	120
B.2	Tube configuration, where the dashed line is the \mathbf{V}^p and dotted line is the \mathbf{V}^c	122

List of Abbreviations

SDE	Stochastic differential equation
MS	Mean square
RMS	Root-mean-square
CR	Constraint release
CLF	Contour length fluctuations
GPS	Generic Polymer Simulation
MC	Monte Carlo
BD	Brownian dynamcis
EIS	Euler integration steps
PC	Predictor-corrector

List of Symbols

ζ_{1D}	friction coefficient of bead inside a tube
b_{1D}	chain statistical segment length
g	grid spacing
N	number of bonds of a chain
\mathbf{R}_n	position vector of the n -th bead
\mathbf{r}_n	bond vector of the n -th bead
$R_{n,\alpha}$	α component of the position vector of bead n
$r_{n,\alpha}$	α component of the bond vector n
\mathbf{R}_e	end-to-end vector
l_k	Kuhn length of a freely-jointed chain
L_c	countour length of a freely-jointed chain
$d(s)$	MS internal distance of beads
b_{3D}	Kuhn length a chain
k	harmonic spring constant
k_B	Boltzmann's constant
T	absolute temperature
ζ_{3D}	friction coefficient
\mathbf{f}_i	random force acting on bead i
\mathbf{X}_p	normal mode p

τ_R	Rouse time
τ_p	relaxation time of the p -th mode
$g_{1,\text{mid}}(t)$	MS displacement of the middle bead
$G(t)$	stress relaxation modulus
$\sigma_{\alpha\beta}$	stress tensor on cartesian component
τ_e	Rouse time of an entanglement strand
N_k	number of Kuhn monomers on a freely-jointed chain
L	contour length of the primitive path
a	tube Kuhn length
Z	tube Kuhn segments
N_e	number of beads per entanglement
ζ_{3D}	friction coefficient
$\mu(t)$	tube segment occupation function
τ_d^0	disengagement time without CLF
$\Phi(t)$	end-to-end relaxation function
g_s	one-dimensional MSD of the middle bead along the tube axis
ζ_{1D}	friction coefficient in one dimensional space
$\tau_{R,1D}$	Rouse time in one dimensional space
\mathbf{V}	position vector of the i -th tube vertex
τ_d	disengagement time with CLF
g'	grid spacing in dimensionless unit
Δt	size of the integration steps
N_{att}	number of attempts for the uncrossability constraints
Z^s	number of tube segments
\mathbf{v}	vector connection two consecutive tube vertices
$\tilde{\mathbf{V}}$	position vector (in integer) of the i -th tube vertex

L_g	contour length of the tube axis
$\Delta\widehat{Z}^s$	variation length of the tube axis
a^g	tube Kuhn length of the tube axis
b_{1D}^g	chain statistical segment length inside tube of the tube axis
N_e^g	number of beads per entanglement of the tube axis
L^{pp}	contour length of the primitive path
a^{pp}	tube Kuhn length of the primitive path
b_{1D}^{pp}	chain statistical segment length inside tube of the primitive path
N_e^{pp}	number of beads per entanglement of the tube axis
t_i^c	creation time for tube cell i
t_i^l	living time for tube cell i
$\tilde{\mu}(t)$	derivative of the $\mu(t)$
D_{3D}	diffusion coefficient in three dimensional space
D_{1D}	diffusion coefficient inside the tube

Abstract

Entanglements contribute to fascinating properties of polymers such as viscoelasticity and memory. The most successful model for treating entangled polymers is the reptation/tube model. Most of the theoretical approaches are based on this model. Nevertheless, some basic assumptions of the tube theory lack a microscopic foundation. In this project, we are interested to find out if the tube theory can adequately describe our simulation model, whether the tube theory has to be modified accordingly, and how to find the parameters of the tube. The model is a Brownian dynamics simulation of a single chain in an array of obstacles, a grid. The intrachain interactions are described by the Rouse model and a non-crossability algorithm is used to prevent the chain from crossing the grid, thereby preserving the topological constraints. This allows us to study the well entangled systems as compared to melt simulations. The predictor-corrector algorithm is implemented in the computer simulation. The simulation preserves the Gaussian statistics of the chains at all time and length scales. The tube parameters in this model, a , b_{1D} and ζ_{1D} are determined by several methods and compared with the assumptions of the tube theory.

Chapter 1

Introduction

1.1 Introduction

A polymer is a molecule that is composed of repeated structural units, called monomers, which are connected by covalent chemical bonds. A molecule can consist of hundreds and millions of monomers. Polyethylene, for example, is a long polymer chain which is formed by synthesizing up to 10^5 ethylene ($\text{CH}_2 = \text{CH}_2$) monomers [1].

In manufacturing polymeric materials and commodities, the polymer melts are subjected to flow. A polymer chain can be considered as a chain of springs and in such a flow it can stretch, thereby giving rise to the elastic behaviour of the polymeric fluid. When the polymer molecules overlap sufficiently and are long enough, they get entangled with each other [2]. This constrains their movement and the material leading to viscoelastic behaviour. The characteristic of the polymer dynamics such as relaxation time and the stress of the material are also affected by type and size of the polymers. Many experiments, computer simulations and theories are trying to predict these properties.

One of the purposes of computer simulations is that it can bridge the gap between experimental and theoretical investigations. It also provides a direct connection between a microscopic model and the observation of experimental quantities [3]. In addition, with the current development of computer technology, computer simulations can simulate longer chains and time scales. In this project, we use a computer simulation of a polymer model and study the predictions of the existing theories of polymer melts.

1.2 Background

Numerous experiments were conducted to study various static and dynamic properties of polymer chains [4–8]. However, up to now no experiment is able to study directly the microscopic origin of the effects occurring at macroscale [3]. For this reason, theories and computer simulations can be used to understand the polymer properties.

The viscoelastic properties of polymers are unusual and difficult to model. Some properties arise because of topological interactions that exist between long polymer chains. These interactions are caused by the fact that chains cannot cross each other, but are entangled instead. The successful mathematical description for entanglement is the tube model developed by Edwards. De Gennes introduced ‘reptation’, the motion of a chain within the confining tube [9–12]. The original tube theory is simple and has managed to predict some experimental observables, however, it is not quantitatively valid for mildly entangled polymers [13]. The tube theory was updated by introducing a tube’s contour length fluctuations (CLF) and constraint release (CR). These mechanisms require more microscopic foundations of the tube which are lacking in the original theory [14]. The characteristics of the tube model

include:

1. The tube model is mean-field approach, coarse grained [15].
2. The tube theory assumes that, at long time and for very entangled chains, the chain inside the tube moves in one dimension along the tube contour [13].
3. There is no detailed information about the chain inside the tube.
4. Some numerical tube parameters are assumed to be unity, for example the ratio of the tube diameter to the tube Kuhn length [14].
5. The tube diameter and the number of beads per tube segment are constant with time.

In addition, the questions regarding the tube theory relevant to this study are:

1. Currently, different experiments or simulations lead to different values of tube diameter [13, 15]. How to obtain the universal tube parameters?
2. How to map the 3D motion of the chain onto its 1D motion inside the tube?
3. Are the chain parameters inside the tube (such as the effective one dimensional friction (ζ_{1D}) and the chain statistical segment length (b_{1D})) equal to the unentangled chain?

The microscopic properties of the tube theory can be examined by using a computer simulation. The models can either use coarse graining of the chains and maintain information about the entanglements or use a one-chain model. In this study, we focus only on the one-chain model.

In the tube theory, the tube length is defined as the primitive path. However, this definition is unclear (see section 3.2, for discussion). The method for generating

primitive path follows essentially the idea by Edwards in identifying the shortest path for each chain without violating the topological constraints. Some well known algorithms have been developed to determine the primitive path. These include ‘annealing’ method, lattice Monte Carlo with adapting annealing method, shortest multiple disconnected path approach (Z-code) [16–20] and the contour reduction topological analysis approach (CReTA) [20–22]. However, these methods are complex and sometimes their results are inconsistent.

In order to represent the entanglement, we require uncrossability algorithm to prevent the chain from crossing the constraint. Briels and collaborators have proposed the TWENTANGLEMENT algorithm whereby the bond is allowed to bend between the bonded beads [23,24]. This approach introduces a lot of computational overhead [22]. Larson and co-workers use a different approach, by computing the distance between two bonds and imposing a short-range repulsive force as a function of this distance [25–27]. A smaller time step is required to prevent the beads from being pushed far away from the remainder of the chains when they become too close to each other [25]. In this project, we use a simple optimised geometry algorithm and implement a step potential which we hope will speed-up the simulation and allow us to study longer chains.

1.3 Motivation

In order to study microscopic properties of the tube theory, we have developed a simple computer simulation. The simulation is simple because it is based on a single chain model, with the Rouse chain inside stationary constraints. The constraints have zero volume and are modelled by a regular array of cubic lattice obstacles (in three-dimensional case). It would be interesting to study the details of the theory

which are addressed in section 1.2 by using this simple model.

The advantage of this model is that only one extra parameter is introduced, namely the grid spacing, g . The contour length fluctuations (CLF) and longitudinal relaxation due to redistribution of beads inside the tube are presented naturally in this model. More complex polymer architectures such as branched polymers are easily incorporated and no extra parameters are needed to be introduced.

1.4 Aim and objectives

The aim of this project is to find clear evidence of the static and dynamic properties of the tube from a more microscopic origin by means of computer simulations. Once established, we want to find out if the tube theory can adequately describe our simulation model, whether it needs to be modified to describe our model and how to find the parameters of the tube.

The detailed objectives of this project are:

1. To develop a computer simulation of entangled polymer chains by using a single chain model and implement an uncrossability check.
2. To obtain the tube parameters by using static and dynamic analysis of the linear chain and to establish a mapping between the tube and the grid model.
3. To observe the contributions of the tube parameters towards the static and dynamic properties of the entangled chain.

1.5 Polymer chain

At a molecular scale, a polymer chain is formed by connecting monomers with each other via a chemical bond, usually of covalent nature. The bond orientations are

different for each monomer unit. However, if the chain is divided into N subchains of a uniform λ number of monomers with $\lambda \gg 1$, then vectors \mathbf{r}_i connecting two consecutive junction points become independent from each other (see Fig. 1.1) [28, 29]. The junction points are presented as massless beads of $\{\mathbf{R}_i\} = (\mathbf{R}_0, \dots, \mathbf{R}_{N+1})$

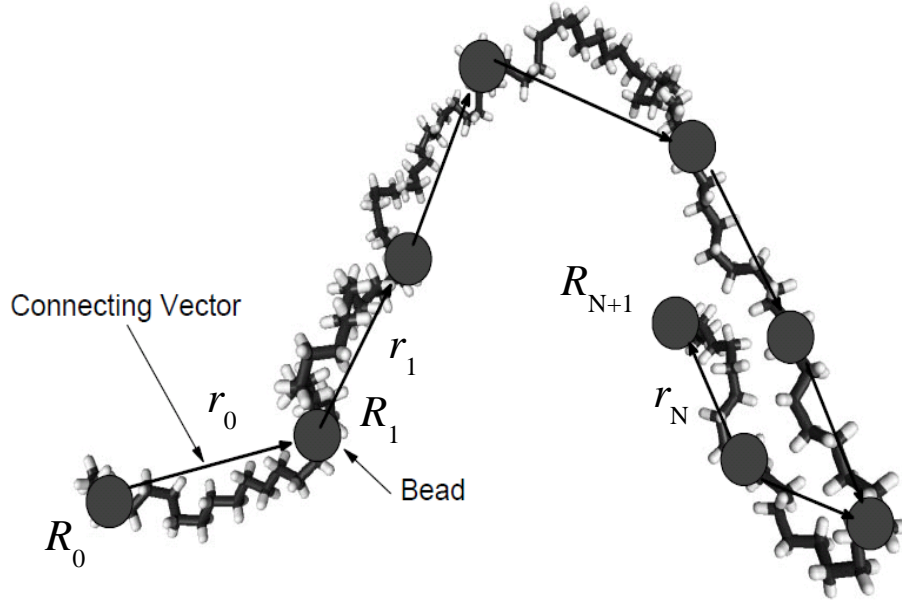


Figure 1.1: A large circle represents a massless bead and the connecting bond vectors are presented by the black arrows

and the bond vectors are $\{\mathbf{r}_i\} = (\mathbf{r}_0, \dots, \mathbf{r}_N)$. The average end-to-end vector of the chain $\langle \mathbf{R}_e \rangle$ is given by [1, Eq. 5.5]:

$$\langle \mathbf{R}_e \rangle = \langle \mathbf{R}_N - \mathbf{R}_0 \rangle \quad (1.1a)$$

$$= \sum_{i=0}^{N-1} \langle \mathbf{r}_i \rangle \quad (1.1b)$$

The $\langle \mathbf{R}_e \rangle$ in Eq. 1.1b is zero because of the isotropic properties of the chain. Thus the chain size can be estimated by:

$$\widehat{\mathbf{R}}_e = \langle \mathbf{R}_e^2 \rangle^{1/2} \quad (1.2)$$

where $\langle \mathbf{R}_e^2 \rangle = \sum_{i,j=0}^{N-1} \langle \mathbf{r}_i \cdot \mathbf{r}_j \rangle$ and $\langle \mathbf{r}_i \cdot \mathbf{r}_j \rangle = \langle |\mathbf{r}_i^2| \rangle \delta_{ij}$ where $\delta_{ij} = 1$ if $i = j$ and $\delta_{ij} = 0$ otherwise, thus

$$\langle \mathbf{R}_e^2 \rangle = N \langle |\mathbf{r}_i^2| \rangle \quad (1.3)$$

The average root-mean square (RMS) bond vector b_{3D} is defined as:

$$b_{3D} = \langle |\mathbf{r}_i^2| \rangle^{1/2} \quad (1.4)$$

thus

$$\widehat{\mathbf{R}}_e = \sqrt{N} b_{3D} \quad (1.5)$$

The ensemble average $\langle \dots \rangle$, is averaging either many different chains or over all the possible conformations of one chain. Eq. 1.5 shows that the size of the chain depends on the b_{3D} . The definition of Kuhn length is [1, 30]

$$l_k = \frac{\langle \mathbf{R}_e^2 \rangle}{L_c} \quad (1.6)$$

where L_c is the contour length of the chain. If we assume that $L_c = N b_{3D}$, then $l_k = b_{3D}$.

1.6 The Gaussian chain

On a global level, a polymer chain can be modelled by a Gaussian chain. If λ (in section 1.5) is large enough, then the distance between two consecutive beads is

Gaussian distributed and the λ monomers can be presented by a harmonic spring with spring constant, $k = \frac{3k_B T}{b_{3D}^2}$ with k_B is Boltzmann's constant and T is the absolute temperature. The prefactor of the constant is chosen so that the average square of the bond length is $\langle (\mathbf{R}_{i+1} - \mathbf{R}_i)^2 \rangle = b_{3D}^2$, when in thermal equilibrium. One of the main properties of the Gaussian chain is that the average square distance for any two beads i and j along the chain can be expressed as [31, Eq.1.31]:

$$\langle (\mathbf{R}_i - \mathbf{R}_j)^2 \rangle = |i - j| b_{3D}^2 \quad (1.7)$$

from Eq. 1.7, we introduce a function [32]

$$d(s) = \frac{1}{N - s + 1} \sum_{i=0}^{N-s} \frac{\langle (\mathbf{R}_{i+s} - \mathbf{R}_i)^2 \rangle}{s} \quad (1.8)$$

where s is the chemical distance, $|i - j|$. For the Gaussian chain, function $d(s)$ is constant and equals to b_{3D}^2 .

Although the Gaussian chain is easy to solve analytically as compared to other models, it only describes the statics of polymer chains. This project also involves the dynamics of polymer chains, thus another suitable model is required.

1.7 The Rouse model

The dynamics of the polymer chain can be modelled by the Rouse model [33]. The properties of the model are [9, 34]:

1. A Gaussian chain, where the bonded force on bead \mathbf{R}_i is the total forces from its neighbours in the same chain. This local potential is assuming that the excluded volume interactions are screened out.
2. Brownian motion. When a bead moves in a solvent, it will feel friction forces

and random forces due to collisions with the solvent molecules. These forces contribute to the random dynamics of the beads similar to the Brownian motion. In a solvent, hydrodynamic interactions are also present but in a melt of chains they are mostly screened out [35, 36].

The stochastic differential equations (SDE) for each bead along the Rouse chain is

$$\zeta_{3D} \frac{d\mathbf{R}_0}{dt} = \frac{3k_B T}{b_{3D}^2} (\mathbf{R}_1 - \mathbf{R}_0) + \mathbf{f}_0(t), \quad \text{if } i = 0 \quad (1.9a)$$

$$\zeta_{3D} \frac{d\mathbf{R}_i}{dt} = \frac{3k_B T}{b_{3D}^2} (\mathbf{R}_{i-1} - 2\mathbf{R}_i + \mathbf{R}_{i+1}) + \mathbf{f}_i(t), \quad \text{if } 0 < i < N \quad (1.9b)$$

$$\zeta_{3D} \frac{d\mathbf{R}_N}{dt} = \frac{3k_B T}{b_{3D}^2} (\mathbf{R}_{N-1} - \mathbf{R}_N) + \mathbf{f}_N(t), \quad \text{if } i = N \quad (1.9c)$$

The relation between the random forces and the friction coefficient is given by the fluctuation-dissipation theorem which leads to the expression:

$$\langle \mathbf{f}_{i,\alpha}(t) \mathbf{f}_{j,\beta}(t') \rangle = 2k_B T \zeta_{3D} \delta_{ij} \delta_{\alpha\beta} \delta(t - t') \quad (1.10)$$

With α, β being the Cartesian coordinates. We also neglected any inertial effects. These equations (eqs. 1.9a, 1.9b and 1.9c) can be analytically solved by using normal modes.

1.7.1 Normal modes

The normal modes describe the relative segment motion of the Rouse chain and are associated with the internal motion of the chain. The Cartesian coordinate of the beads can be transformed into a normal coordinate by

$$\mathbf{X}_p = \frac{1}{N+1} \sum_{i=0}^N \mathbf{R}_i \cos\left(\frac{\pi p (i + \frac{1}{2})}{N+1}\right) \quad p = 0, 1, \dots \quad (1.11)$$

The backward transformation of Eq. 1.11 is given as:

$$\mathbf{R}_i = \mathbf{X}_0 + 2 \sum_{p=1}^N \mathbf{X}_p \cos \left(\frac{\pi p(i + 1/2)}{N + 1} \right) \quad (1.12)$$

Eqs. 1.9a, 1.9b and 1.9c in normal modes is

$$\zeta_{3D}^p \frac{\partial \mathbf{X}_p}{\partial t} = -k_p \mathbf{X}_p + \mathbf{f}_p \quad (1.13)$$

With $\langle \mathbf{f}_{p,\alpha}(t) \mathbf{f}_{q,\beta}(t') \rangle = 2k_B T \zeta_{3D}^p \delta_{pq} \delta_{\alpha\beta} \delta(t - t')$, where $\zeta_{3D}^p = 2(N + 1)\zeta_{3D}$ and $k_p = \frac{24k_B T(N+1)}{b_{3D}^2} \sin^2 \left(\frac{\pi p}{2(N+1)} \right)$. The dynamics of the mode is independent from each other with its relaxation time τ_p . The zeroth mode, $p = 0$ represent the motion of the centre of mass of the chain. It will be treated differently, where $\zeta_{3D}^0 = (N + 1)\zeta_{3D}$ and $k_0 = 0$. The τ_p for other modes are given as:

$$\tau_p = \frac{\zeta_{3D}^p}{k_p} = \frac{\zeta_{3D} b_{3D}^2}{12k_B T} \sin^{-2} \left(\frac{\pi p}{2(N + 1)} \right) \quad p = 1, 2, \dots, N \quad (1.14)$$

The longest relaxation time, occurring at $p = 1$, is known as the Rouse time, a characteristic time when the polymer molecule diffuses a distance of order of its size [30]:

$$\tau_R \equiv \tau_1 = \frac{\zeta_{3D} b_{3D}^2}{12k_B T} \sin^{-2} \left(\frac{\pi}{2(N + 1)} \right) \quad (1.15a)$$

$$\approx \frac{\zeta_{3D} b_{3D}^2 N^2}{3\pi^2 k_B T}, \quad \text{for } N \gg 1 \quad (1.15b)$$

The shortest relaxation time

$$\tau_N = \frac{\zeta_{3D} b_{3D}^2}{12k_B T} \sin^{-2} \left(\frac{\pi N}{2(N + 1)} \right) \approx \frac{\zeta_{3D} b_{3D}^2}{12k_B T} \quad (1.16)$$

which approximately 2.5 times larger than

$$\tau_0 = \frac{\zeta_{3D} b_{3D}^2}{3\pi^2 k_B T} \quad (1.17)$$

In the following sections, all the measurable properties will be given in general terms of normal mode amplitudes and will be evaluated explicitly for the Rouse model. In the following calculations and computer simulations, we used unit of dimension where $k_B T = 1$, $b_{3D} = 1$ and $\zeta_{3D} = 1$.

1.8 Mean square displacement of beads

A useful quantity traditionally measured in molecular dynamics is the monomer mean square displacement, $g_1(t)$. In this project, we studied the mean squared displacement of the middle bead, $g_{1,\text{mid}}(t)$, because its analytical treatment is quite simple compared to other beads along the chain and it reduces the chain ends effects of the bead's motion [37]. The $g_{1,\text{mid}}(t)$ is defined as $g_{1,\text{mid}}(t) \equiv \langle (\mathbf{R}_{N/2}(t) - \mathbf{R}_{N/2}(0))^2 \rangle$ and its analytical expression is [9]

$$g_{1,\text{mid}} = \frac{6k_B T}{(N+1)\zeta_{3D}} t + \frac{b_{3D}^2}{N+1} \sum_{p=2,\text{even}}^N \sin^{-2} \left(\frac{\pi p}{2(N+1)} \right) \left[1 - \exp \left(-\frac{t}{\tau_p} \right) \right] \quad (1.18)$$

In the limit of a very long chain, $N \gg 1$, $g_{1,\text{mid}}(t)$ shows three regimes. The first regime occurs at very short times, $t < \tau_N$ and depends on microscopic details of its potentials. The second and third regimes are universal and depend on the τ_R and the chain length which is shown in Fig. 1.2 for $N = 16, 32, 64$ and 128 :

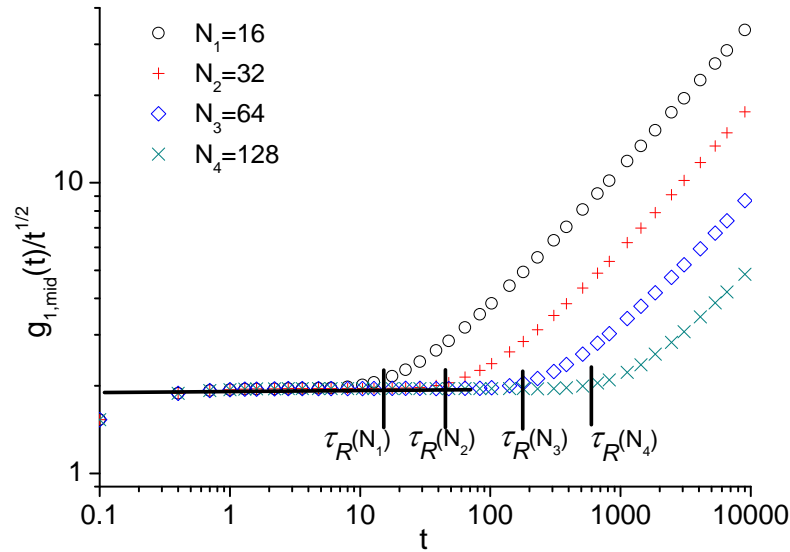


Figure 1.2: The $g_{1,\text{mid}}(t)$ for the Rouse model that is normalised by $t^{1/2}$, shows a plateau region as predicted by expression 1.19. The plots are for $N = 16, 32, 64, 128$.

$$g_{1,\text{mid}}(t) \approx \begin{cases} \frac{6k_B T}{\zeta_{3D}} t, & t \leq \tau_N \\ 2b_{3D}^2 \sqrt{\frac{3t}{\pi}}, & \tau_N \leq t \leq \tau_R \\ \frac{6k_B T}{(N+1)\zeta_{3D}} t, & t \geq \tau_R \end{cases} \quad (1.19)$$

1.9 Stress relaxation

1.9.1 Macroscopic viscosity and stress tensor

The viscoelastic behaviour of a polymer melt can be examined in two different ways; the linear or the non-linear regime [38]. In this study, we limit our study to the linear regime only. For small enough deformation (infinitesimal deformation) or sufficiently slow rate (infinitesimal rate of deformation) the response of the subsystem is linear and causal. Linear means the response to two arbitrary perturbations are linear superpositions of the individual responses (Boltzmann's superposition principle) and

the causal means the current response (the observable at actual time t) is only influenced by the shear in the past t' , $t' \leq t$.

In a stepwise shear experiment, the polymer is initially at rest and at time $t = 0$ is given a small strain γ_0 . The ratio of the shear stress σ and the γ_0 is given by the stress relaxation $G(t)$ as follows:

$$G(t) = \frac{\sigma(t)}{\gamma_0} \quad (1.20)$$

Another experiment is by using a small sinusoidal deformations with the angular frequency, ω which measures the steady state response of the material. The measured properties are the dynamic storage $G'(\omega)$ and the loss modulus $G''(\omega)$. Their relationship with $G(t)$ are [39]

$$G'(\omega) = \omega \int_0^\infty G(t) \sin(\omega t) dt \quad (1.21)$$

$$G''(\omega) = \omega \int_0^\infty G(t) \cos(\omega t) dt \quad (1.22)$$

1.9.2 Maxwell model

The Maxwell model is a mechanical model for viscoelastic materials. In this model, a transient deformation $\gamma(t)$ applied to a material is distributed between the deformation of the elastic $\gamma_e(t)$ and viscous elements $\gamma_v(t)$:

$$\gamma(t) = \gamma_e(t) + \gamma_v(t) \quad (1.23)$$

In the Maxwell model, $G(t)$ in the shear experiment has a simple exponential decay of

$$G(t) = G_0 \exp\left(-\frac{t}{\tau}\right) \quad (1.24)$$

with τ the relaxation time of the viscoelastic liquid. The $G(t = 0)$, denoted by G_0 is known as the instantaneous modulus. In practice, a material can often be described by sum of individual Maxwell modes [2]:

$$G(t) = \sum_i^m G_i \exp\left(-\frac{t}{\tau_i}\right) \quad (1.25)$$

where G_i and τ_i are the amplitude and the relaxation time of the mode number i where m is the maximum number of Maxwell modes.

1.9.3 Microscopic expressions for the viscosity and stress tensor

The stress tensor $\sigma_{\alpha\beta}$ of the molecular model is defined as [9, Eq. 3.134]:

$$\sigma_{\alpha\beta} = -\frac{1}{V} \sum_{i=0}^N \langle \mathbf{R}_i^\alpha \mathbf{F}_i^\beta \rangle \quad (1.26)$$

where \mathbf{F}_i is the total force acting on bead i and V is the volume in which the σ is calculated and the Greek indices denote their Cartesian components.

In this project, we do not apply any deformation and the $G(t)$ is determined by using the fluctuation-dissipation theorem. The fluctuations that occur naturally in the Rouse model can be used to evaluate the stress relaxation. The fluctuation-dissipation theorem relates the shear relaxation to a time correlation of the stress tensor [24, 35]:

$$G(t) = \frac{V}{k_B T} \langle \sigma_{xy}(t + \tau) \sigma_{xy}(\tau) \rangle \quad (1.27)$$

1.9.4 Calculation for the Rouse model

Referring to definition of the stress tensor Eq. 1.26 and the normal modes Eq. 1.12, we obtained:

$$\sigma_{\alpha\beta} = \frac{3k_B T}{V b_{3D}^2} \sum_{i=0}^{N-1} \left(R_{i+1}^\alpha(t) - R_i^\alpha(t) \right) \left(R_{i+1}^\beta(t) - R_i^\beta(t) \right) \quad (1.28a)$$

$$= \frac{24(N+1)k_B T}{V b_{3D}^2} \sum_{p=1}^N X_p^\alpha(t) X_p^\beta(t) \sin^2 \left(\frac{\pi p}{2(N+1)} \right) \quad (1.28b)$$

Upon substituting this stress tensor into Eq.1.27, $G(t)$ is as follows:

$$G(t) = \frac{k_B T N_c}{V} \sum_{p=1}^N \sum_{q=1}^N C_{pq}(t) \quad (1.29)$$

with

$$C_{pq}(t) = \frac{\langle X_p^x(t) X_p^y(t) X_q^x(0) X_q^y(0) \rangle}{\langle X_p^2 \rangle \langle X_q^2 \rangle} \quad (1.30)$$

Here N_c is the number of independent chains in the system. This equation can be simplified as:

$$G(t) = \frac{k_B T c}{N+1} \sum_{p=1}^N \exp \left(-\frac{2t}{\tau_p} \right) \quad (1.31)$$

with c is the number of monomers per unit volume, $c = \frac{NN_c}{V}$. Eq. 1.31 indicate three regimes:

$$\tilde{G}(t) \approx \begin{cases} 1 - \frac{12k_B T}{\zeta_{3D} b_{3D}^2} t, & t \leq \tau_N \\ \sqrt{\frac{\zeta_{3D} b_{3D}^2}{24\pi k_B T}} \frac{1}{t}, & \tau_N \leq t \leq \tau_R \\ \frac{1}{N} \exp \left(-\frac{2t}{\tau_R} \right), & t \geq \tau_R \end{cases} \quad (1.32)$$

where $\tilde{G}(t) = \frac{G(t)}{k_B T c_b}$ and $c_b = NN_c/V$ is the number of density of bonds.

The first and second regimes are independent from the chain length. Fig. 1.3(a) shows the $G(t)$ for the Rouse model with various chain lengths. The second and

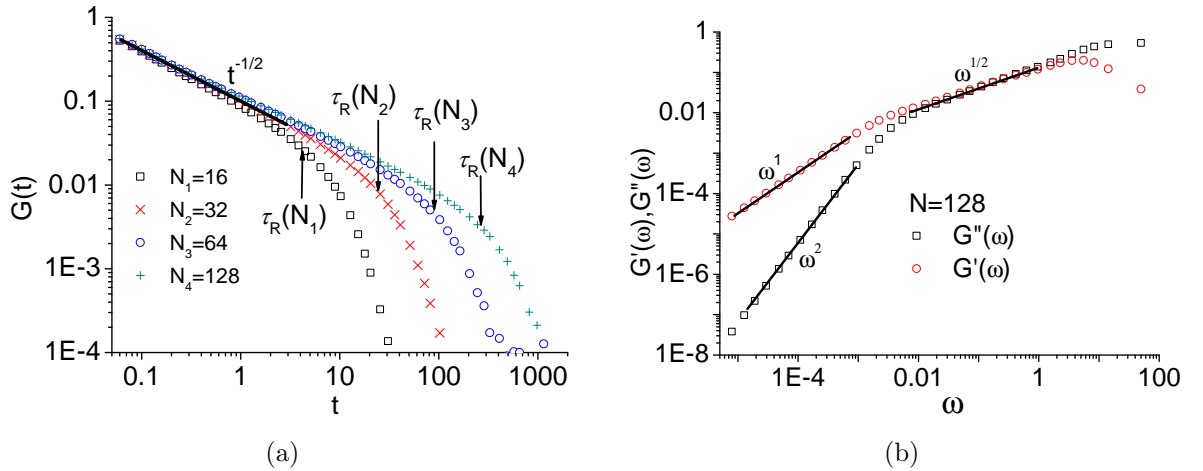


Figure 1.3: The stress relaxation, $G(t)$ for the Rouse model with $N = 16, 32, 64, 128$ are shown in Fig. 1.3(a) and the scaling of $G'(\omega)$ and $G''(\omega)$ are in Fig. 1.3(b).

third regimes, as predicted by Eq. 1.32, are clearly visible. The first regime occurs in a very short time scale thus a smaller time step is required to observe this region. Fig. 1.3(b) shows $G'(\omega)$ and $G''(\omega)$ as predicted by the Rouse model.

1.10 The tube model

The tube model for a single rubber strand with crosslinks located at its ends was introduced by Edwards [40]. In a rubber, the strands cannot cross each other and will form topological constraints. These constraints confine a test strand in a tube-like region if the strands are long enough. The diameter of the tube is independent of the length of the strand and is determined by its local conditions.

De Gennes implemented the tube model for uncross-linked polymer melts by introducing the dynamics of the tube, called ‘reptation’ [11, 12]. At times longer than the equilibration, time of the chain inside the tube τ_e , one does not need to distinguish between the tube and the chain. The stress relaxation of the chain and other quantities are computed from the tube evolution equations.

Doi and Edwards introduced the ‘primitive path’, the shortest path connecting the chain’s ends with the same topology as its tube [9]. The physical meaning of this path is that at an earlier time, the chain’s centre of mass do not move and the chains are wiggling around the primitive path and later, the conformation of the path changes as the chain moves with their ends outside of the original tube and new tube segments are created.

The correct definition of the tube length is still unknown and in this project we will use two definitions which are introduced in section 3.2. First, is the tube axis and second is the primitive path. An alternative definition of the tube length is the ‘time averaged density of a chain’ [41]. However the difficulties with this definition are that the density pattern changes with the chain motion and there are some cases where more than one maximum exists in the cross-sectional density profile of the chain [41].

1.10.1 Definition of the tube model

The tube model assumes that all chains in the melt are frozen except a test chain. The test chain is viewed as being located in a sea of obstacles (referring to the frozen other chains), as shown in Fig. 1.4.

We can map the tube into an equivalent freely jointed chain with N_k bonds of length l_k each. The mapping works by equating the mean square (MS) end-to-end distance, $\langle \mathbf{R}_e^2 \rangle = N_k l_k^2$ and contour length $L = N_k l_k$.

The MS end-to-end distance of the primitive chain is assumed to be equal to the MS end-to-end distance of the chain, $N b_{3D}^2$. If we know the contour length of the

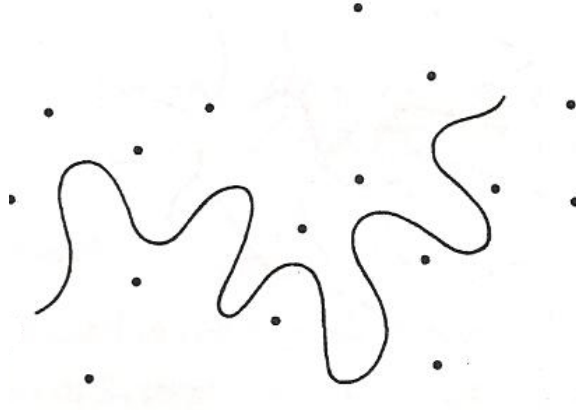


Figure 1.4: The Rouse chain and the obstacles, representing the other chains

primitive chain, L , then

$$La = Nb_{3D}^2 \quad (1.33)$$

$$L = Za \quad (1.34)$$

where Z is the tube Kuhn segments and a is the tube Kuhn length. Thus,

$$a = \frac{Nb_{3D}^2}{L} \quad (1.35)$$

$$Z = \frac{L}{a} = \frac{Nb_{3D}^2}{a^2} \quad (1.36)$$

The primitive path can be viewed as a chain consisting of ‘blobs’ with size a . Each blob contains N_e monomers and behaves as an ideal polymer coil because we assume that the excluded volume interactions are completely screened out in polymer melts. From Eq. 1.36, N_e is defined as:

$$N_e = \frac{N}{Z} = \frac{N^2 b_{3D}^2}{L^2} = \frac{a^2}{b_{3D}^2} \quad (1.37)$$

1.10.2 Pure reptation

The original tube model assumes [20, 31]:

1. The local fluctuations of the primitive path at the chain ends (contour length fluctuations, CLF effects) are neglected [9].
2. The tube is fixed and there is no constraint release, CR. It only moves via reptation, where the tube segments diffuse in curvilinear one dimensional motion along the tube except for the tube ends which randomly move.
3. The friction of the beads of the chain inside the tube, ζ_{1D} is equal with the unentangled Rouse chain, $\zeta_{1D} = \zeta_{3D}$. However, some detailed studies are required to validate this assumption.

Some elements have been added to the original tube model [9] such as CR and CLF. In real polymer melts, the lifetime of an obstacle is finite and leads to some constraint release. The CR is especially effective for binary blends such as when mixing long chains with short chains [42]. In a complete description for the polymer melts, CR should be taken into account. However, this is beyond the scope of the present project as our simulations are based on fixed obstacles for the modeling of polymer melts.

1.10.3 Tube segment occupation function

The tube segment occupation function, $\mu(t)$ is the fraction of the original tube that lives longer than time t and at the disengagement time, τ_d^0 , the original tube is completely forgotten and a new tube for the chain is created. The analytical

expression of $\mu(t)$ for pure reptation is [9, Eq.6.16]

$$\mu(t) = \sum_{p=1,\text{odd}} \frac{8}{p^2\pi^2} \exp\left(-\frac{p^2 t}{\tau_d^0}\right) \quad (1.38)$$

where τ_d^0 is the disengagement time without CLF:

$$\tau_d^0 = \frac{\zeta_{3D} N^3 b_{3D}^4}{\pi^2 k_B T a^2} \quad (1.39)$$

In the case without CR, the tube theory predicts the $\Phi(t) = \mu(t)$ where $\Phi(t)$ is the chains end-to-end relaxation function [43]. The expression for the $\Phi(t)$ is available in [9, Eq.4.35] with $\Phi(t) = \frac{\langle \mathbf{R}_e(t) \mathbf{R}_e(0) \rangle}{\langle \mathbf{R}_e^2 \rangle}$ where $\mathbf{R}_e(t)$ is the end-to-end vector of the chain.

If the tube is deformed, the tube segments are randomly oriented. The orientation contributes to the stress. By means of reptation, when the chain diffuses out of the original tube segment, the segment is deleted. The newly created segments after the deformation has random orientations. The initial deformation is thus forgotten at this stage, where the $G(t)$ is proportional to the $\mu(t)$ [9, 44].

$$G(t) = G_N^0 \mu(t), \quad t \gg \tau_e \quad (1.40)$$

with the entanglement time, τ_e is defined as

$$\tau_e = \frac{a^4 \zeta_{3D}}{3\pi^2 b_{3D}^2 k_B T} \quad (1.41)$$

The stress relaxation $G(t)$ for the entangled melts consists of two regimes:

1. $t < \tau_e$, at this short time scale, $G(t)$ behaves like the free Rouse chain that scales with $t^{-1/2}$ as in Eq. 1.32 and the limit time is τ_e .

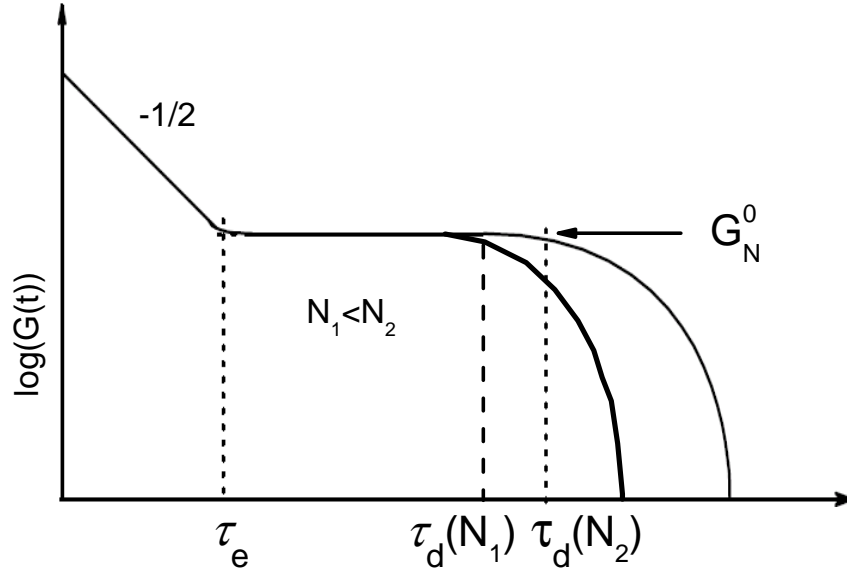


Figure 1.5: A schematic plot of $G(t)$ for different chain lengths as measured in entangled polymer chains.

2. $t > \tau_e$, this regime is based on Eqs. 1.40 and 1.38

The tube theory only predicts the second regime. The schematic plot of the time behaviour of the $G(t)$ as measured for different chain length is shown in Fig. 1.5.

1.10.4 Segmental diffusion

The one dimensional mean square displacement of the bead along the tube contour, $g_s(t)$ is defined as $g_s(t) \equiv \langle \Delta s^2 \rangle$ with $\Delta s = s(t) - s(0)$ where s , ($s = 0, \dots, L$) is the bead coordinate along the tube contour which is measured from a certain fixed point inside the tube (see Fig. 1.6). Assuming s is a continuous function, then in the limit of $N \gg 1$, Δs shows two regimes with the characteristic time of $\tau_{R,1D}$:

$$g_s(t) = \begin{cases} \frac{2k_B T b_{1D}}{\zeta_{1D}} \sqrt{\frac{t \zeta_{1D}}{3\pi k_B T}}, & t \leq \tau_{R,1D} \\ \frac{2k_B T}{N \zeta_{1D}} t, & t \geq \tau_{R,1D} \end{cases} \quad (1.42)$$

where $\tau_{R,1D} = \frac{\zeta_{1D} b_{1D}^2 N^2}{3\pi^2 k_B T}$. The $g_s(t)$ will be further discussed in section 4.4.

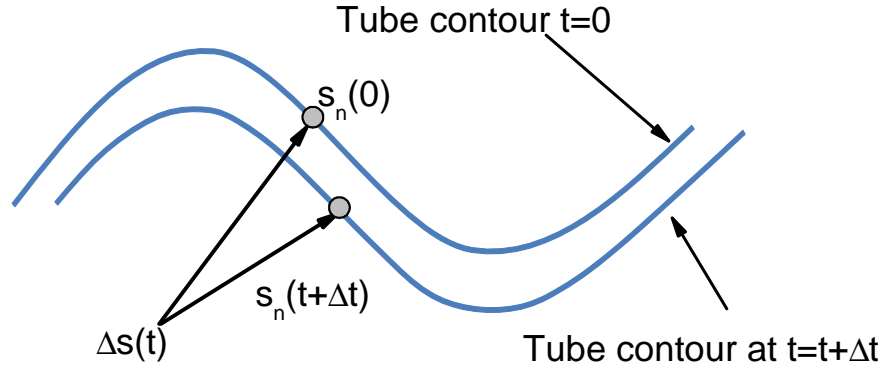


Figure 1.6: Motion of bead n along the primitive path

1.10.5 Bead diffusion in the tube

The MSD of a bead of an entangled chain consists of 4 regimes, (see Fig. 1.7). Each regime is delimited by its characteristic time as follows [9, 11]:

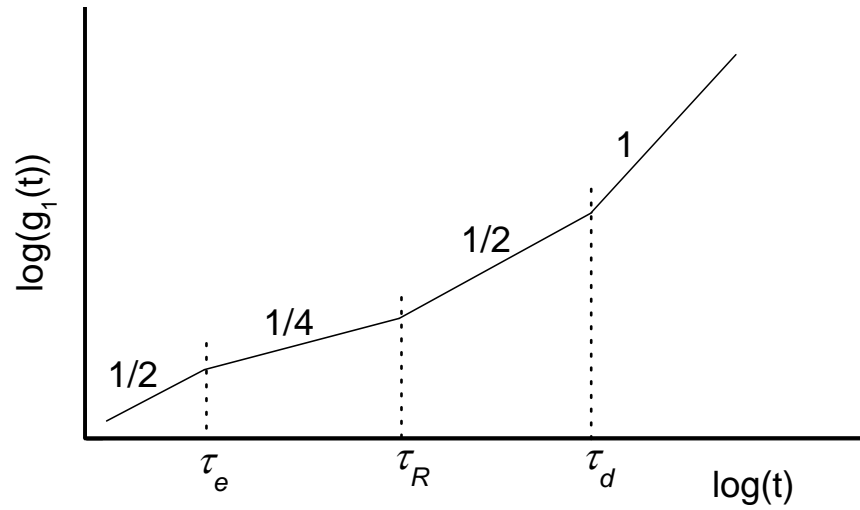


Figure 1.7: The MSD of the tube segments consist of several regimes which is determined by its characteristic time.

1. The first regime, $t \leq \tau_e$

At very short times, the beads move like in a Rouse chain in free space. This

is because the beads do not feel the constraints yet. When a bead moves a distance of the tube diameter ‘ a ’, the dynamics of the bead is restricted by the presence of the constraints. This occurs at time, τ_e which is independent of the chain length N , see Eq. 1.41 [45].

2. Second regime, $\tau_e < t < \tau_R$

The MSD of the beads scales with $t^{1/4}$ with the assumption that the primitive path and the chain as a whole do not move [45]. The MSD of the bead is

$$g_{1,\text{mid}}(t) \sim a\sqrt{g_s(t)} \quad (1.43)$$

where g_s is Eq. 1.42. We will show that the expression 1.43 needs a prefactor, which we calculate in section 4.4.1.

3. Third regime, $\tau_R < t < \tau_d$

The dynamics of the beads can be described as synchronised one dimensional motion of the chain and the tube contour length. The $g_{1,\text{mid}}(t)$ is still described by Eq.1.43 with g_s given in Eq. 1.42 for $t > \tau_R$.

4. Fourth regime, $t > \tau_d$

At this regime, the tube segments are totally renewed. The dynamics of the beads are dominated by the tube reptation, thus it gives [9]:

$$g_{1,\text{mid}}(t) \approx \frac{k_B T a^2}{N^2 \zeta_{3D} b_{3D}^2} t \quad (1.44)$$

From the definition of τ_R and τ_d , we can see that they are separated only by the number of entanglement $3Z$. This indicates that this region is clearly visible only for very long chains.

1.10.6 Contour length fluctuations

Let us denote the average length of the tube by $\widehat{L} = \langle L \rangle$ where L is the instantaneous contour length of the tube. The contour length is assumed to be Gaussian distributed. It can be considered as being under the influence of a quadratic potential [30, 46]:

$$U(\widehat{L}) = \nu \frac{k_B T}{N b_{1D}^2} (L - \widehat{L})^2 \quad (1.45)$$

with $\nu = \frac{3}{2}$. The probability of a chain with length N beads being confined in a tube of length L with its average \widehat{L} and variance $\Delta \widehat{L}^2$ can be approximated by Gaussian function. The approximation at the the region of $L \approx \widehat{L}$ [41, 47–49] is

$$P(L, N) = \left(\frac{1}{2\pi \Delta \widehat{L}^2} \right)^{1/2} \exp \left(\frac{-U(\widehat{L})}{k_B T} \right) \quad (1.46)$$

Thus, the average fluctuations of the tube length is

$$\Delta \widehat{L} \equiv \langle \Delta \widehat{L}^2 \rangle^{1/2} = \left(\frac{N b_{1D}^2}{3} \right)^{1/2} \quad (1.47)$$

Apart from N , the expression for $\Delta \widehat{L}$ also depends on the local parameter b_{1D} , which is the chain statistical segment length inside the tube. Hence, alternatively b_{1D} can be defined as:

$$b_{1D} = \sqrt{\frac{3}{N} \Delta \widehat{L}^2} \quad (1.48)$$

where b_{1D} is related to spring constant for the one-dimensional Rouse chain inside the tube k_{1D} via $k_{1D} = \frac{3k_B T}{b_{1D}^2}$. We mark b_{1D} with the subscript *1D* to stress that b_{1D} might be different from the free Rouse chain parameter in three dimensions, while in [9] there is no distinction between b_{3D} and b_{1D} .

In limit of length scale larger than step size of the tube, the conformations of

the tube are assumed to be Gaussian where for any two tube vertices, \mathbf{V}_i and \mathbf{V}_j with $|i - j| \gg 1$, we expect:

$$P(\mathbf{V}_i - \mathbf{V}_j) = \left(\frac{3}{2\pi|i - j|a^2} \right)^{3/2} \exp \left(-\frac{3(\mathbf{V}_i - \mathbf{V}_j)^2}{2|i - j|a^2} \right) \quad (1.49)$$

thus we obtain

$$\langle (\mathbf{V}(s) - \mathbf{V}(s'))^2 \rangle = a^2 |s - s'| \quad (1.50)$$

where s is the separation between the cells.

In this project, Eq. 1.50 is observed by averaging the internal distance between vertices, i and j as a function of chemical distance $|i - j|$ with the following function:

$$d_i(s) = \frac{1}{Z - s + 1} \sum_{i=0}^{Z-s} \frac{\langle (\mathbf{V}_{i+s} - \mathbf{V}_i)^2 \rangle}{s} \quad (1.51)$$

where the average is calculated over ensemble and time.

Statistics of the tube contour length is assumed to be Gaussian. However, a new tube segment is created when the chain moves out and an old segment is deleted if the chain retracts into the tube. If we assume that the tube is a random walk on a regular d -dimensional lattice, then the chain ends have $(z_d - 1)$ directions to choose from z_d possible path which increases the tube's contour length then there is an imbalance in the change of the contour length. On a larger scale, the conformations of the tube contour segments are represented by a non-folding back random walk statistics in a lattice [41]. The MS end-to-end vector of the non-folding back chain is given by:

$$\langle R_e^2 \rangle = Z^s l^2 \frac{z_d}{z_d - 2} \quad (1.52)$$

where l is the step length of the contour and Z^s is number of tube segments.

The contour length fluctuations, CLF, describe more details of the dynamics

of a single chain inside a tube. The dimension of a real flexible polymer chain can fluctuates and this is not different from the primitive path. These fluctuations contribute significantly to the disengagement time, τ_d (the typical time it takes for the chain to escape from its original tube) and the stress relaxation of the chain. According to Doi and Edwards [9], the CLF makes the tube relax faster, $\tau_d^f < \tau_d^0$, (disengagement time with CLF, τ_d^f) and will enhance the stress relaxation of the chain [9].

The probability of the contour length, $P(L)$ and $\Delta\hat{L}$ was calculated in section 1.10.6, where the relative fluctuation decreases with the number of tube segments:

$$\frac{\Delta\hat{L}}{\hat{L}} \approx \left(\frac{ab_{1D}}{\sqrt{3N}b_{3D}^2} \right) \approx \frac{1}{\sqrt{3Z}} \quad (1.53)$$

The estimation of the τ_d^f is given by [9]:

$$\tau_d^f \approx \tau_d^0 \left(1 - \frac{X}{\sqrt{Z}} \right)^2 \quad (1.54)$$

With X as an unknown parameter which is larger than 1.45 [9,45]. As Z gets larger the effect of CLF become less important. In our model, the CLF is already added thus the τ_d^f in the following analysis will be represented by τ_d . The CLF is more significant in branched polymer, for example the star polymers in melts cannot move by reptation and is relaxed by individual arms retraction.

1.11 Outline of Thesis

This thesis reports the coarse-grained simulations of polymer melts. We studied two well known theories for the dynamics of polymer melts, the Rouse and the tube model. These theories and some analytical results are discussed in this chapter.

In chapter 2, we present the computer simulations for the Rouse chain in an array of obstacles, known as the ‘grid model’. Uncrossability constraints will be implemented to mimic the entanglements. The simulation is developed according to the polymer model discussed in section 1.7. The suitability of the simulation methods (Brownian dynamics and Monte Carlo) and the integration steps (Euler integration steps and predictor-corrector) will be studied. We also studied the effects of allowing the bead to reattempt its movement when it violates the constraint.

The static properties of the entangled polymer chains will be analysed in chapter 3. These include the procedures of the tube construction and the tube length. The definitions of the tube length that we studied are the tube axis and the primitive path. The tube parameters for each definition will be analysed. We also compared the results of the grid model with the lattice models.

Chapter 4 covers the dynamic properties of the polymer chain. First we validated the basic results of the entangled polymer chains as predicted by the tube theory. Then, we analysed the bead diffusion along the tube axis which gave the bead friction inside the tube, ζ_{1D} . By using the ζ_{1D} and the tube static parameters, the properties of the chain dynamics can be predicted.

At the end of this thesis, we will give an overall conclusion and suggestions for improvements of the current computer simulations.

Chapter 2

The Computer Simulation Model

2.1 Introduction

The developments of current technology made computer simulations an essential tool in revealing the microscopic behavior of polymer chains. Nowadays, a number of simulation techniques have been developed such as molecular dynamics (MD), Monte Carlo (MC) and Brownian dynamics (BD) simulations [50,51]. In this project we study BD and MC simulations in order to be able to explore the structures and dynamic properties of polymer melts at time and length scales of microscale. Discussion about MC is available in Appendix A.

The static and dynamic properties of macromolecules can be observed by atomistic MD simulation at molecular level, but it requires a lot of CPU resources. Usually, one is not able to obtain results for long chains where the entanglement effects are evident. One way to solve this problem is to coarse grain (e.g., use groups of atoms as the basic unit in the model), which allows one to use softer potentials and to simulate a large system with a longer time scale. Examples of the coarse-grained models are dynamic Monte Carlo [52, 53], coarse-grained molecular dynamics and

BD simulations [50, 51, 54]. However softer potentials do not prevent the chains from crossing each other, thus the effects of entanglements can be lost with coarse graining. In this chapter, we discuss our computer simulations for polymer melts, the grid model. This includes the simulation methods (BD and MC), integration algorithms and uncrossability constraints.

2.2 Brownian dynamics model

Brownian dynamics is used to simulate the dynamics of molecules that undergo Brownian motion. The motion arise from random collisions of the particles with other particles in the solvent/melts. In Brownian dynamics model, the SDE of the Rouse chain (Eqs. 1.9a, 1.9b and 1.9c) can be solved by integrating them with respect to time. In the grid model, there is an additional potential caused by the constraints. The potential between the bonds with the line obstacle which is represented by the ‘step’ potential as follows [55]:

$$U(d) = \begin{cases} 0, & d > 0 \\ \infty, & d = \delta_i \end{cases} \quad (2.1)$$

where $\delta_i \rightarrow 0$ is the closest distance between the bond and the obstacles.

A suitable numerical integration method is required as it will determine the efficiency of the simulation and accuracy of the data. In determining the procedure for our simulation, we have studied two numerical schemes. They are the Euler integration algorithm and the predictor-corrector integration algorithm.

2.2.1 Euler integration algorithm

The Euler integration step, EIS also known as conventional Brownian dynamics is a first-order algorithm to solve the Rouse equation [56–59]. The algorithm is based on the following particle update scheme:

$$\mathbf{R}_i(t + \Delta t) = \mathbf{R}_i(t) + \frac{\mathbf{F}_i(\{\mathbf{R}_j(t)\})\Delta t}{\zeta_{3D}} + \Gamma_i(t) \quad (2.2)$$

where Δt is the time step and $\Gamma_i(t)$ is a random displacement of particle i . The $\Gamma_i(t)$ is sampled from a Gaussian distribution with zero mean and variance $\langle \Gamma_{i,k}^\alpha(t)\Gamma_{j,m}^\beta(t') \rangle = (2\Delta tk_B T \delta_{ij} \delta_{km} \delta_{\alpha\beta}) / \zeta_{3D}$ where k and m are the current and previous time steps, respectively. Their Cartesian components are denoted by α and β . The bonded forces, $\mathbf{F}_i(\{\mathbf{R}_j(t)\})$ are

$$\mathbf{F}_i(\{\mathbf{R}_j\}) = -\frac{dU_{\text{Rouse}}}{d\mathbf{R}_i} \quad \text{with} \quad (2.3)$$

$$U_{\text{Rouse}} = \frac{3k_B T}{2b_{3D}^2} \sum_{i=0}^{N-1} (\mathbf{R}_{i+1} - \mathbf{R}_i)^2 \quad (2.4)$$

where k_B is Boltzmann's constant and T is the absolute temperature.

2.2.2 Predictor-corrector integration algorithm

The predictor-corrector (PC) is a second-order algorithm. It is based on an extended deterministic Runge-Kutta algorithm in which the stochastic term is added. The algorithm involves the prediction and the correction steps:

First, the predicted position of bead \mathbf{R}_i is calculated by using the EIS:

$$\mathbf{R}_i^p(t + \Delta t) = \mathbf{R}_i(t) + \frac{\mathbf{F}_i(\{\mathbf{R}_j(t)\})\Delta t}{\zeta_{3D}} + \Gamma_i(t) \quad (2.5)$$

Second, the positions of beads are corrected by using the second order stochastic Runge-Kutta algorithm [57]:

$$\mathbf{R}_i(t + \Delta t) = \mathbf{R}_i(t) + \frac{1}{\zeta_{3D}} [\mathbf{F}_i^a(t) + \mathbf{F}_i^b(t + \Delta t)] \Delta t + \Gamma_i(t) \quad (2.6)$$

where $\mathbf{F}_i^a = \mathbf{F}_i(\{\mathbf{R}_j(t)\})$ and $\mathbf{F}_i^b = \mathbf{F}_i(\{\mathbf{R}_j^p(t + \Delta t)\})$. The $\Gamma(t)$ in Eq. 2.6 is the same as in Eq. 2.5. In contrast to the EIS, two force evaluations per bead per time step are required for this algorithm.

2.3 Uncrossability constraints

Uncrossability constraints are required to prevent the chains from crossing other chains. The uncrossability constraints can also be used for multi-chain model or single chain model where other chains are presented by obstacles. The algorithm for uncrossability constraints involves a simple geometrical operation. The operations are simple but must be optimized because they are repeated billions of times during a long simulation and thus take a lot of computational time. For instance, the implementation of one of the existing entanglement algorithms in a stochastic dynamic program is roughly 10 times slower than the same algorithm without uncrossability constraints [23]. In order to check whether the bond crosses the obstacles, we implement 3 steps of checking.

1. For bond $\mathbf{r}_i(t)$ and line obstacle \mathbf{L}_i as shown in Fig. 2.1. The scalar triple product is calculated [25] at each instant of time:

$$v_i(t) = (\mathbf{R}_i(t) - \mathbf{l}_i) \cdot (\mathbf{r}_i(t) \times \mathbf{L}_i) \quad (2.7)$$

The absolute value of v_i , is the volume of the parallelepiped defined by $\mathbf{R}_i(t)$, \mathbf{l}_i , \mathbf{r}_i

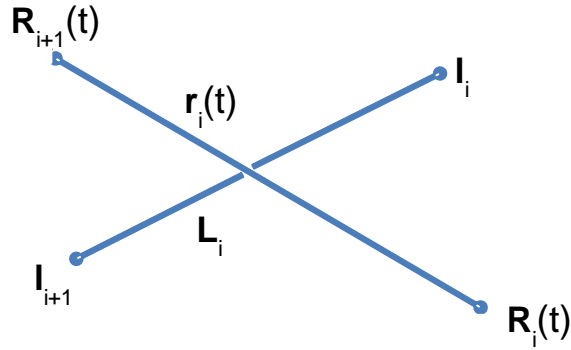


Figure 2.1: Bond r_i connects beads R_i and R_{i+1} , and line obstacle L_i connects point l_i and l_{i+1} .

and L_i . There are three possibilities for the volume to become zero. First, if the distance between the bond and the line obstacle is zero. Second, if the bond and obstacle are parallel to each other. Third, if the bond length $r(t)$ is zero. Those three situations are very rare to occur in a standard linear chains simulation [24] ('standard' refer to the grid model). However, they occur in the primitive path construction which uses the geometrical moves (see section 3.2.3). If one of these conditions occur the trial move is rejected then the bead is kept at its original position. This is to avoid the $|v_i|$ become zero, which makes us unable to detect whether the bond has crossed the line. If v_i changes its sign upon displacing the bond:

$$v_i(t)v_i(t + \Delta t) < 0 \quad (2.8)$$

there is a possibility that the bond has crossed the constraint. However, Eq. 2.8 is only true if the bond and the line obstacle are infinite. If it is not, the following check is required.

2. This analysis is for a plane and line intersection. There are two planes formed

when bead $\mathbf{R}_i(t)$ moves into a new position $\mathbf{R}'_i(t + \Delta t)$ (see Fig. 2.2). Each plane contains one triangle. The first plane is formed by the triangle 1 and the triangle 2 is located on the second plane. In the following discussion, we only focus on the first plane and its corresponding triangle. For the second plane, we use the same steps as in the first plane. The beads and obstacles in this plane are illustrated in Fig. 2.3.

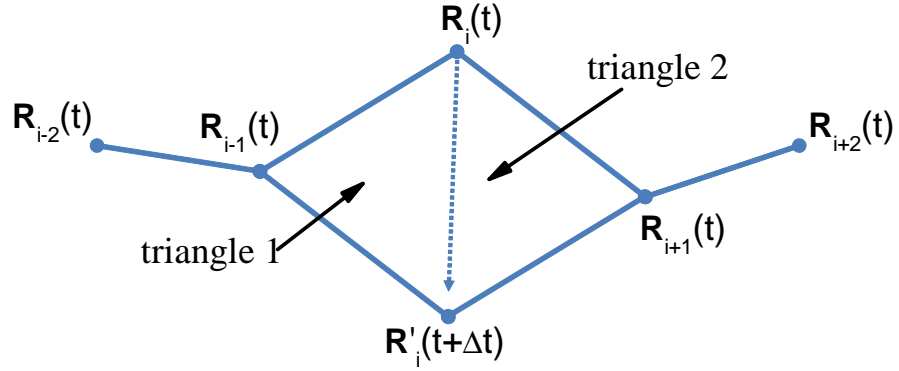


Figure 2.2: Bead $\mathbf{R}_i(t)$ moves into a new position $\mathbf{R}'_i(t + \Delta t)$, it forms two triangles. The first triangle is constructed by $\mathbf{R}_i(t)$, $\mathbf{R}_{i-1}(t)$, $\mathbf{R}'_i(t + \Delta t)$ and the second triangle is by $\mathbf{R}_i(t)$, $\mathbf{R}_{i+1}(t)$, $\mathbf{R}'_i(t + \Delta t)$.

Point \mathbf{p} of the line \mathbf{L}_i that passes through the plane is given by:

$$\mathbf{n} \cdot (\mathbf{l}_i + \mu (\mathbf{l}_{i+1} - \mathbf{l}_i)) = \mathbf{n} \cdot \mathbf{p} \quad (2.9)$$

with \mathbf{n} is normal vector of the plane. The parameter μ is obtained by:

$$\mu = \frac{\mathbf{n} \cdot (\mathbf{p} - \mathbf{l}_i)}{\mathbf{n} \cdot \mathbf{L}_i} \quad (2.10)$$

If $\mathbf{n} \cdot \mathbf{L}_i = 0$, this means that the line and plane are parallel thus bead $\mathbf{R}'_i(t + \Delta t)$ does not violate the constraint.

The point \mathbf{p} will intersect with the plane if:

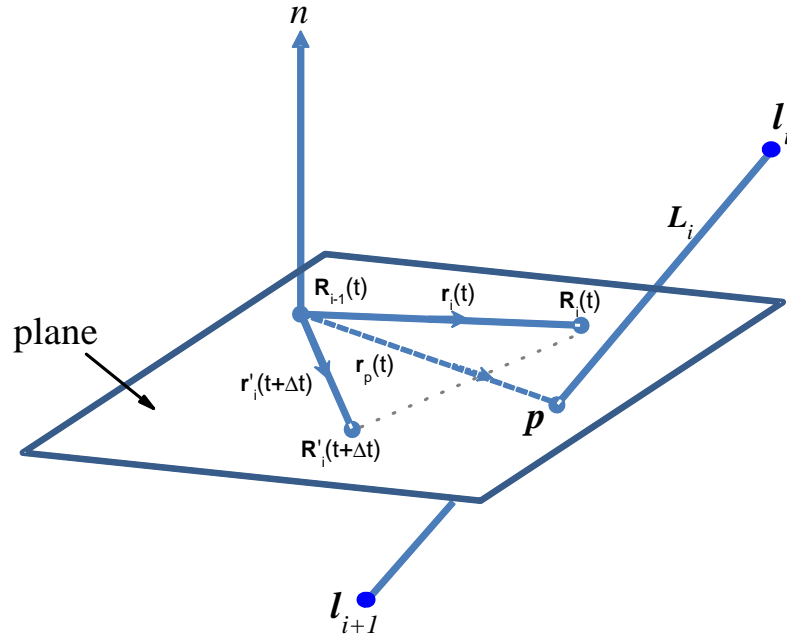


Figure 2.3: The plane is constructed by the three position vectors $\mathbf{R}_i(t)$, $\mathbf{R}_{i-1}(t)$ and $\mathbf{R}'_i(t + \Delta t)$, with \mathbf{n} a normal vector of the plane. The line \mathbf{L}_i intersects with the plane at position \mathbf{p} . $\mathbf{r}_p(t)$ is a vector connecting $\mathbf{R}_{i-1}(t)$ and \mathbf{p} .

- $0 < \mu < 1$: the intersection is between point \mathbf{l}_i and \mathbf{l}_{i+1} thus go to step 3.
- $\mu = 0$ or $\mu = 1$: the intersection either occurs at the end point of \mathbf{l}_i or \mathbf{l}_{i+1} .
- $\mu > 1$ or $\mu < 0$: there is no intersection along the point \mathbf{l}_{i+1} and \mathbf{l}_i .

An intersection can occur at any point of the surface. The following check is required to know if the intersection is located within the triangle. If it does, then this implies that the bead's movement has violated the constraint. The next step will test this.

3. Finally, we use the Barycentric method to determine the location of point \mathbf{p} . According to this method, assume a triangle made by beads \mathbf{A} , \mathbf{B} and \mathbf{C} . Any point \mathbf{p} is inside the triangle can be described by a linear combination of

the beads:

$$\mathbf{p} = \lambda_1 \mathbf{A} + \lambda_2 \mathbf{B} + \lambda_3 \mathbf{C} \quad (2.11)$$

where λ_1 , λ_2 and λ_3 are the coefficient in the Barycentric coordinates. Taking coefficient in Eq. 2.11 gives:

$$1 = \lambda_1 + \lambda_2 + \lambda_3 \quad (2.12)$$

Rearrange the coefficients and substitute back it into Eq. 2.11:

$$\mathbf{P} - \mathbf{C} = \lambda_1(\mathbf{A} - \mathbf{C}) + \lambda_2(\mathbf{B} - \mathbf{C}) \quad (2.13)$$

In our case, $\mathbf{A} = \mathbf{R}_i(t)$, $\mathbf{B} = \mathbf{R}'_i(t + \Delta t)$ and $\mathbf{C} = \mathbf{R}_{i-1}(t)$. Convert the parameters in Eq. 2.13 into their connectiong vectors (see Fig. 2.3) gives:

$$\mathbf{r}_p = \lambda_1 \mathbf{r}_i(t) + \lambda_2 \mathbf{r}'_i(t + \Delta t) \quad (2.14)$$

In 3D case, there are three equations with two unknown parameters λ_1 and λ_2 , so any one equation can be dropped and the remaining two will be solved. The equation is solved by using Cramer's rule [60]. The point \mathbf{p} is located in the triangle, if and only if:

$$\lambda_1 + \lambda_2 < 1 \quad \text{with} \quad \lambda_1 \in (0, 1) \quad \text{and} \quad \lambda_2 \in (0, 1) \quad (2.15)$$

and hence the constraint is violated.

2.4 The grid model

The grid model is a single chain model. The chain is modelled by a Rouse chain which is located in a regular grid of fixed point obstacles (for 2D simulation) or line obstacles (for 3D simulation). The function of the obstacles is to mimic the entanglements with other chains. The thickness of the lines and the diameter of the ‘points’ are only constrained by the floating-point precision. This is small enough in order to have a negligible effect on the static properties and therefore it only affects the dynamic properties of the chain [61, 62].

The only parameter that determine the size of the square lattice (in 2D) and the cubic lattice (in 3D) of the obstacles is the length of the grid spacing g , ($g = 1, 2, \dots$). The dimensionless unit of g is defined as $g' = \frac{g}{b_{3D}}$, which shown in Fig. 2.4.

The mobility of the chains is restricted by prohibiting bonds to cross the obstacles. The model is supposed to mimic real polymer melts where long range hydrodynamic and excluded volume interactions are screened by other chains [9, 63]. In this study, we use the 3D case. An example of a snapshot of our simulation with $N = 13$ and $g' = 1$ is shown in Fig. 2.5.

2.4.1 Implementation of the Brownian dynamics integration scheme

To incorporate the effect of the uncrossable constraints we modify the integration algorithm as follows:

1. All beads must be selected to move at each time step. The order in which beads in the system are moved is taken at random (by generating a permutation of bead indices). This is to make sure our algorithm is time reversible, head-tail

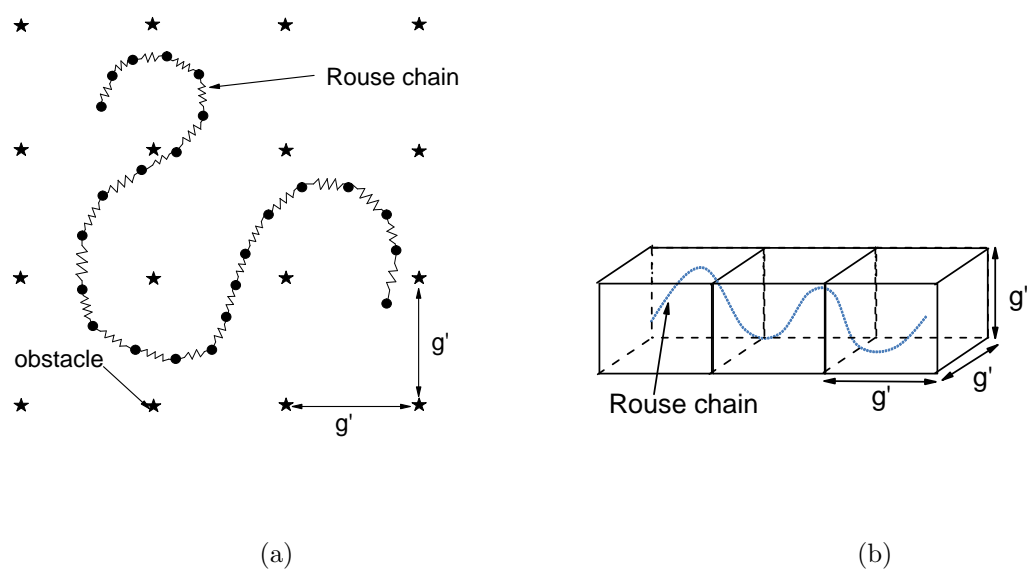


Figure 2.4: The Rouse chain in an array of point obstacles for 2D model (2.4(a)) and the chain in 3D cubic lattice (2.4(b)).

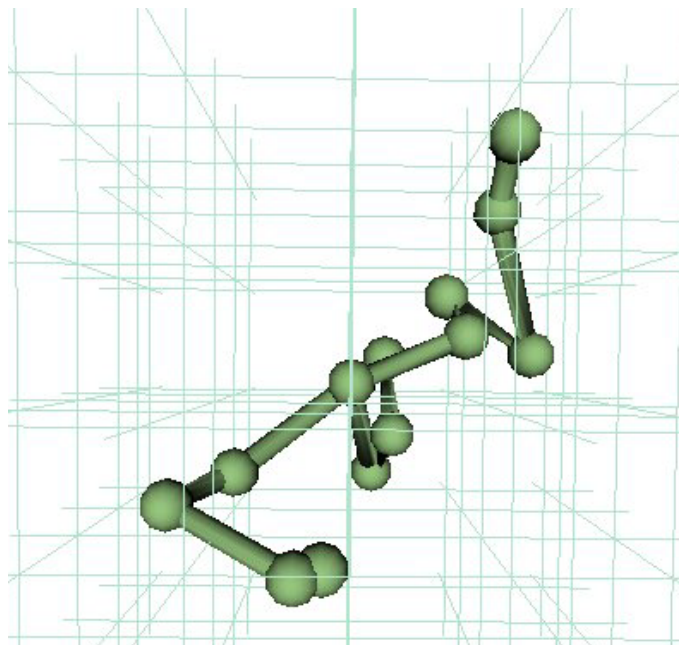


Figure 2.5: A snapshot of the 3D model of the computer simulation, consisting of chain with 13 beads located in a grid, $g' = 1$.

symmetric with respect to the chain ends and as efficient as possible.

2. The selected bead is moved by using the selected numerical integration schemes either the EIS or the PC.
3. A possible violation of constraints is checked for the current bead by looking at the bonds with which the bead is connected (the constraints are point-like in 2D and lines in 3D). The detail about the violation of constraints was discussed in section 2.3.
4. If any of the two bonds crossed the constraint then the motion is rejected and keep the bead at its original location. Otherwise the movement is accepted.
5. Step 1 is repeated for other selected beads.

2.5 The computer program: Generic Polymer Simulation

Our Simulations are run by using Generic Polymer Simulation (GPS). GPS is a simulation package which is developed by the Theoretical Polymer Physics group, at the University of Reading. This package works as a platform for researchers to build their polymer models and uses object oriented programming concepts. The advantage of this package is that researchers are able to share or use some common functions such as observables and analyses. Some parts of the code describing the specific model make use of classes and inheritance. Therefore the validation of the model is easier as some functions are already validated by others.

2.6 Discussion

2.6.1 Brownian dynamics step

In the Brownian dynamics simulations, the size of time step contributes to accuracy of the results and simulation's efficiency. An optimal time step is required to preserve the Gaussian statistics of the chains and minimize the computational time. Thus we did analysis of rejection rate for various sizes of time step, Δt . Average rejection rate (γ_{rej}) is the average number of rejection movement due to obstacles violation for each particle per integration step. The γ_{rej} as a function of Δt for different chain lengths with $g' = 1$ and $g' = 2$ is shown in Fig. 2.6.

The γ_{rej} for all N and g' shows a slow increase until $\Delta t = 0.01$ and then dramatic increase with Δt . The fitting of the data indicate that the γ_{rej} for both g' approximately scale with $\sqrt{\Delta t}$. As a result, the time step that will be used in our simulation is $\Delta t = 0.01$, just before fast increase of γ_{rej} .

2.6.2 Integration step

The EIS is easy to implement in computer programming, however it has strong time step dependence. The smaller time step is required to provide accurate results. However, a larger time step allows one to simulate longer chain length or time scales.

The PC method can give more accurate results for larger time steps. This method was first developed for computer simulations of colloid particles [56], Brownian motion of particles in one [57] and two dimensions [58]. Although there is extra works required (calculate the predicted positions and then correct them) but there is still significant gain in efficiency because time step can be much larger. The objective of this analysis is to study the suitability of PC for our simulations.

The analysis is carried out by comparing the results between these methods for

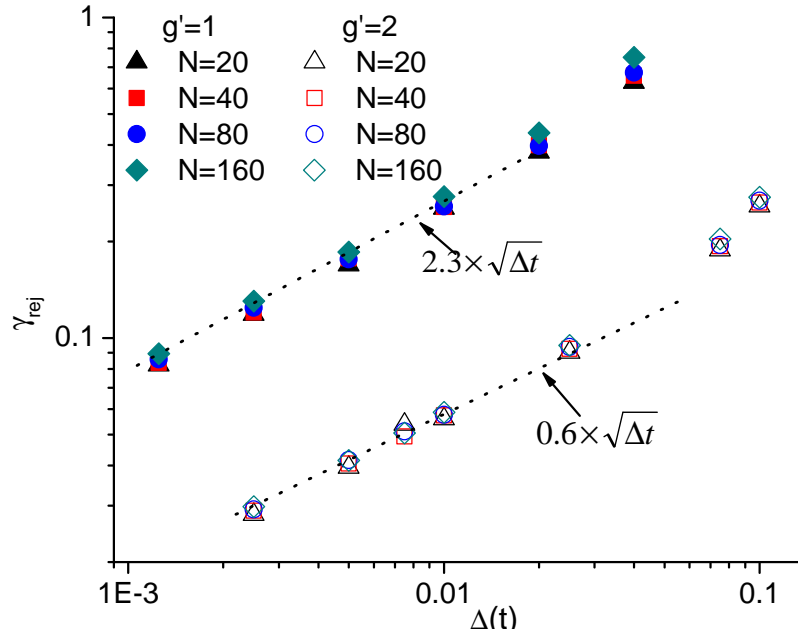


Figure 2.6: Average rejection rate γ_{rej} versus different sizes of time steps, Δt for $N = 20, 40, 60$ and 160 . The open symbols are for $g' = 1$ and filled for $g' = 2$. The dotted lines are the linear fitting of the data, which scale approximately with $\sqrt{\Delta t}$.

the Rouse chain without and with grid. We are interested in the influence of the algorithms on some physical quantities characterising statics and dynamics of the chain. They are the $d(s)$, $g_{1,\text{mid}}(t)$ and $G(t)$.

In the static property, we studied the Gaussian properties of the chain by analysing the $d(s)$ as a function of Δt . We obtained the $d(s)$ by taking average values of the vector connecting beads with chemical distance 4, $d(4)$. The $d(4)$ as a function of Δt and Δt^2 are shown in Fig. 2.7. In this figure, the $d(s)$ from the PC for all Δt are much closer to the expected $d(s) = 1$ while from the EIS, it increases linearly with Δt . The $d(4)$ from the PC is proportional to Δt^2 . Thus, it can be concluded that the PC is able to preserve the Gaussian statistics of the chains better than EIS even for the larger Δt .

In the case of dynamic properties of the chain, we investigate the functions of $G(t)$ and $g_{1,\text{mid}}(t)$ with $N = 16$ at $t = 9.6$ and 8.0 , respectively. These are shown in

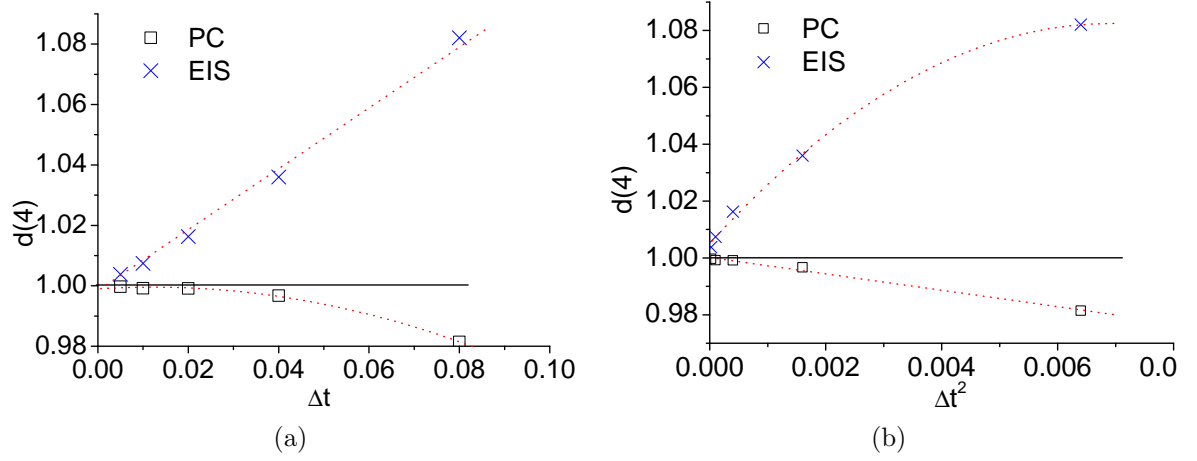


Figure 2.7: The $d(s)$ for 4 beads distance of the free Rouse chain from the EIS and PC algorithms with $N = 16$ as a function of time steps Δt (in Fig. (a)) and Δt^2 (in Fig. (b)). The solid lines are the $d(s)$ for the Gaussian chain statistics.

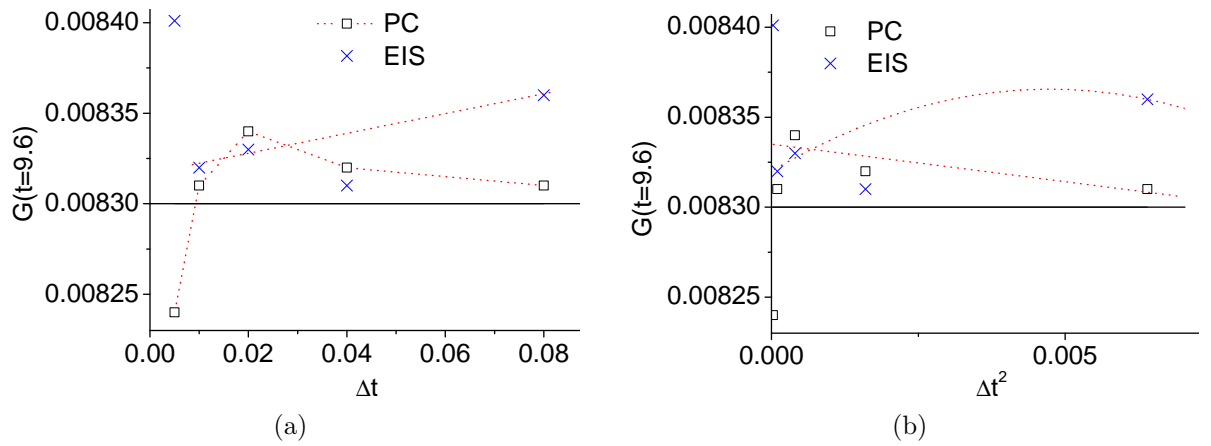


Figure 2.8: The $G(t)$ at $t = 9.6$ of the free Rouse chain with $N = 16$ from the EIS and PC algorithms as a function of Δt (in Fig. (a)) and Δt^2 (in Fig. (b)). The solid lines are the exact values for $G(t = 9.6)$ obtained from expression 1.31.

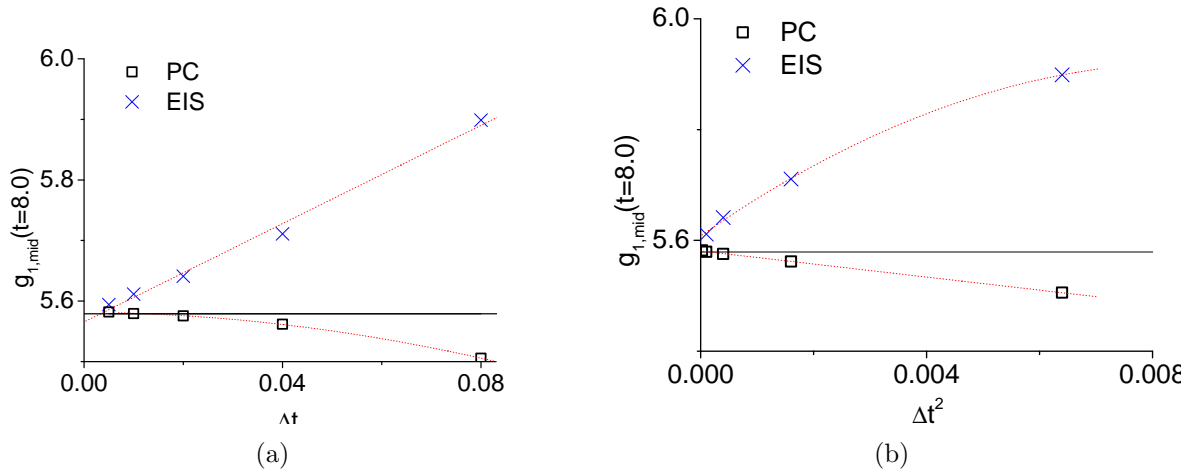


Figure 2.9: The $g_{1,\text{mid}}(t)$ at $t = 8.0$ from the PC and EIS algorithms with $N = 16$ as a function of Δt (in Fig. (a)) and Δt^2 (in Fig. (b)). The solid lines are the exact values for $g_{1,\text{mid}}(t = 8.0)$ obtained from expression 1.18.

Figs. 2.8 and 2.9, respectively. The results obtained from $G(t = 9.6)$ at small sizes of Δt are quite noisy but their fluctuations are still close to the exact values. There are no significant differences between the $G(t)$ obtained from the PC and the EIS (see Fig. 2.8). This is also shown in the $G(t)$ as a function of t with $N = 16$ and $\Delta t = 0.08$ (see Fig. 2.10).

The $g_{1,\text{mid}}(t = 8.0)$ from the EIS deviates significantly from the exact value while the value obtained from the PC only shows a slight deviation. The $g_{1,\text{mid}}(t = 8.0)$ from the EIS and PC changed linearly with Δt and Δt^2 , respectively. The results from the PC algorithm have demonstrated that it weakly changes with Δt .

From this analysis, we found that the PC provides good estimation for static and dynamics of the Rouse chains without grid. This is expected because the simulation is more or less the same as being reported in the literature, i.e., the motion of Brownian particles [56, 57] and dynamics of colloid particles [56]. The question is, whether the PC is able to give the same precision when we implement uncrossability constraints?

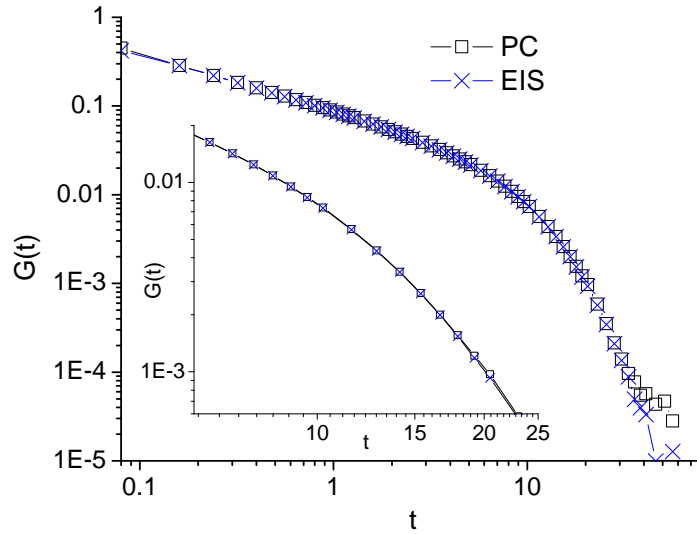


Figure 2.10: The $G(t)$ as a function of t with $N = 16$, $\Delta t = 0.08$ for EIS and PC.

For this purpose, we performed the similar analysis with $g' = 1$. The limitation of such analysis was the unavailability of the analytical value of each observable to compare with. However, we can still investigate the convergence of the observables as $\Delta t \rightarrow 0$.

The function of $d(s)$ from simulations of $N = 32$ and $g' = 1$ for various Δt are obtained from the EIS and the PC are shown in Fig. 2.11. For small Δt , the $d(s)$ from PC are approximately close to the Gaussian chain statistics $d(s) = 1$ (see Fig. 2.11(b)) compared to EIS (see Fig. 2.11(a)). The $d(s)$ obtained from the end-to-end distance of 8 beads, $d(8)$ as function of Δt and Δt^2 are shown in Fig. 2.12, while $d(3)$ for $g' = 2$ with $N = 64$ are shown in Fig. 2.13. These plots demonstrated similar trends as the Rouse chain without grid. It can be concluded that the PC also produce better result for static properties of the entangled chains.

For dynamics observations, the $G(t)$ from the EIS and the PC algorithms with different sizes of Δt are shown in Fig. 2.14 and the intermediate-time regions is shown in the inset. It was observed that the $G(t)$ from the PC change slower

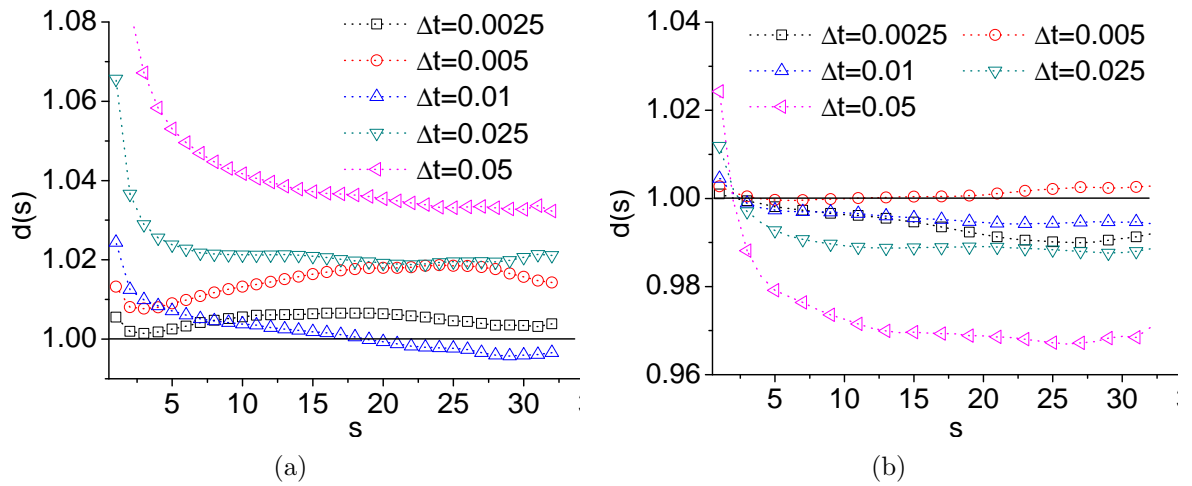


Figure 2.11: The $d(s)$ for $N = 32$ and $g' = 1$ from the EIS (a) and PC (b) algorithms with different sizes of the time steps. The solid lines are the $d(s)$ for ideal random walk statistics of the chain.

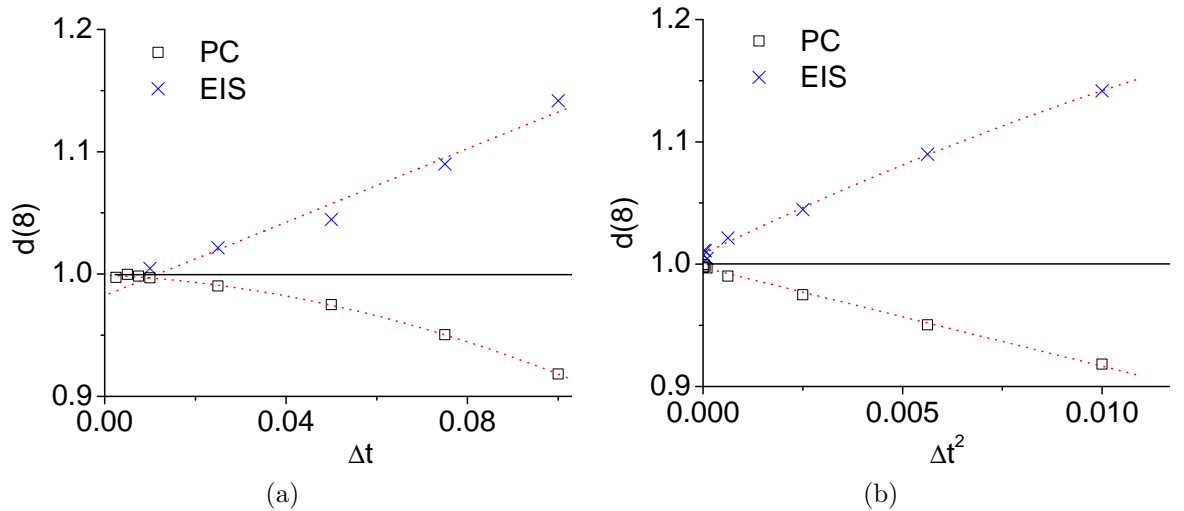


Figure 2.12: The $d(8)$ from the EIS and PC algorithms for $N = 32$, $g' = 1$ with Δt (in Fig. (a)) and Δt^2 (in Fig. (b)).

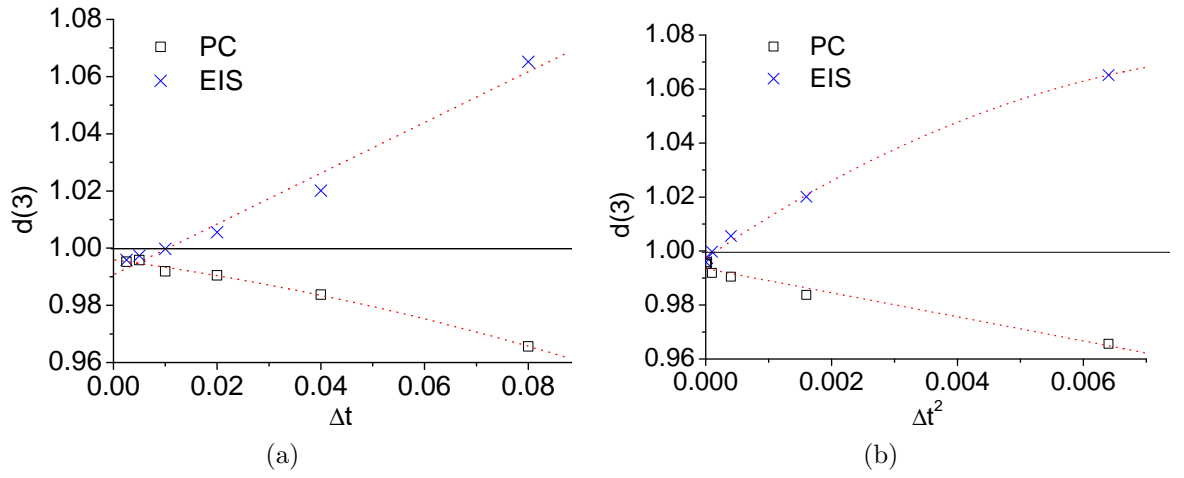


Figure 2.13: The $d(3)$ from the EIS and PC algorithms with $N = 64$, $g' = 2$ as a function of Δt (in Fig. (a)) and Δt^2 (in Fig. (b)).

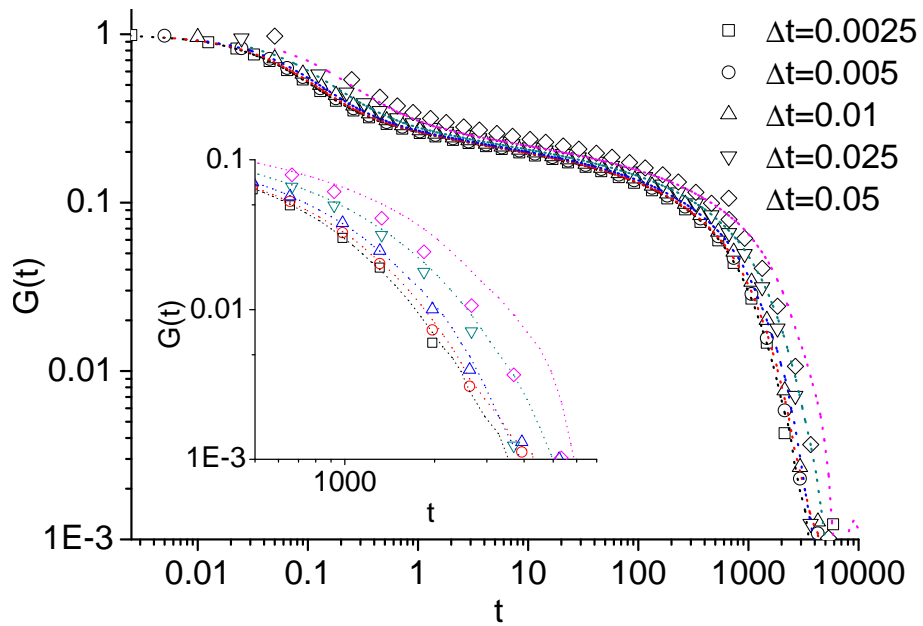


Figure 2.14: The $G(t)$ from the EIS and PC algorithms are in dotted lines and symbols, respectively. The data from $N = 32$, $g' = 1$ and different sizes of the time step, Δt . The inset shows an enlargement of the intermediate-time regions.

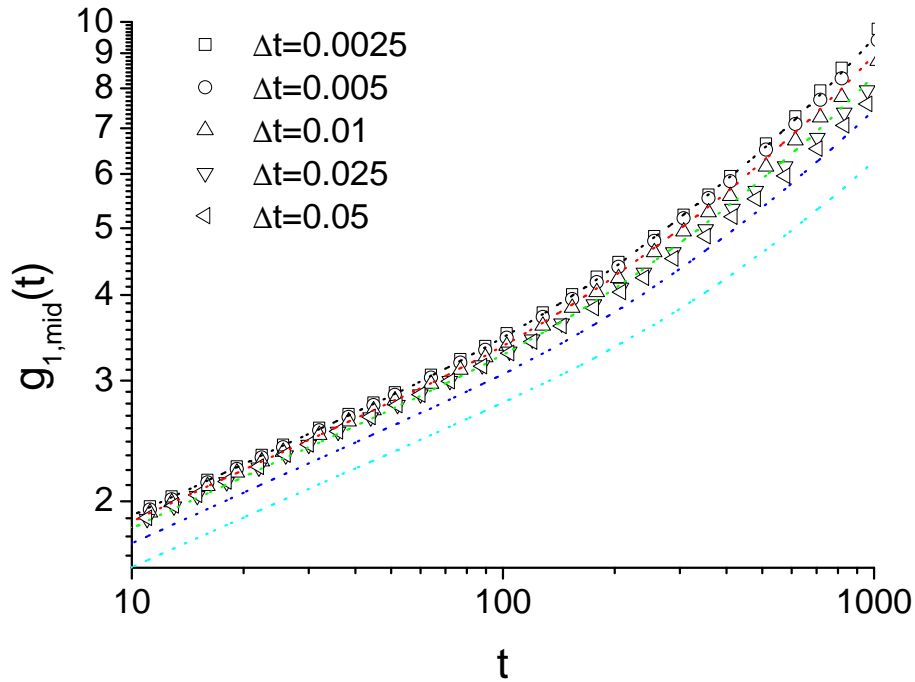


Figure 2.15: The intermediate-time regions of the $g_{1,\text{mid}}(t)$ from the EIS (in lines) and PC (in symbols) algorithms with $N = 32$, $g' = 1$ and different sizes of the time step.

with Δt than EIS. At $\Delta t \leq 0.01$, both algorithms produce very similar $G(t)$. The contribution of PC towards the $g_{1,\text{mid}}(t)$ can be seen in its intermediate-time regions (see Fig. 2.15). The $g_{1,\text{mid}}(t)$ from the PC is less affected by the Δt compared to the EIS.

In the entangled Rouse chain, we found that the PC has better convergence of both static and dynamic properties as compared to EIS. Thus, we will use the PC algorithm with $\Delta t = 0.01$ in our simulations.

2.6.3 Number of attempts

In this section, we vary number of attempts that are allowed if the bead's motion violated a constraint. There are other algorithms available such as the Monte Carlo simulations, where the movement is rejected if it violates the constraints (see section

A.1.1).

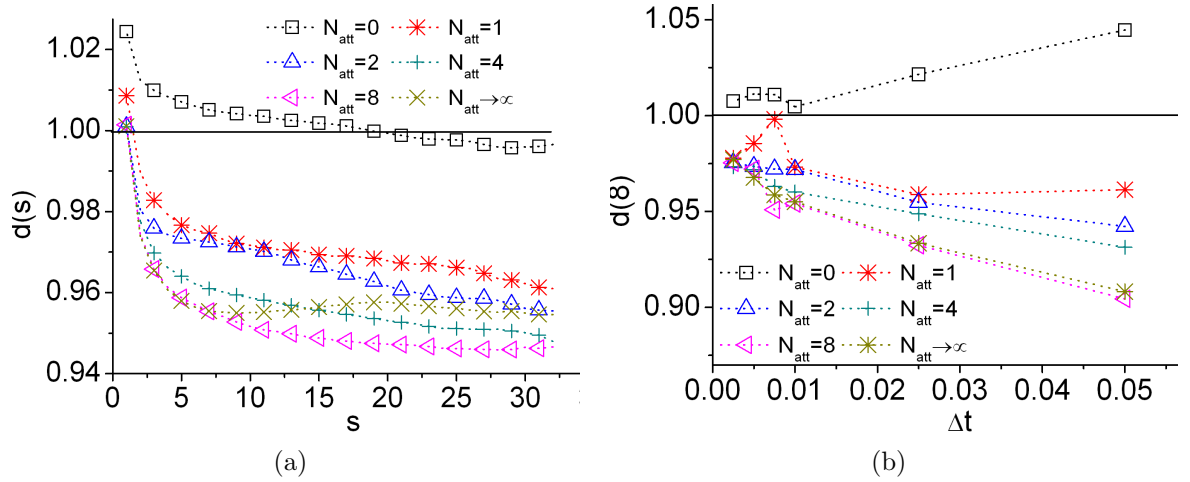


Figure 2.16: The $d(s)$ over the s beads distance with $N = 32$, $g = 1$, $\Delta t = 0.01$ and different number of attempts N_{att} in Fig. (a). The $d(8)$ for each N_{att} as a function of time steps which obtained from Fig. (a) are in Fig. (b). The solid lines in both graphs are the $d(s)$ for Gaussian chain statistics.

We are interested in the influence of maximum number of attempts N_{att} on various static and dynamics properties. They are $d(s)$, MS displacement of the middle bead, $g_{1,\text{mid}}(t)$, stress relaxation, $G(t)$ and end-to-end vector relaxation function, $\Phi(t)$. The procedure of this analysis is that, we run several simulations with the same input parameters N , g and Δt but we vary the maximum number of attempts that is allowed. For example, if $N_{\text{att}} = 3$, the bead will attempt to move 3 times and if it still violates the constraint, then the bead is not moved during that time step.

The contribution of N_{att} to the static properties of the chain are determined from the $d(s)$ which is shown in Fig. 2.16. The function of $d(s)$ without attempt procedure, $N_{\text{att}} = 0$ shows a moderate decrease and the values are relatively close to the expected Gaussian chain statistics, $d(s) = 1$. Increase in the N_{att} values, however, the $d(s)$ deviate more than 2% from the expected values. The $\langle b_{3D}^2 \rangle$ of each N_{att} is obtained from the vector connecting beads with chemical distance 8,

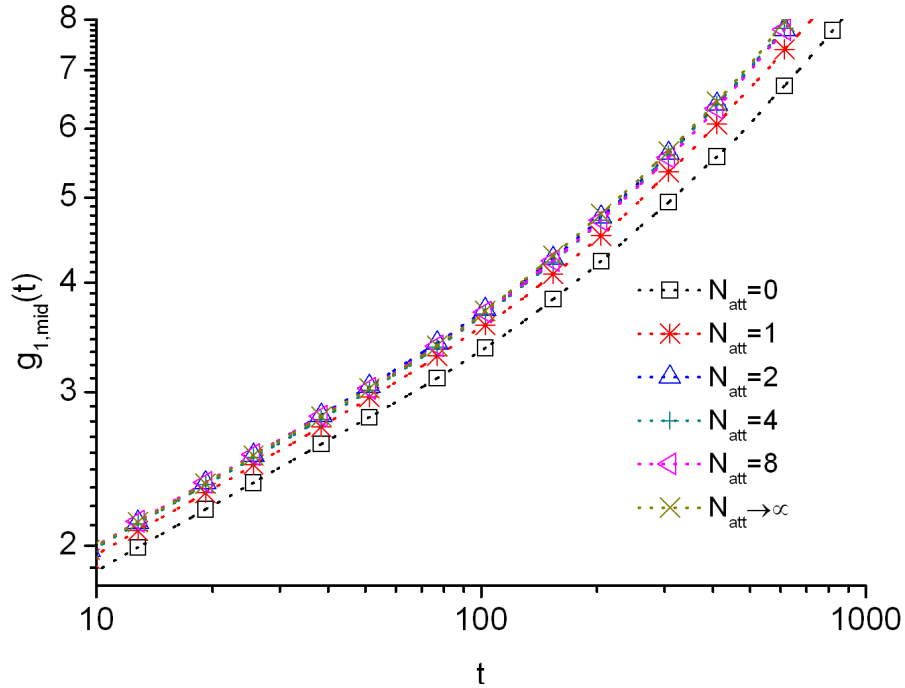


Figure 2.17: The intermediate-time regions for the $g_{1,\text{mid}}(t)$ with $N = 32$, $g = 1$, $\Delta t = 0.01$ and different number of attempts, N_{att} .

$d(8)$ is plotted as a function of Δt in Fig. 2.16(b). The figure shows for $\Delta t \leq 0.01$, the $\langle b_{3\text{D}}^2 \rangle$ from $N_{\text{att}} = 0$ is almost equivalent to the exact values, $\langle b_{3\text{D}}^2 \rangle = 1$, whereas for the $N_{\text{att}} > 0$, about 2% deviation was obtained. In this project, we will use $\Delta t = 0.01$ for our Brownian dynamics simulations, thus by using $N_{\text{att}} = 0$, the simulation will be able to preserve the Gaussian statistics of the chains.

For the dynamics analysis, we use the simulation of $N = 32$ with $g' = 1$, $\Delta t = 0.01$ and different number of attempts, N_{att} . The intermediate regimes of the $g_{1,\text{mid}}(t)$, is shown in Fig. 2.17. The middle bead moves slower for $N_{\text{att}} = 0$ as compared to the higher N_{att} . This is because the beads do not move when they were rejected due to the constrain violations.

The $G(t)$ for various maximum number of attempts is shown in Fig. 2.18. The results for $G(t)$ are not very sensitive on N_{att} . The clear difference is shown in the inset. The $N_{\text{att}} = 0$ shows the chains relaxed slower compared to the others. This

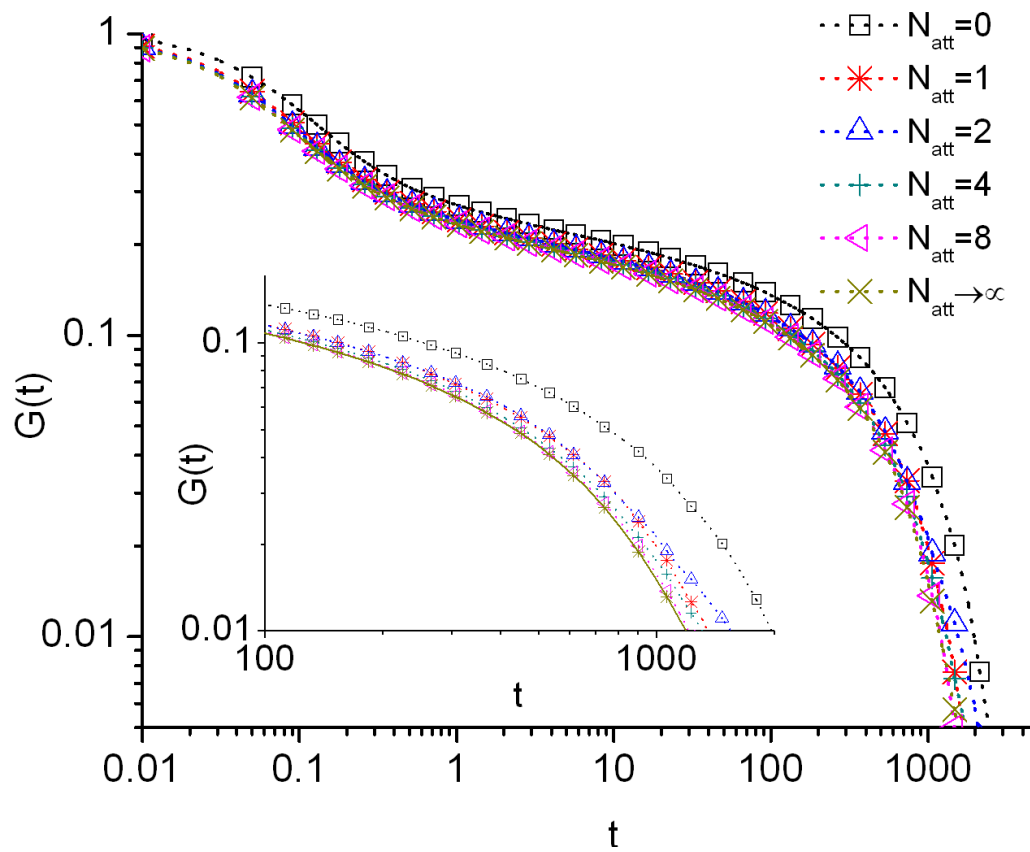


Figure 2.18: The $G(t)$ for $N = 32$, $g' = 1$ and $\Delta t = 0.01$ with different number of attempts, N_{att} . The inset presents an enlargement of the intermediate-time regions.

is because the bead movement has a higher probability to be rejected and hence the bonds are less likely to be re-oriented and therefore it stores the original stress longer. The changes of $\Phi(t)$ are very similar to the of $G(t)$.

Simulation without attempt procedure has shown that it produces a better static properties of the chain. In the dynamics observations, the chain from $N_{\text{att}} = 0$ relaxed slower compared to higher N_{att} . The higher number of N_{att} also contributes to the high bead's density at the centre of the tube. As a result, we will use no attempt procedure through the simulations.

2.7 Conclusions

We have developed Brownian dynamics and dynamic Monte Carlo simulations of the Rouse chain in a sea of fixed obstacles. The predictor-corrector algorithm is used in our simulation where its able to preserve the Gaussian properties of the chains. Regarding to the reattempt procedure, the results from the simulations without attempts have better static property and have slightly slower dynamics. In this chapter, we conclude that we will not use the re-attempt procedure in the uncrossability constraints and will apply the predictor-corrector algorithm in the Brownian dynamics simulations. The Monte Carlo simulations was able to preserve the Gaussian statistics of the chains for the larger Δt as shown in Appendix A. However the dynamics of the chains become slower due to increase of rejection rate, but is is still the fastest overall.

Chapter 3

Static analysis of the Tube

3.1 Introduction

The static analysis includes testing the conformation of the tube as defined by the tube theory by means of simulations. The simulation as discussed in chapter 2. In order to conduct this, we first need to construct the tube, given the chain in an array of obstacles. The conformation of the tube will be examined to obtain tube parameters. The statistics of the tube is analysed such as the average and ‘root-mean-square’ (RMS) length of the tube. The tube length distributions are compared with standard statistical distributions, which allows the tube parameters such as the tube Kuhn step (a), the chain statistical segment length inside the tube (b_{1D}) and the number of beads per entanglement (N_e) to be calculated.

3.2 Tube-like region

We will employ two definitions of the tube:

1. Tube axis: the total length of segments connecting vertices of the tube cells as shown in Fig. 3.1.

2. Primitive path: the shortest path connecting the ends of the chain without violating the constraints.

As the constructions for both methods show some overlap, we will first present their preconstruction in section 3.2.1. Section 3.2.2 will further treat the tube axis and introduce some additional notation. In section 3.2.3, the construction of the primitive path will be given.

3.2.1 Construction of the tube-like region

The tube-like region can be constructed by different ways either for lattice [41,48,61] or off lattice model [21,22,64,65]. Our model is based on the off lattice single chain model. For multi-chain models, the tube region and its primitive path was obtained by using several methods. One of the successful methods is called the ‘annealing’ method [16]. The method consist of 3 steps:

1. The chain ends are fixed in space.
2. The intrachain excluded volume interactions is disabled.
3. The energy of the system is minimized by slowly cooling the system toward $T = 0$. This cause the bonds try to reduce their length to zero and pull the other chains taut.

The other method is the primitive chain network (PCN) [66–68]. The PCN is a 3D network chains where the entanglements are modelled as slip-links joining two chains. Each chain slides through several slip links in the simulation box.

In our model, the tube will be constructed based on the idea proposed by Edwards and Evans [40,62], who introduced the concept of obstacles which are produced by other chains, resulting in a ‘tube’ where the beads move. The physical

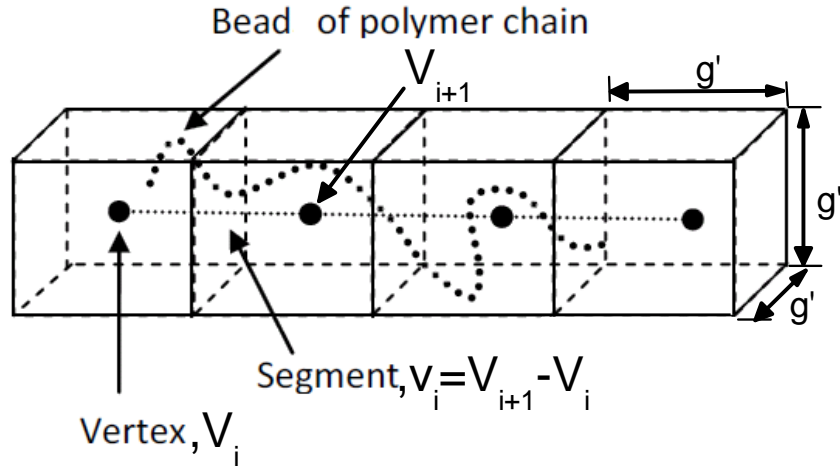


Figure 3.1: Definition of the tube parameters where the tube consist of three segments, $Z^s = 3$.

description of the parameters used in the tube construction is shown in Fig. 3.1 using the following definitions:

- grid g : length of the grid spacing, while g' is dimensionless grid size defined as $g' = \frac{g}{b_{3D}}$.
- vertex \mathbf{V}_i : Cartesian coordinate of the centre of cell i .
- Segment \mathbf{v}_i : vector connecting two consecutive vertices, $\mathbf{v}_i = \mathbf{V}_{i+1} - \mathbf{V}_i$ with $i = 1, \dots, Z^s$, where Z^s is total number of the tube segments with $Z^s + 1$ cells (see Fig. 3.1).

To construct the tube like region, we refer to steps used by Evans and Edwards in their work, where they have constructed a primitive path from the lattice model [62]. Some modifications have been made to suit with our off-lattice model. The steps are as follows. Consider a chain configuration as in Fig. 3.2(a), (for the sake of simplicity, we illustrate the algorithm in 2D, but 3D is analogous).

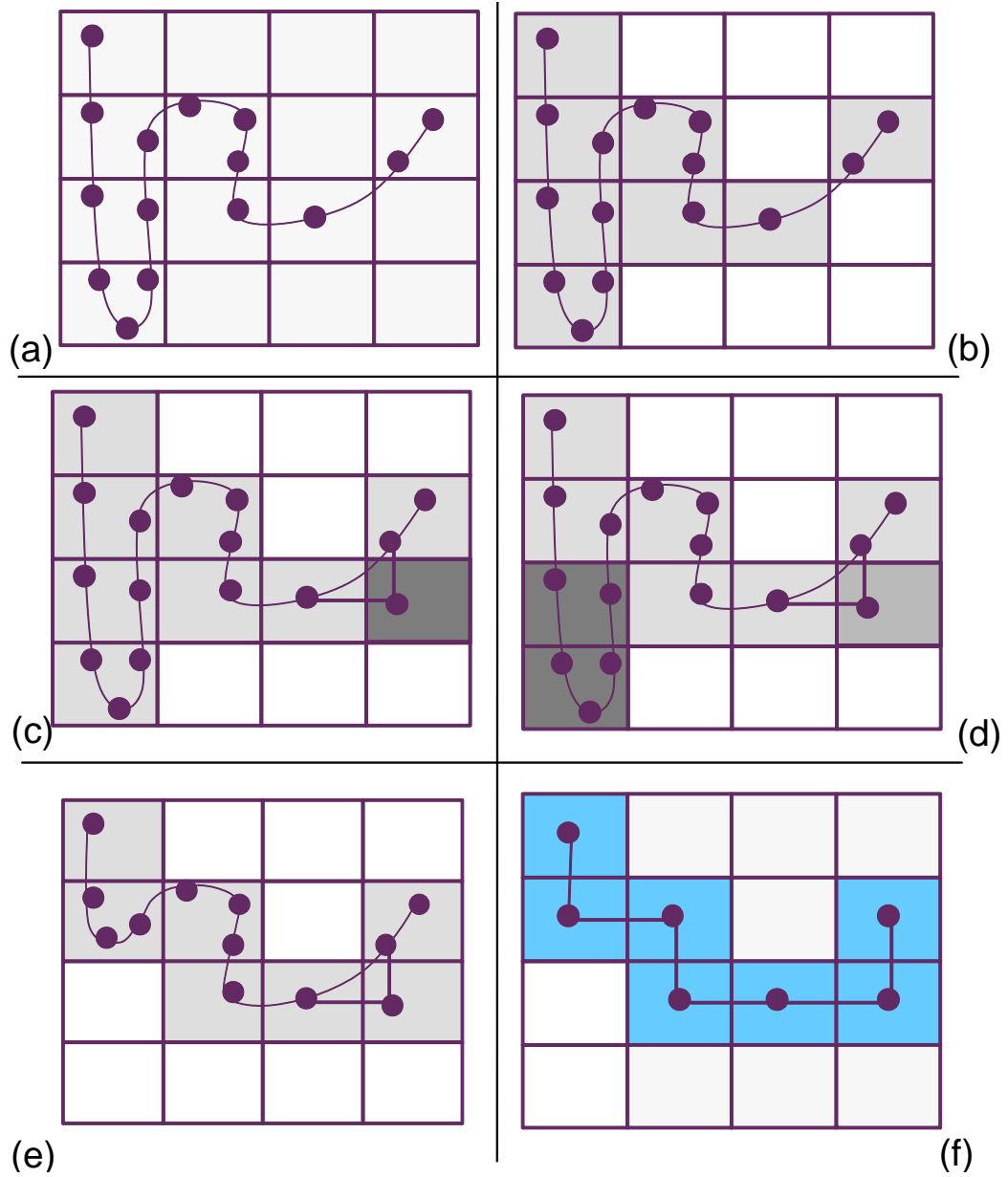


Figure 3.2: Steps in constructing the tube like region.

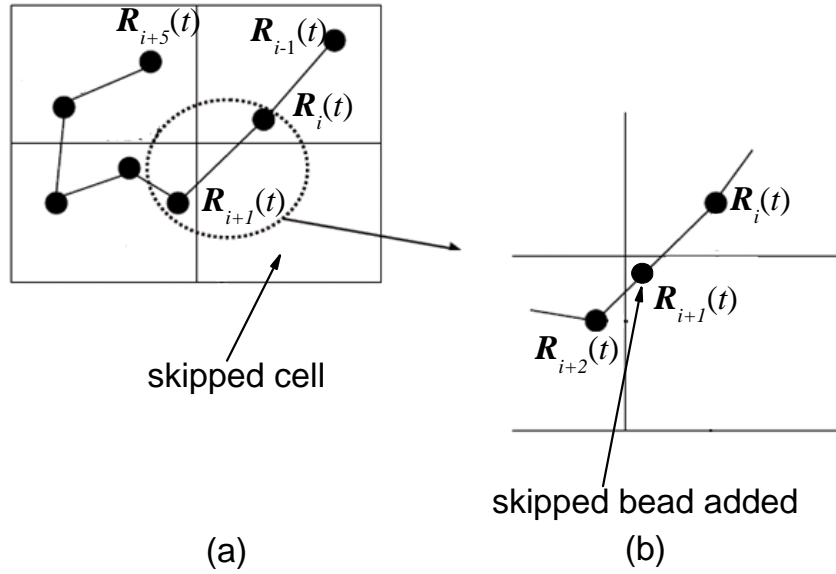


Figure 3.3: (a) Determine the skipped cell. (b) bead $\mathbf{R}_{i+1}(t)$ is added at the skipped cell.

1. The bead coordinate, \mathbf{R}_i is converted into a dimensionless vertices coordinate, $\tilde{\mathbf{V}}_i$ by using

$$\tilde{\mathbf{V}}_{i,\alpha} = (\mathbf{R}_{i,\alpha} - q \times g) + \frac{1}{2} \quad (3.1)$$

where q is the *quotient* of the division between $\mathbf{R}_{i,\alpha}$ and g with $i = 0, \dots, N$. The Greek indices denote the Cartesian components and $\frac{1}{2}$ is added to move the coordinate into the centre of the cell. Since the vertices coordinate $\tilde{\mathbf{V}}_i$ is an integer, therefore, there is a possibility that more than one bead will have the same $\tilde{\mathbf{V}}_i$.

2. The initial tube configuration is determined by marking all the cells that are occupied by $\tilde{\mathbf{V}}_i$, see Fig. 3.2(b).
3. If the segment length $|\mathbf{v}_i| > g$ for $i = 1, \dots, N$ then the bond \mathbf{v}_i has crossed

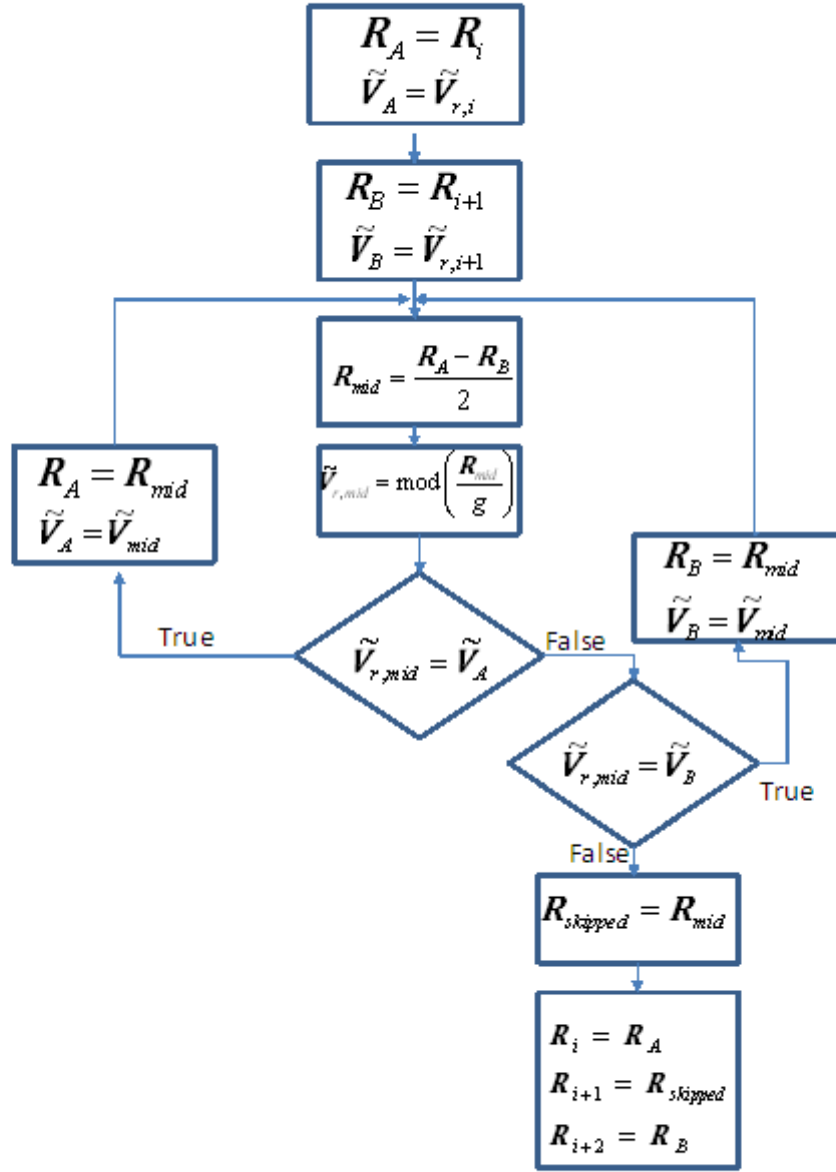


Figure 3.4: Flow chart of recursive middle point calculation. Firstly, two adjacent beads are copied into new variables \mathbf{R}_A and \mathbf{R}_B . Calculating the middle coordinate between \mathbf{R}_A and \mathbf{R}_B gives \mathbf{R}_{mid} and converted to grid base coordinate, $\tilde{\mathbf{V}}_{r,mid}$. If the $\tilde{\mathbf{V}}_{r,mid}$ is located in the same cell with $\tilde{\mathbf{V}}_A$, then the A variables are replaced by *mid* variables. If the checked false then if $\tilde{\mathbf{V}}_{r,mid}$ is in cell $\tilde{\mathbf{V}}_B$, then the B variables are replaced by *mid*. This process is repeated until the mid bead is located neither in $\tilde{\mathbf{V}}_A$ nor $\tilde{\mathbf{V}}_B$. Finally, the skipped bead $\mathbf{R}_{skipped}$ is added between bead \mathbf{R}_i and \mathbf{R}_{i+1} by shift bead \mathbf{R}_{i+1} into \mathbf{R}_{i+2} .

the tube corner as illustrated in Fig. 3.3(a). In this situation, an extra bead is required to make sure the tube segments are the same length. The skipped bead is added by using the algorithm called *recursive middle point calculation* as follows

- (a) Calculate \mathbf{R}_{mid} which is in the middle point between beads \mathbf{R}_i and \mathbf{R}_{i+1} (see Fig. 3.3(b)).
- (b) \mathbf{R}_{mid} is converted into $\tilde{\mathbf{V}}_{\text{mid}}$ using Eq. 3.1.
- (c) If $\tilde{\mathbf{V}}_{\text{mid}}$ is the same coordinate with $\tilde{\mathbf{V}}_i$ then bead \mathbf{R}_i is replaced by \mathbf{R}_{mid} . The same procedure is applied to $\tilde{\mathbf{V}}_{i+1}$.
- (d) Steps, a, b and c (calculate \mathbf{R}_{mid} , convert to $\tilde{\mathbf{V}}_{\text{mid}}$ and compare $\tilde{\mathbf{V}}_{\text{mid}}$ with \mathbf{R}_i and \mathbf{R}_{i+1}) are repeated until the current $\tilde{\mathbf{V}}_{\text{mid}}$ is located neither in $\tilde{\mathbf{V}}_i$ nor $\tilde{\mathbf{V}}_{i+1}$.
- (e) The skipped bead, \mathbf{R}_{mid} is added in cell $\tilde{\mathbf{V}}_{\text{mid}}$.

The detail about the algorithm is presented in Fig. 3.4. Step 1 is repeated to convert \mathbf{R}_i into $\tilde{\mathbf{V}}_i$, ($i = 0, \dots, N'$) where N' is the chain length included the skipped bead

4. Unentangled loops in Fig. 3.2(d) are determined and removed. The unentangled loop is defined as, if vertices, $\tilde{\mathbf{V}}_{i-1}$ and $\tilde{\mathbf{V}}_{i+1}$ are located in the same cell then, $\tilde{\mathbf{V}}_{i-1}$, $\tilde{\mathbf{V}}_i$ and $\tilde{\mathbf{V}}_{i+1}$ are in the unentangled loop. These beads are moved into their root cell, $\tilde{\mathbf{V}}_{i-1}$. This process is repeated until all the unentangled loops are removed and the tube configuration is constructed as illustrated in Fig. 3.2(e).
5. Finally, the beads in cell $\tilde{\mathbf{V}}_i$ are replaced by one vertex point \mathbf{V}_i shown in Fig. 3.2(f). The tube consist of $\{\mathbf{V}_i\} = (\mathbf{V}_0, \dots, \mathbf{V}_{Z^s})$ with $Z^s = 6$ as in Fig.

3.2(f).

3.2.2 Tube axis

The tube like region consist of numbers of tube cells (see Fig. 3.5), thus the tube axis is defined as a path produced by connecting the middle of the cells of the tube.

Contour length of the tube axis is defined as:

$$L_g = \sum_{i=0}^{Z^s-1} |\mathbf{v}_i| = Z^s g \quad (3.2)$$

which means that in average:

$$Z_{\text{av}}^s g a = N b_{3\text{D}}^2 \quad (3.3a)$$

$$Z_{\text{av}}^s = \frac{N b_{3\text{D}}^2}{a g} \quad (3.3b)$$

The Z_{av}^s in Eq. 3.3b is not the number of entanglements since the entanglements are usually associated with the number of turns of the tube path. Thus we cannot use Z_{av}^s directly into the tube theory. \widehat{Z}^s is defined as $\widehat{Z}^s = \langle Z^s \rangle$ and $\Delta \widehat{Z}^s = \langle (\Delta Z^s)^2 \rangle^{1/2}$ with

$$(\Delta Z^s)^2 = \left\langle \left(Z^s \right)^2 \right\rangle - \left(\widehat{Z}^s \right)^2 \quad (3.4)$$

where $\langle \dots \rangle$ is the average over the number of conformations of the tube segments.

By using Eqs. 1.36 and 1.48, the tube parameters are defined as:

$$a^g = \frac{N b_{3\text{D}}^2}{\widehat{Z}^s g} \quad (3.5)$$

$$b_{1\text{D}}^g = \sqrt{\frac{3(\Delta \widehat{Z}^s)^2 g^2}{N}} \quad (3.6)$$

3. The number of beads for each tube cell is added so that total number of beads in each cell is n_b , giving a total number of N' beads per chain with $N' = (Z^s + 1) \times n_b$. The beads are located inside the cell in accordance to the following procedures:
 - (a) Construct the tube for its initial chain configuration (at $t = 0$).
 - (b) The tube cell is divided into n_b sub-segments as shown in Fig. 3.6.
 - (c) The n_b beads are distributed equally for each tube cell with one bead per sub-segment except for the sub-segments adjacent to the tube ends. For simplicity, we use the centre of each sub-segment as coordinate for the added bead. As an example, for $n_b = 3$ as shown in Fig. 3.6, firstly, the cell is divided into 3 segments (see Fig 3.6(a)), then beads are added at the segments except for the end bead of the chain, as shown in Fig. 3.6(b).
 - (d) Step 3(b) is repeated for all cells in the tube.

4. We study two methods of obtaining the primitive path. The first is by using the ‘annealing’ method. The energy of the system is minimised by slowly cooling down the system. At each time step, the temperature is exponentially decreased which resulted in the shrinking of the bond lengths. This process is repeated until $T \rightarrow 0$, thus, it requires a longer time to obtain the shortest contour length. The second method is by initially using $T = 0$ and immediately reducing (shrinking) the bond lengths without the violation of constraints. The bonds are allowed to move along the constraints until the shortest path is obtained. In this project, we use the second method because it is faster in obtain the shortest path.

5. The contour length L^{PP} between $\mathbf{R}_0, \dots, \mathbf{R}_{N'}$ is obtained by summing all bond

lengths:

$$L^{\text{PP}} = \sum_{i=0}^{N'-1} |\mathbf{R}_i - \mathbf{R}_{i+1}| \quad (3.7)$$

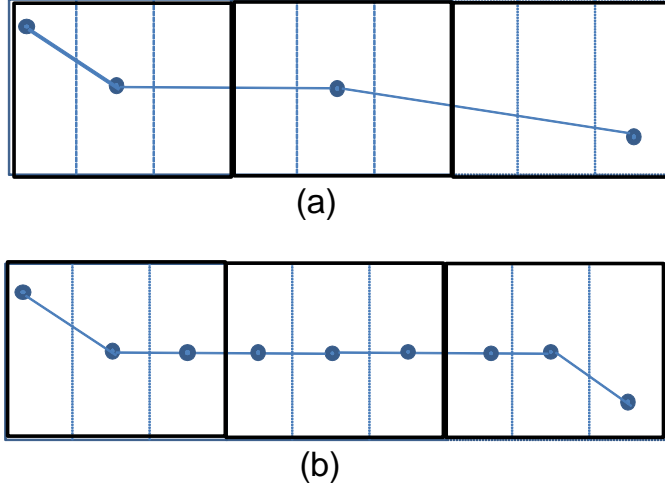


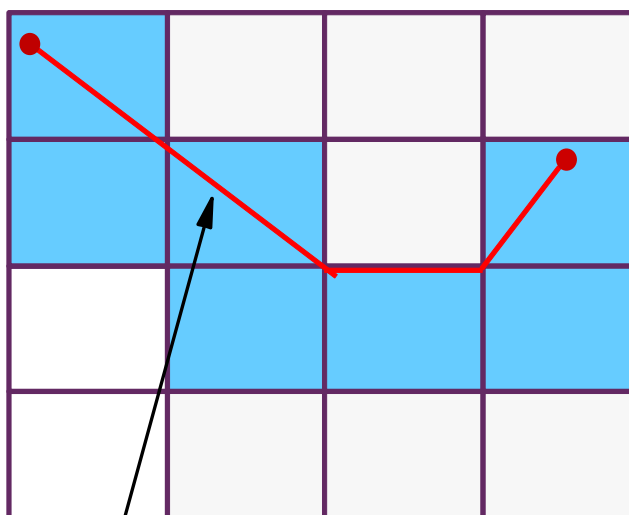
Figure 3.6: Example of adding $n_b = 3$ per tube cell. The cell is divided into n_b sub-segments (Fig. (a)). The beads are added into the sub-segments, Fig (b).

We have conducted an analysis to determine which n_b is required for each grid size. Table 3.1 shows the primitive path length with different n_b and grid sizes. We found that for $g' > 1$, increasing the n_b results will decrease the primitive path length. However, the changes of primitive path length is smaller for the higher n_b . As a result, we use n_b which gives a large change of the primitive path length. As a result we used $n_b = 2, 4, 6$ for $g' = 1, 2, 4$ respectively.

The construction of the primitive path is shown in Fig. 3.7. The definitions of the tube Kuhn step a^{PP} , the chain statistical segment length inside the tube $b_{1\text{D}}^{\text{PP}}$ and number of beads per entanglement N_e^{PP} are similar with Eqs. 3.5, 3.6 and 1.37, respectively, by substituting $\widehat{Z}^s g$ with \widehat{L}^{PP} and $\Delta \widehat{Z}^s g$ with $\Delta \widehat{L}^{\text{PP}}$.

Table 3.1: Number beads per cell for each grid sizes with $N = 128$ based on statistics of 300 chains.

grid	n_b	Length of Primitive Path
1	1	61.508
	2	61.964
	4	62.083
2	1	32.487
	2	31.952
	4	31.880
	6	31.909
4	1	18.711
	2	18.563
	4	18.593
	6	18.576
	8	18.580



Primitive path

Figure 3.7: Primitive path of the tube. The Rouse chain is given in 3.2(a).

3.3 Probability distribution of the tube length

The probability distribution of the tube length is available in section 1.10.6. The negative of natural logarithm of Eq. 1.46 gives:

$$\ln(P(L, N)) = -\ln\left(\frac{1}{2\pi\Delta\hat{L}^2}\right)^{1/2} + \frac{(L - \hat{L})^2}{2\Delta\hat{L}^2} \quad (3.8a)$$

$$= \frac{L^2}{2\Delta\hat{L}^2} - \frac{L\hat{L}}{\Delta\hat{L}^2} + \frac{\hat{L}^2}{2\Delta\hat{L}^2} - \frac{1}{2}\ln\left(\frac{1}{2\pi\Delta\hat{L}^2}\right) \quad (3.8b)$$

Expression 3.8b can be used to obtain the Gaussian parameters such as \hat{L} and $\Delta\hat{L}$ [69]. In our simulation, Eq. 3.8b is valid for shallow fluctuations around \hat{L} . However, for deep fluctuations, the potential experienced by the chain ends is not as specified by Eq. 1.45 [47]. This is because in the limit of very long chain, $N \gg g'$, the probability to form a loop where there are no entanglements and its ends are in the same cell [49]. As a result Eq. 3.8b can be simplified when $L = 0$ and transform back it into original expression, Eq. 1.46 gives:

$$P(L = 0, N) = \exp\left(\frac{\hat{L}^2}{2\Delta\hat{L}^2} - \ln\left(\frac{1}{2\pi\Delta\hat{L}^2}\right)^{1/2}\right) \quad (3.9a)$$

$$= \left(\frac{1}{2\pi\Delta\hat{L}^2}\right) \exp\left(\frac{\hat{L}^2}{2\Delta\hat{L}^2}\right) \quad (3.9b)$$

Assuming $a \approx g$, $b_{3D} = 1$ then we obtain $N_e \approx (g')^2$, knowing that $\hat{L} = \hat{Z}g$ and $\Delta\hat{L} = \Delta\hat{Z}g$. Thus from Eq. 3.9b we obtain

$$P(0, N) = c \left(\frac{N}{g^2}\right)^{-1/2} \exp\left(-\beta\frac{N}{g^2}\right) \quad (3.10)$$

with two unknown parameters, c and β . These parameters for the 2D and 3D lattice models available in [41, 49], respectively. In this project, parameter β is obtained by

using the following steps:

1. Fit the natural logarithm of $P(L, N)$ with Eq. 3.8b as shown in Fig. 3.8 for the tube axis, $P(Z^s, N)$ with $N = 512$, and $g = 4$. The dashed line represents the fitting at $Z^s \approx \widehat{Z}^s$ and the solid line is at small Z^s . The fitting is represented by Eq. 3.8b, then the intersection at y -axis which represent $P(0, N)$ is obtained. This process is repeated for all chain lengths and grid sizes as shown in Figs. 3.9 for $g' = 1$ and $g' = 2$.

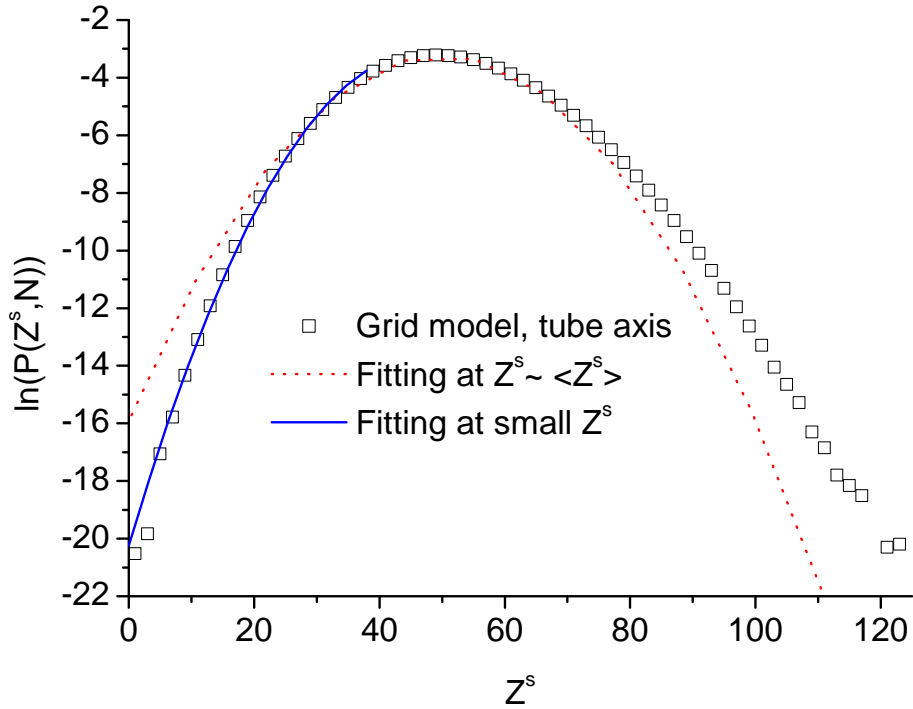


Figure 3.8: The natural logarithm of the data for $P(Z^s, N)$ with $N = 512$, $g' = 4$, $\langle Z^s \rangle = 50.18$. The solid and dashed lines are the regions to obtain the $P(0, N)$. The dashed line is the fitting at the peak region of the distribution.

2. In each grid size, the $P(0, N)$ are fitted with Eq. 3.10 to obtain the parameters, c and β . This is shown by the dashed lines in Fig. 3.9 for the tube axis with $g' = 1$ and $g' = 2$ which gives $\beta = 0.3$, $c = 0.3$ for $g' = 1$ and $\beta = 0.4$, $c = 0.4$ for $g' = 2$. The β and c for all grid sizes are presented in Table 3.2.

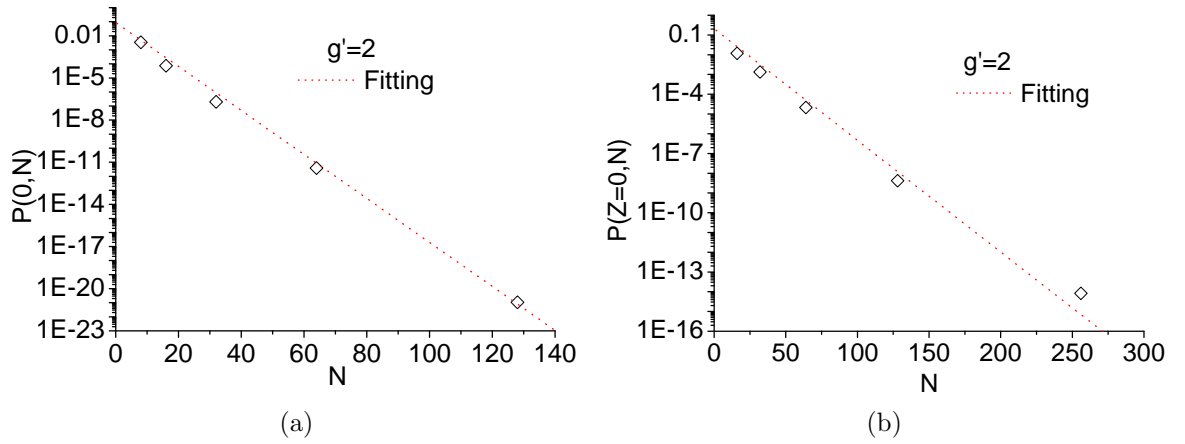


Figure 3.9: $P(Z = 0, N)$ as a function of N for $g' = 1$ (Fig. 3.9(a)) and $g' = 2$ (Fig. 3.9(b)). The dashed lines are the data fitting with Eq. 3.10.

If the potential is obtained from the dashed lines, the parameters in Eq. 3.10 (in this case, they are represented by β^T and c^T) can be calculated analytically by using Eqs. 1.46 and 3.10 where:

$$\beta^T = \nu \frac{b_{3D}^4 g^2}{b_{1D}^2 a^2} \quad (3.11)$$

$$c^T = \left(\frac{3}{2\pi g^2 b_{1D}^2} \right)^{1/2} \quad (3.12)$$

with $\nu = 3/2$. Table 3.2 present β^T and c^T for all grid sizes. By identifying the simulation value β and the theoretical value β^T , the difference between them is given below:

$$\Delta\beta = |\beta - \beta^T| \quad (3.13)$$

which shows how large the potential in the model deviate from the ideal Gaussian distribution (fitting at $Z \approx \hat{Z}$).

3.4 Analysis and Discussion

3.4.1 Probability distribution of the tube length

The tube theory assumes that the tube length is Gaussian distributed (Eq. 1.46) and by using our model, we are able to test this assumption and to see deviations from the Gaussian approximation [41, 49, 70, 71].

Figs. 3.10 and 3.11 show the probability distributions of the tube length for the tube axis and the primitive path which are normalised with \widehat{Z}^s , $\Delta\widehat{Z}^s$ and \widehat{L}^{pp} , $\Delta\widehat{L}^{pp}$, respectively. The predicted ideal Gaussian is included to show the derivations from Gaussianity (the dashed lines).

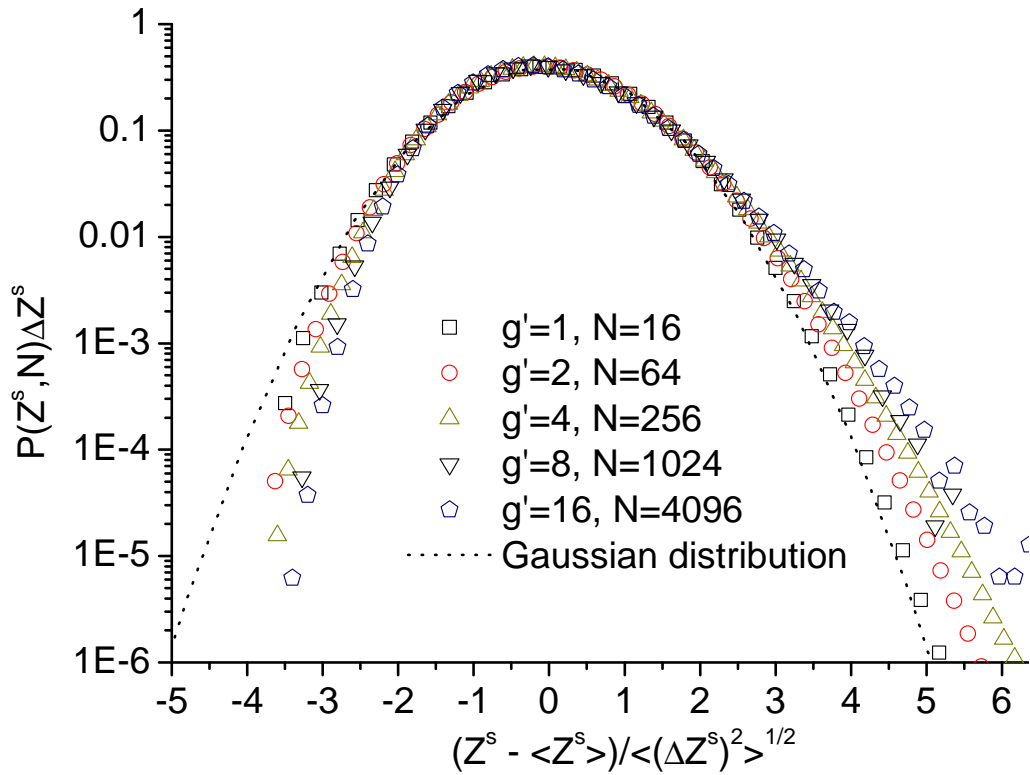


Figure 3.10: Semi-log scale, normalised distribution of number of tube segments \widehat{Z}^s for $g' = 1, 2, 4, 8, 16$ with $N = 16, 64, 256, 1024, 4096$, respectively. The dashed line is the normalised Gaussian distribution. The data are based on 1×10^6 configurations.

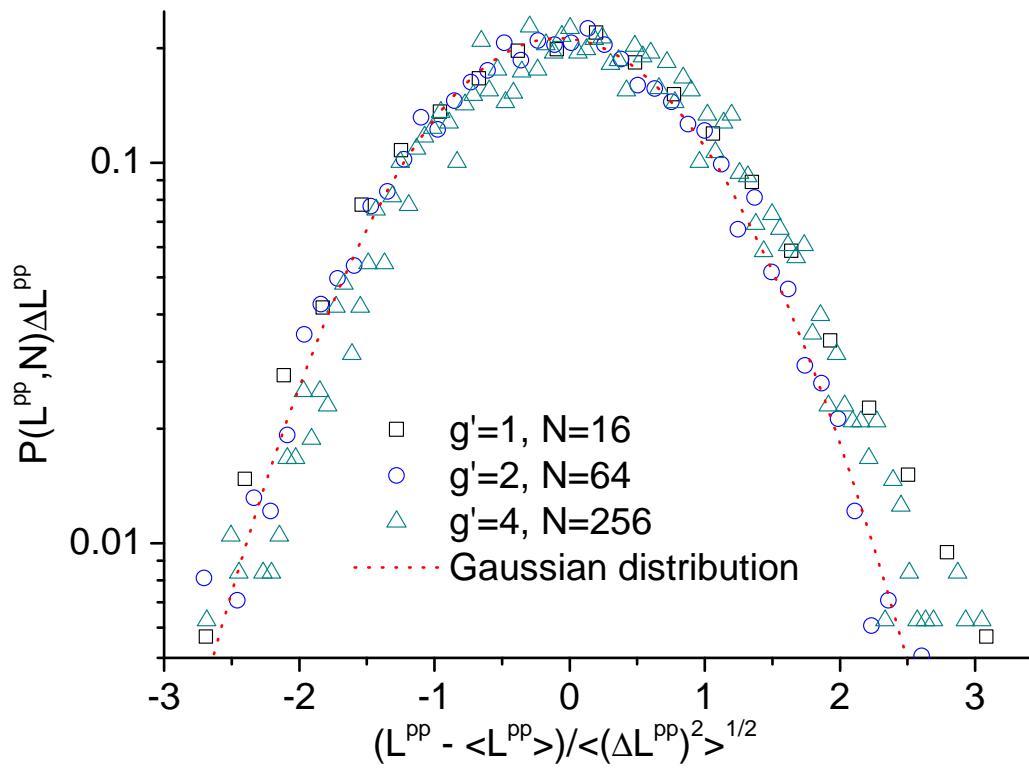


Figure 3.11: Semi-log scale, normalised distribution function of the primitive path length, \hat{L}^{pp} for $g' = 1, 2, 4$ with $N = 16, 64, 256$, respectively. The dashed line is the normalised Gaussian distribution. The data are based on 1000 configurations.

In tube axis and primitive path methods, their probability distributions are well approximated by Gaussian at the probability larger than 0.01. In case of the tube axis, we are able to observe very small probabilities in the distribution function (see Fig. 3.10). Hence both deep retractions $Z^s \ll \widehat{Z}^s$ and stretching $Z^s \gg \widehat{Z}^s$ are visible. For $g' = 1$, all chain lengths behave Gaussian with very small deviations occurring especially for the longest chain, $N = 128$. The deviations are clearly visible for $g' = 2, 4, 8, 16$ especially for the longer chains. The results show that it is less probable to find a tube with shorter Z^s than predicted by Gaussian. On the other hand, a larger value of Z^s has a higher probability to occur. The deviation for deep retractions implies that the effective potential in our model is stronger than the ideal quadratic potential (Eq. 1.46). This is in qualitative accordance with the literature lattice model, which observed the potential was stronger than the ideal Gaussian distribution with a 20% deviation [48, 49]. Although there are some differences from the Gaussian prediction, these are only visible at a very low probability. As such, for probabilities larger than 0.01, our model shows a good fit with the Gaussian distribution.

The probability distribution of the primitive path length for all chain lengths and grid sizes is shown in Fig. 3.11. The data are noisier because they require a huge number of tube conformations to obtain good statistics. The drawback of the primitive path method is that longer time is required to do the analysis, as it is required to minimize the contour length.

The degree of deviation from the ideal quadratic potential is determined by the parameter $\Delta\beta$ in Eq. 3.13. Table 3.2 presents the value of β_g , β_g^T and $\Delta\beta_g$ for the grid model. β_g^T and c_g^T are obtained by using Eqs. 3.11 and 3.12, respectively, with b_{1D}^g and a are from the static analyses of the tube axis. Fig. 3.12 shows the β_g^T as a function of $1/N$ and the extrapolated values are obtained.

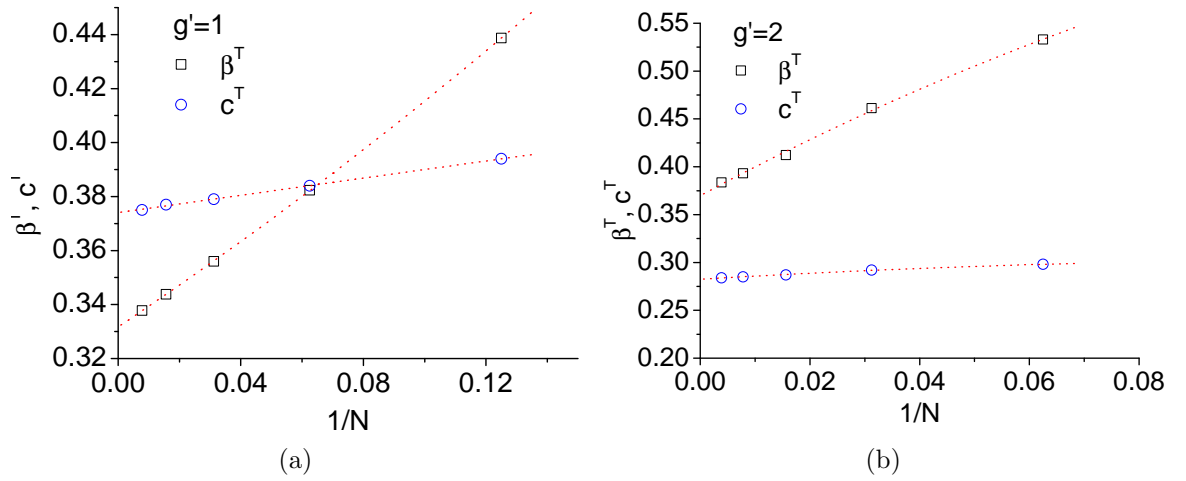


Figure 3.12: β^T and c^T as a function of $1/N$ for $g' = 1$ and $g' = 2$ are in 3.12(a) and 3.12(b), respectively. These are based on the tube axis statistics.

In the lattice model by Zheligovskaya et al., the parameter β_L is available in [49] and β_L^T is obtained by using Eq. 3.18. The trend of β and β^T as a function of $1/\sqrt{g}$ for both models are shown in Fig. 3.13. In the grid model, the deep retractions for small grid sizes are well presented by the ideal Gaussian distribution. However, for the larger grid size $g \geq 4$ the deviations are visible. On the other hand, the lattice model shows the agreement is improving for the larger lattice size. This is due to the anisotropic properties of the lattice model where the segments are not allowed to fold back. In the limit of $g \rightarrow \infty$, both models approximately have $\beta = 0.6$ (see Fig. 3.13).

The lattice model is where the beads of the chain are situated at the lattice points thus the bonds have the same length and they independent with each other. The example of 2D lattice model with 5 segments is shown in Fig. 3.14.

The analysis shows that a non-quadratic correction for a full retraction potential is required. Examples of the correction are available in [47]. However, for the linear chains the correction is not so important as the deviation only occurs at probability smaller than 0.1. The non-quadratic correction is important for branch polymers

Table 3.2: Parameters c and β from the grid model

grid	fitting at $Z^s \ll \widehat{Z}^s$		fitting at $Z^s \approx \widehat{Z}^s$		$\Delta\beta$
	c_g	β_g	c_g^T	β_g^T	
1	0.3	0.30	0.37	0.33	0.03
2	0.4	0.40	0.3	0.40	0
4	0.4	0.50	0.23	0.40	0.10
8	0.4	0.55	0.2	0.40	0.15
16	0.4	0.60	0.16	0.43	0.17
32	0.4	0.60	0.18	0.47	0.13

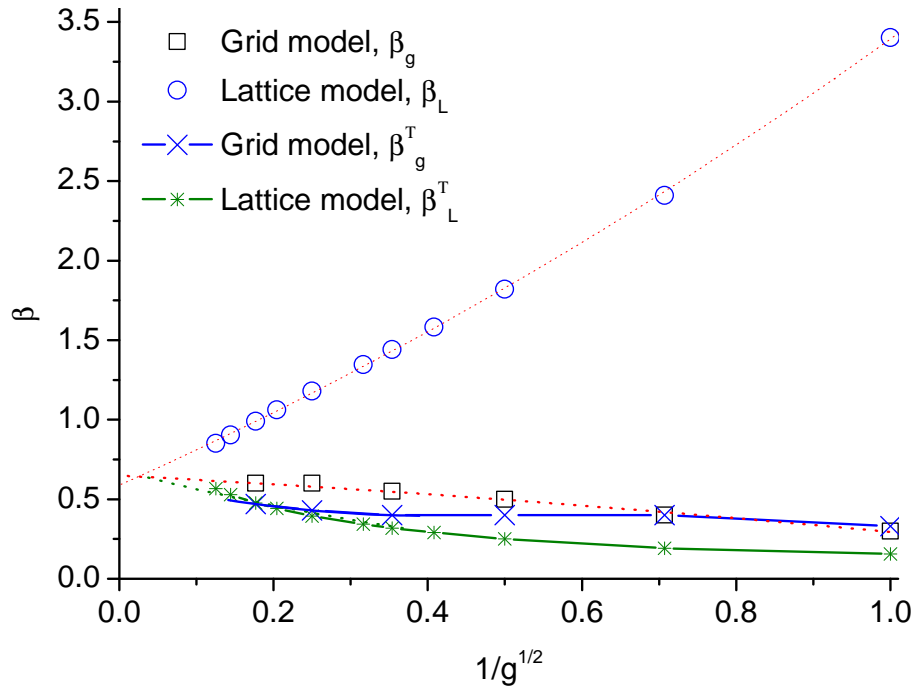


Figure 3.13: Parameter β from the grid and lattice model by Zheligovskaya et al as a function of $1/g^{1/2}$. In the limit of a very large g , β in both models approximately equals to 0.6.

where the relaxation of the arms depends on such extreme fluctuations to relax their entangled conformations. Also, many important rheological properties such as the stress relaxation modulus are governed by the deep fluctuations. We would disregard the non-quadratic correction since we focus solely on linear chain.

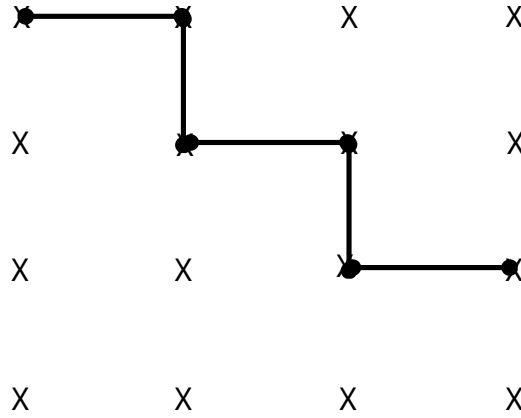


Figure 3.14: Two dimensional representation of a chain on the lattice model. The chain consist of 5 segments.

3.4.2 Mean square spatial distance

The purpose of this section is to observe whether the conformation of the tube segment can be represented by an ideal random walk or an ideal non-folding back random walk. The tube theory assumes the conformation is Gaussian on a large length scale [9, 62], and Rubinstein and Helfand mention that the statistics are a non-folding back random walk [41].

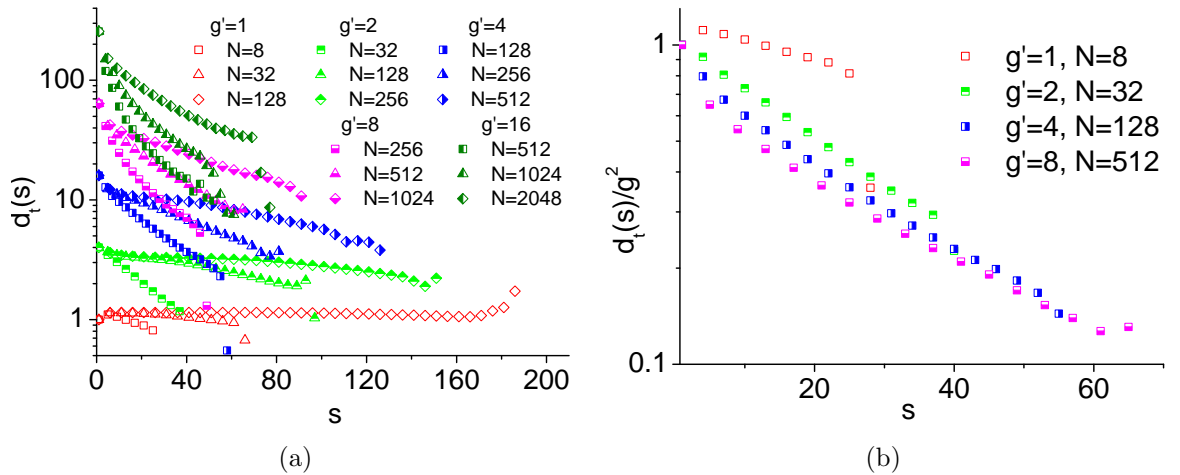


Figure 3.15: Mean square spatial distance of the tube axis as a function of cell separation s for various grid sizes in Fig. 3.15(a) and normalised by g^2 , in 3.15(b)

The analysis is carried out by using Eq. 1.51. The average square of the internal distance $d_t(s)$ between cell i and j for $g' = 1, 2, 4, 8, 16$ are shown in Fig. 3.15(a). In $g' = 1$, a plateau region for long chains is visible which is equal to the average square of the tube Kuhn segment $(a^g)^2$. For the larger g' , the patterns are: $d_t(s)$ increases from $s = 1$ until $s = 2$, then it decreases, after which a plateau is reached and finally it decreases again. The increased section is due to the non-folding back property of the tube segments and the decreased section means that there is a long range effective interaction between the segments. This observation means that the conformations of the segments obey neither ideal random walk nor ideal non-folding back statistics.

The scaling of $d_t(s)$ at different grid size is studied in Fig. 3.15(b), where the focus is on $\widehat{Z}^s \approx 8$ with $N = 8, 32, 128, 512$ for $g' = 1, 2, 4, 8$, respectively. The normalised $d_t(s)$ over the grid size shows that they collapse upon each other except for $g' = 1$, which indicates that the grid dependence disappears in the limit of a large grid size.

3.4.3 Average tube length and its fluctuations

The tube has a different length in every chain conformation, thus its average fluctuations $\Delta\widehat{Z}^s$ can be obtained either by using the definition in Eq. 3.4 or by fitting the top region of the $P(Z^s, N)$. An example of the fitting for the tube axis with $g' = 4$, $N = 512$ is shown in Fig. 3.16 where the solid lines represent the fitting regions. The results from these methods show that they produce approximately the same $\Delta\widehat{Z}^s$. In the following analysis, the first method (Eq. 3.4) is implemented because the $(Z^s)^2$ and \widehat{Z}^s are calculated during simulations.

Two tube parameters, a^g and b_{1D}^g can be derived from \widehat{Z}^s and $\Delta\widehat{Z}^s$, respectively, (see Eqs. 3.5 and 3.6). Fig. 3.17 shows the parameters for each grid size as a

function of g^2/N . The a^g and b_{1D}^g are almost linearly change with g^2/N then their extrapolated values are obtained which presented in Table 3.3. Indeed, if $a^g \approx g$ and $b_{3D}^2 = 1$, then g^2/N is the expected inverse number of entanglements.

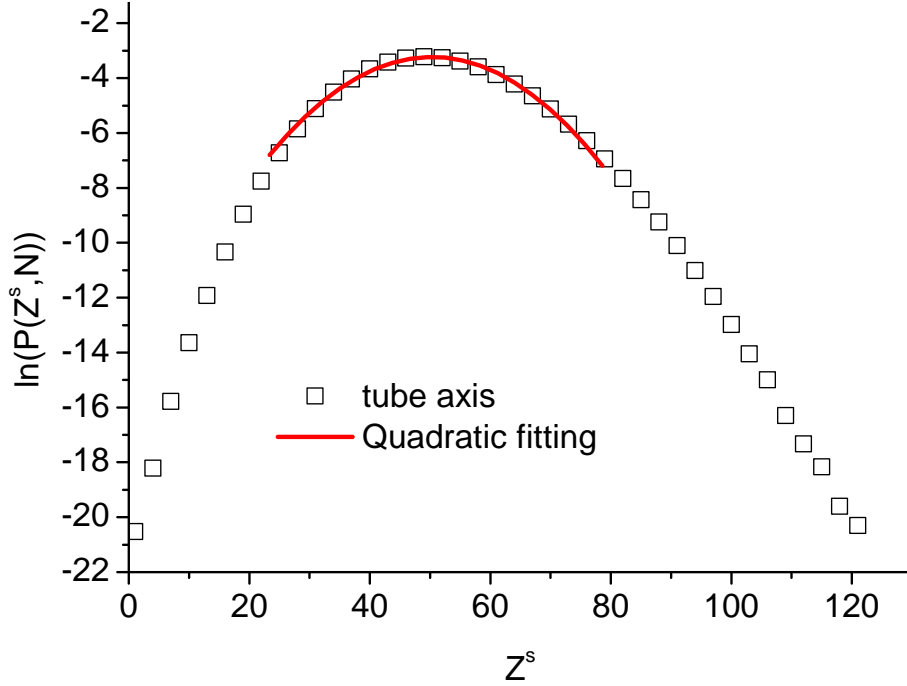


Figure 3.16: Natural logarithm of the data for $P(Z^s, N)$ with $N = 512$ and $g' = 4$. The solid line is the fitted region. The Gaussian parameters obtained from the fitting are $\hat{Z}^s = 50.184$ and $\Delta\hat{Z}^s = 10.04$.

The variation of the primitive path length is calculated by using Eq. 3.4 with \hat{Z}^s and Z^s are replaced by \hat{L}^{pp} and L^{pp} , respectively. The process to obtain the extrapolated tube parameters for the primitive path, a^{pp} and b_{1D}^{pp} is similar with the tube axis (see Fig. 3.18). The values of the parameters are shown in Table 3.3. An interesting feature found in the b_{1D}^{pp} is that the dependence on g' is not too obvious.

In Figs. 3.5 and 3.7, we see that the contour length of the tube axis is longer than that of the primitive path for the same grid size and chain length, thus the Kuhn step of the tube axis is smaller than that of the primitive path. This property is clearly illustrated in Fig. 3.19(a). The normalised a^g and a^{pp} by g , show their

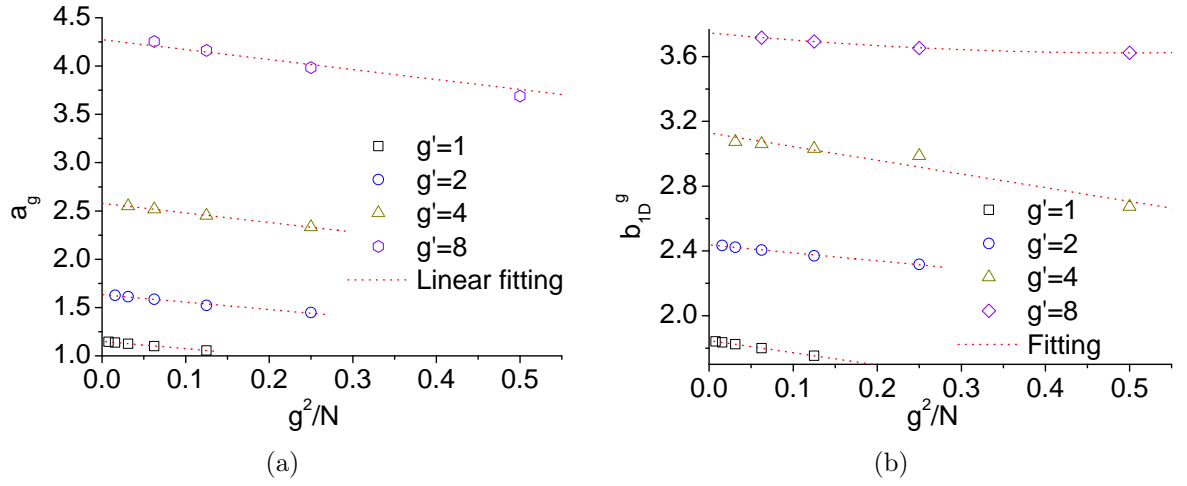


Figure 3.17: Tube Kuhn step for the tube axis, a^g as a function of g^2/N where the asymptotic value, $N \rightarrow \infty$ for each grid size is obtained in Fig. 3.17(a). The same procedure is applied for the b_{1D}^g , Fig. 3.17(b).

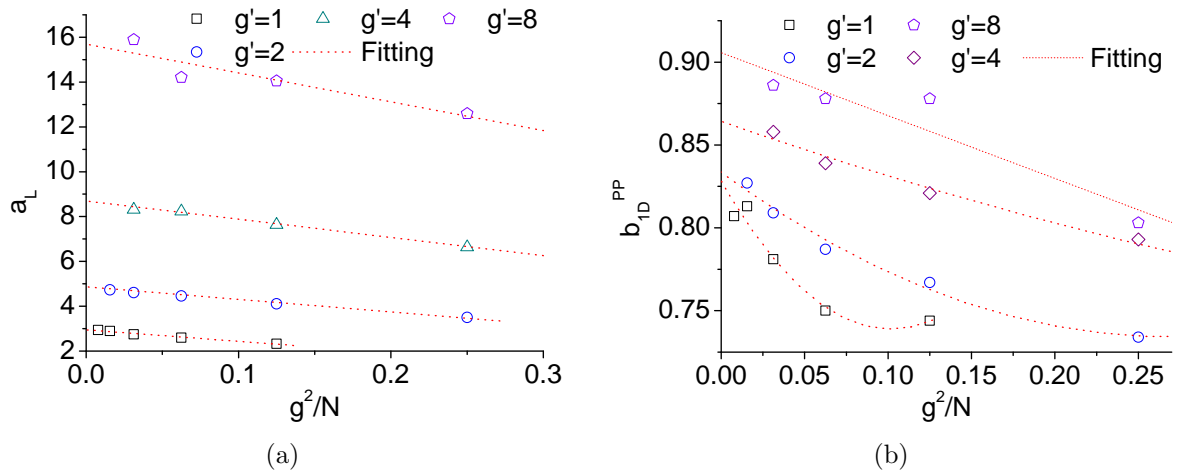


Figure 3.18: Kuhn step for the primitive path, a^{PP} as a function of g^2/N where the asymptotic value, $N \rightarrow \infty$ for each grid size is obtained in Fig. 3.18(a). The same procedure is applied for b_{1D}^{PP} , Fig. 3.18(b).

Table 3.3: The extrapolated value of a and b_{1D} for each grid size from the tube axis and the primitive path.

grid size	a^g	a^{PP}	b_{1D}^g	b_{1D}^{PP}
1	1.151	2.997	1.848	0.828
2	1.646	4.812	2.443	0.833
4	2.586	8.702	3.09	0.864
8	4.351	16.313	3.746	0.906
16	7.681		4.399	
32	13.905		5.055	
64	25.695		5.544	

scaling as $a^g \propto g$ and $a^{PP} \propto g$ for $g \gg 1$.

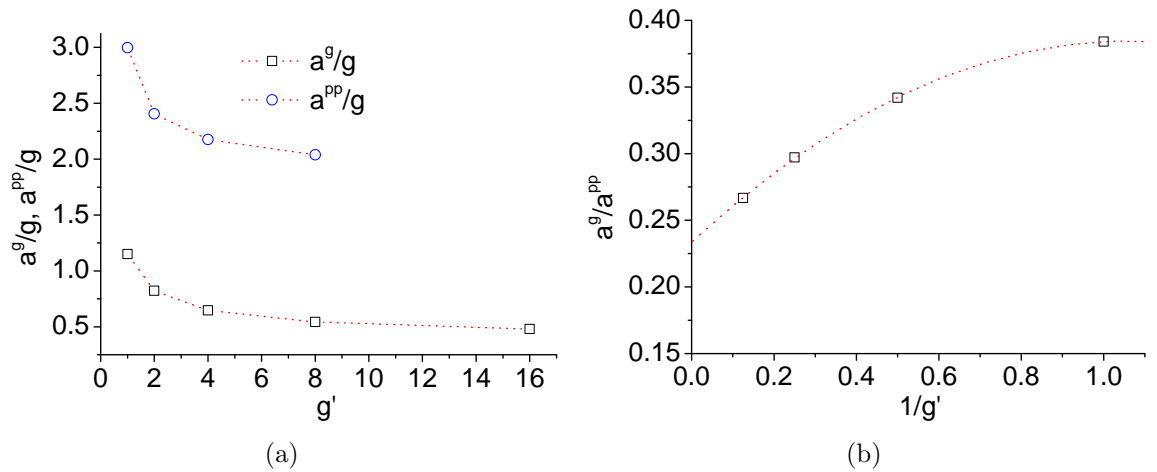


Figure 3.19: The Kuhn segment length from the tube axis, a^g and the primitive path, a^{PP} normalised by g' as a function of g' are in Fig. 3.19(a). The ratio of these Kuhn segments versus $1/g$ is shown in Fig. 3.19(b).

Further analysis was conducted by taking the ratio between a^g and a^{PP} as in Fig. 3.19(b). In limit of $g' \rightarrow \infty$, the a^g is about factor 2.5 smaller than a^{PP} . The number of beads per tube cell, N_e from the tube axis and the primitive path for each grid size are presented in Table 3.4.

In Fig. 3.20, the b_{1D}^g for all grid sizes is greater than 1.0 and slowly change with g' approximately scaled as $g'^{1/4}$ and approach $b_{1D}^g = 9.1$ for $g' \rightarrow \infty$. On the other hand, $b_{1D}^{PP} < 1.0$ and seem almost constant with g' . Within all grid sizes, b_{1D} which

Table 3.4: Average number of beads per entanglement, N_e for each grid size from the tube axis and the primitive path.

grid	N_e^g	N_e^{PP}
1	1.325	8.963
2	2.707	23.138
4	6.684	75.242
8	18.881	280.98
16	58.717	
32	193.77	
64	660.01	

obtained from the tube axis and the primitive path are not equal to b_{3D} as predicted by the tube theory.

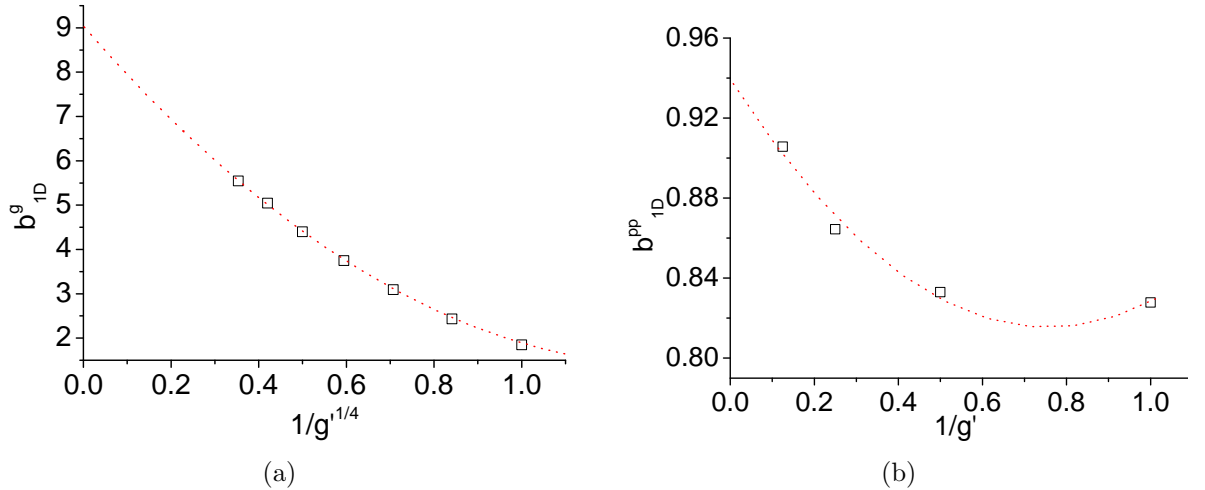


Figure 3.20: The extrapolate value for b_{1D}^g and b_{1D}^{PP} in Fig. 3.20(a) and 3.20(b), respectively.

3.5 Comparison with the lattice model

A very similar approach to our study is the lattice model. In the literature, there are two studies for this lattice model, i.e, Rubinstein and Helfand [41] for 2D lattice and Zheligovskaya et al. [49] for the 3D. We are interested to obtain the tube parameters from these models and compare them with our results. Since our model is in 3D, we

only refer to the work by Zheligovskaya et al. The description of the parameters in the lattice model is presented in Table 3.5. We also developed our 3D lattice model and used exactly the same procedure as in the grid model.

Table 3.5: Parameters under study

Description	Grid Model	Zheligovskaya et al
Grid or lattice spacing	g	m
Average number of tube segments	\widehat{Z}	k_0
Instantaneous number of tube segments	Z	k
Number of beads /chain length	N	N
Number of beads per cell	N_e	G_0
Tube parameters	a_g and b_{1D}	γ and β

The distribution of the tube length was approximated around the most probable value k_0 by [49]

$$P(k) = \sqrt{\frac{\gamma}{2\pi k_0}} \exp\left(-\frac{\gamma}{2k_0}(k - k_0)^2\right) \quad (3.14)$$

By comparing it with Eq. 1.46 for the grid model, the relationship between the parameters are

$$k_0 = \frac{Nb_{3D}^2}{ga^g} \quad (3.15)$$

$$\frac{\gamma}{k_0} = \frac{1}{(\Delta\widehat{Z})^2} \quad (3.16a)$$

$$= \frac{3g^2}{N(b_{1D}^g)^2} \quad (3.16b)$$

thus

$$\gamma = \frac{3gb_{3D}^2}{a^g(b_{1D}^g)^2} \quad (3.17)$$

and β_L^T is obtained by using Eqs. 3.14 and 3.10:

$$\beta_L^T = \frac{\gamma b_{3D}^2 g}{2a^g} \quad (3.18)$$

From Eqs. 3.15 and 3.17, the parameters a^g and b_{1D} from k_0 and γ are obtained by taking into account that $k_0 = \frac{N}{g_0 g^2}$ where $g_0 = \frac{G_0}{g^2}$, thus:

$$a^g = \frac{N b_{3D}^2}{g k_0} = b_{3D}^2 g_0 g \quad (3.19)$$

$$b_{1D}^2 = \frac{3 g b_{3D}^2}{a \gamma} = \frac{3}{g_0 \gamma} \quad (3.20)$$

The a^g from the models are presented in Fig. 3.21(a). In the limit of $g \gg 1$, our lattice model and the grid model almost agree to each other.

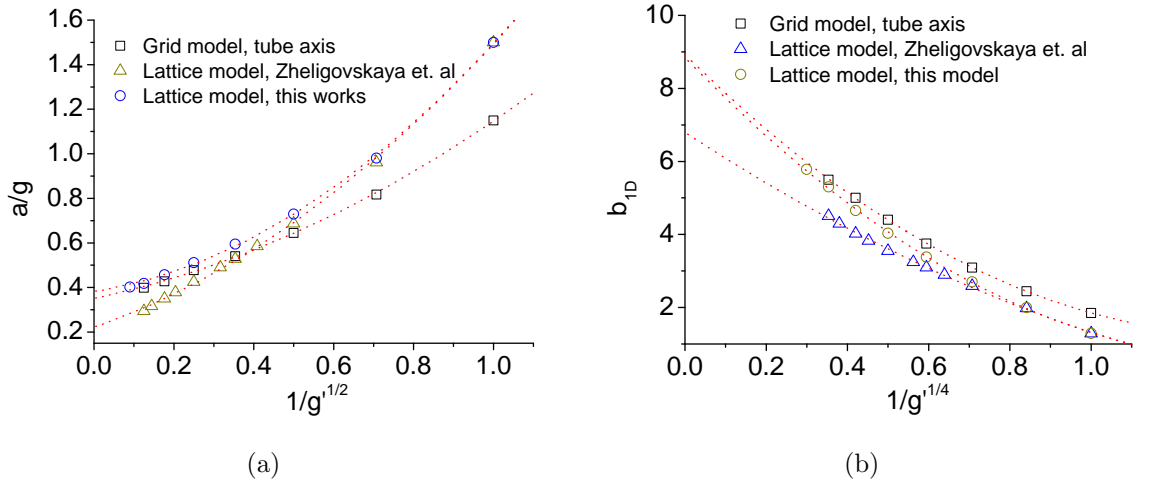


Figure 3.21: Tube Kuhn step normalised by g from the grid and the lattice models as a function $1/g^{1/2}$ in Fig. 3.21(a). b_{1D} from the models show they approximately scale with $g^{1/4}$ in Fig. 3.21(b).

The b_{1D} in all models are scaling with $g^{1/4}$ but the lattice model by Zheligovskaya et al. deviate at $g \gg 1$ while our lattice model converges with the grid model (See Fig. 3.21(b)). This finding indicates that, the disagreement with the lattice

model by Zheligovskaya et al. might be due to the inaccuracy of their data.

3.6 Conclusions

Two definitions of the tube length were studied, the tube axis and the primitive path. Both definitions show their conformations are random walk for long enough chains. The probability distribution of the tube length concludes that there are deviations between the Gaussian approximation especially with respect to deep retractions of the tube in larger grid sizes. Furthermore, the potential is stronger than predicted by the tube theory.

Table 3.6: The product of a and b_{1D} from the tube axis and the primitive path.

grid	$(a^g \times b_{1D}^g)/b_{3D}$	$(a^{pp} \times b_{1D}^{pp})/b_{3D}$
1	2.127	2.481
2	4.021	4.008
4	7.991	7.527
8	16.299	13.976
16	33.789	
32	70.290	
64	142.453	

According to the definition of the tube, the contour length of the tube axis is longer than the primitive path and none of them give $b_{1D} = b_{3D}$. Despite the fact that parameters of the tube axis and the primitive path are not equal, the ab_{1D} is almost the same (see Table 3.6). It can be concluded that, any definition of the tube contour length results in similar ab_{1D} . The parameters examined in this chapter will be further applied to the analyses of the dynamics of entangled polymer chains.

Chapter 4

Dynamic Analysis of the Tube

4.1 Introduction

The dynamic properties of the entangled polymer chains that are examined in this chapter are MS displacement of the bead $g_{1,\text{mid}}(t)$, stress relaxation modulus, $G(t)$, end-to-end vector relaxation function, $\Phi(t)$, tube survival function, $\mu(t)$ and MS displacement of bead along the tube axis, $g_s(t)$. The objectives of the analysis are to validate the assumptions of the tube theory with regards to the agreement between $G(t)$, $\Phi(t)$ and $\mu(t)$ and the determination of the tube parameters, a , b_{1D} and ζ_{1D} . The $\mu(t)$ and $g_s(t)$ are obtained based on the tube length which are defined by the tube axis (see section 3.2.2).

4.2 Tube mapping

The dynamics of the chain is referred to as reptation where the middle bead moves simultaneously along the tube while the ends move randomly [11]. The tube cells are created when chain ends moved out into a new position and are deleted when the ends retract into the tube. Thus, each cell in the tube contains information

about its creation time and its life time. The life time is defined as time difference between the creation time and the time that the cell is visited again by the chain ends. This is required in calculating the $\mu(t)$ where it is defined as fraction of the tube segments that live longer and equal to time t .

At every time step, a new tube segment is created or deleted depending on the motion of the chain inside the tube. Thus the current tube is required to map with its configuration at a previous time step. This is to determine which segment of the tube is deleted, added and which segment moved into a new position. The process to gather these information is known as tube mapping.

Tube mapping is essential and proper validation is required to ensure $\mu(t)$ is correctly calculated. The mapping becomes more complicated because a tube cell can be occupied by more than one bead at one time. The algorithm of the mapping is described in Appendix B.

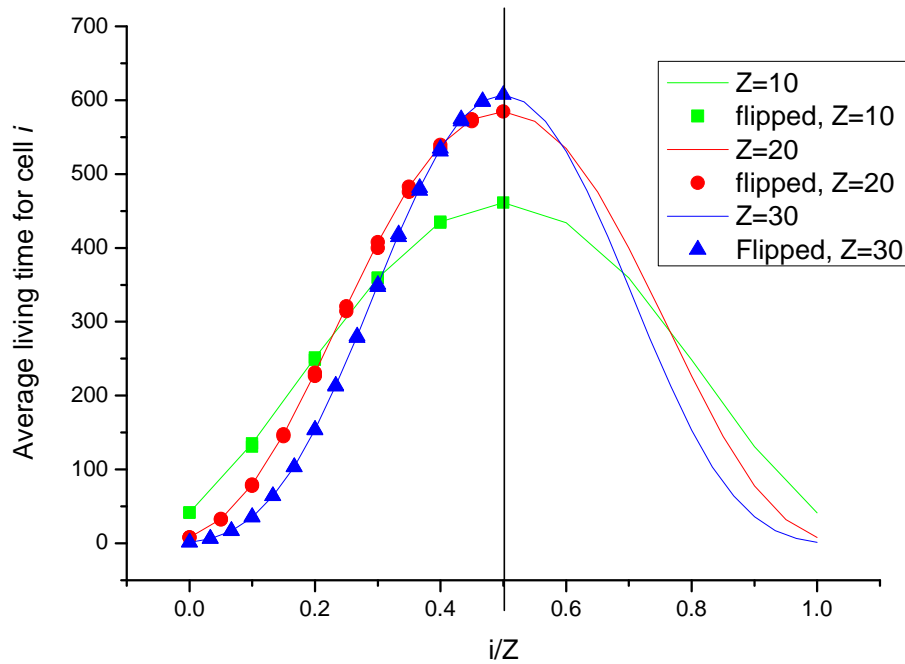


Figure 4.1: Living time of cells for $Z^s=10, 20$ and 30 , grid=1

The check is the distribution of the average living time of cells in the tube must

be symmetric. This quantity is predicted by the tube theory [9, Fig. 6.5]. Fig. 4.1, shows the distribution of the average living time of each cell in different tube lengths. The symmetric properties is checked by imposing the right side of the plot into its left side (symbols in Fig. 4.1). This figure confirms that our mapping algorithm provide the reasonable distribution of the average living time of cells inside the tube.

4.3 Tube segment occupation function

The function $\mu(t)$ is defined as the fraction of tube segments who live longer than time t . The expression for $\mu(t)$ for all length scales is available in section 1.10.3. The $\mu(t)$ for early time, $\tau_e < t < \tau_R$ has a scaling form [45]:

$$\mu(t) = \frac{L(t)}{L_0} \quad (4.1a)$$

$$= 1 - \frac{C_\mu}{\hat{Z}} \left(\frac{t}{\tau_e} \right)^{1/4} \quad (4.1b)$$

where C_μ is numerical prefactor, calculated to be $C_\mu \approx 1.5$ in [45].

In this project, $\mu(t)$ is calculated as presented in the following example (see Fig 4.2). At initial time, $t = 0$, the tube has 3 cells (2 segments). In here, we use $\Delta t = 1$ for simplicity. The data that is gathered at every time step is the cell's creation time, t_i^c , ($i = 0, \dots, Z^s$). The life time is the time the cell lives at time t which is defined as $t_i^l = t - t_i^c$, ($i = 0, \dots, Z^s$). At every time integration steps the $\mu(t)$ is calculated as follows:

1. At $t = 0$.

Firstly the creation time for each cell is assigned, $t_i^c = 0$, $i = 0, \dots, 2$. Then their living time is calculated as shown in Fig. 4.2(a).

2. At $t = 1$.

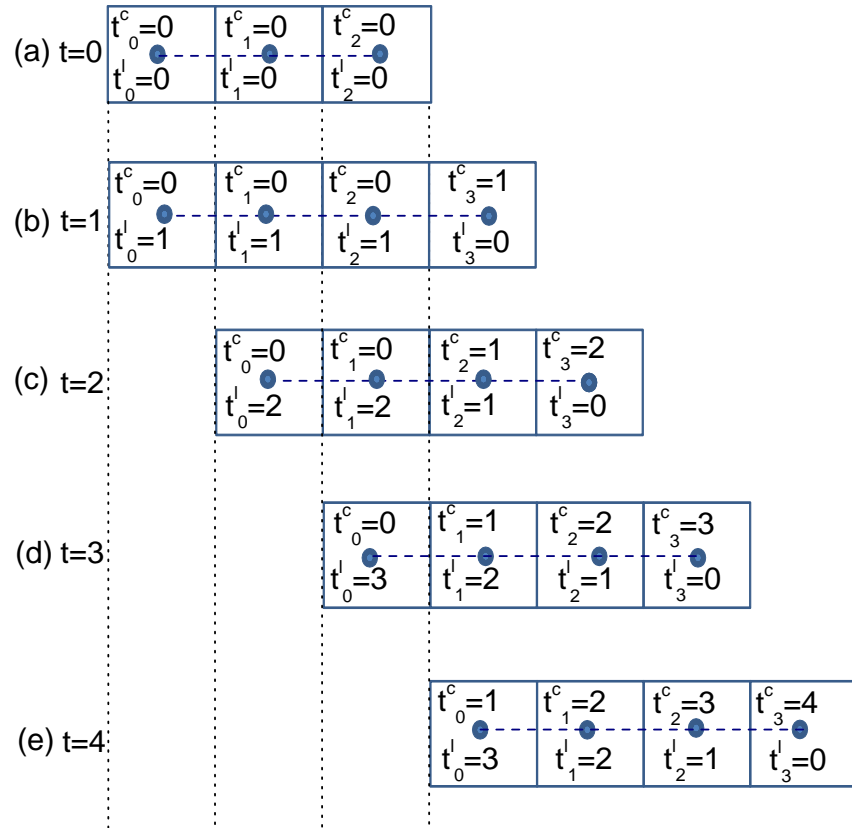


Figure 4.2: Steps in calculating $\mu(t)$ where t_i^c and t_i^l are the creation time and living time for cell i respectively.

Assume the chain retraction makes the tube expand into $Z^s = 4$ (see Fig. 4.2(b)). A new cell $i = 3$ is created and its creation time is $t_3^c = 1$. The creation time for cells 0 until 2 is transferred from $t = 0$ as shown in Fig. 4.2(b) with their $t_i^l = 1$, $i = 0 \cdots 2$. $\mu(t)$ for $t = 0$ is:

$$\mu(t = 0) = \frac{4}{4} = 1.0$$

$$\mu(t = 1) = \frac{3}{4} = 0.75$$

3. At $t = 2$.

The chain reptates on the right direction thus one cell is created and one cell

at the left of the tube is deleted. The creation time for the new cell is assigned, $t_3^c = 2$ and the living time for each cell is calculated as shown in Fig .4.2(c).

Thus $\mu(t)$ for this time is:

$$\mu(t = 0) = \frac{4}{4} = 1.0$$

$$\mu(t = 1) = \frac{3}{4} = 0.75$$

$$\mu(t = 2) = \frac{2}{4} = 0.5$$

4. At $t = 3$.

The chain reptate into one cell, a new cell, $i = 3$ is created and one cell in the left of the tube is deleted. The t_i^c and t_i^l with $i = 0, \dots, 2$ are shown in Fig. 4.2(d). The $\mu(t)$ for this time is :

$$\mu(t = 0) = \frac{4}{4} = 1.0$$

$$\mu(t = 1) = \frac{3}{4} = 0.75$$

$$\mu(t = 2) = \frac{2}{4} = 0.5$$

$$\mu(t = 3) = \frac{1}{4} = 0.25$$

5. At $t = 4$.

A new tube is created with the creation time and living time for each cells as

shown in Fig. 4.2(e). The $\mu(t)$ as follows:

$$\mu(t = 0) = \frac{4}{4} = 1.0$$

$$\mu(t = 1) = \frac{3}{4} = 0.75$$

$$\mu(t = 2) = \frac{2}{4} = 0.5$$

$$\mu(t = 3) = \frac{1}{4} = 0.25$$

$$\mu(t = 4) = \frac{0}{4} = 0$$

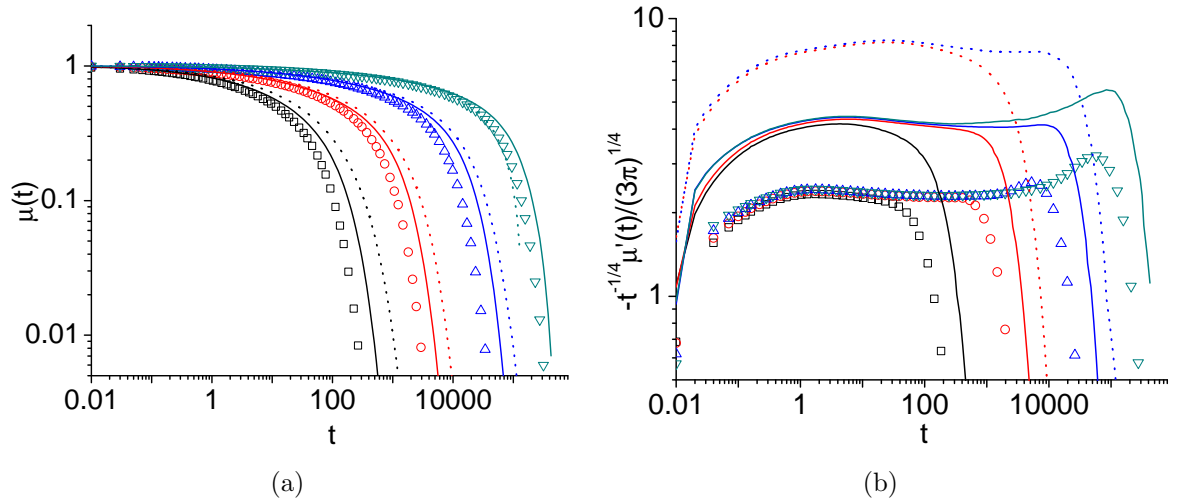


Figure 4.3: The $\mu(t)$ for $g' = 1$ with $N = 16, 32, 64, 128$ in symbols, whereas $g' = 2$ is shown in solid lines for $N = 32, 64, 128, 256$ and the dashed lines are for $g' = 4$ with $N = 64, 128, 256, 512$. Fig. 4.3(b) shows the normalised derivative of $\mu(t)$ for g' and N as in Fig. 4.3(a), while for $g' = 4$, the chain lengths are $N = 128$ and 256 .

The behaviour of $\mu(t)$ is boring monotonic and it is quite difficult to obtain much information regarding to the tube parameters from it. This is shown in Fig. 4.3(a) for $g' = 1, 2$ and 4 with various chain lengths. However the time derivative of Eq. 4.1b indicates:

$$\tilde{\mu}(t) \equiv -4\hat{Z}\tau_e^{1/4}t^{3/4} \left(\frac{\partial\mu}{\partial t} \right) \quad (4.2)$$

where a plateau region appears at early time $\tau_e \leq t \leq \tau_R$ which gives the value of unknown coefficient C_μ in Eq. 4.1b. At later time $\tau_R \leq t \leq \tau_d$ a step rise pattern is noticeable for the well entangled chains..

The tube theory predicts the plateau region is approximately at 1.5, however we obtain, the plateau at 2.3 for $g' = 1$ and increases with the grid size. This is due to the approximations have been made to the tube parameters above.

4.4 Bead diffusion along the tube axis

According to Doi and Edwards [9], the dynamics of the beads inside the tube at times $\tau_e < t < \tau_R$ is 1D Rouse-like diffusion along the tube axis and at $\tau_R < t < \tau_d$, the whole chain diffuses along the tube. This assumption can be validated by observing the mean square displacement of a bead along the tube axis, $g_s(t)$. The $g_s(t)$ is defined as $g_s(t) \equiv \langle \Delta s(t)^2 \rangle$ and $\Delta s(t) = s(t) - s(0)$ where s is bead position in the unit of the cell index, which is measured from the middle cell of the tube. The middle cell is chosen to avoid the tube ends effect and to reduce the probability of the bead coming back into the tube after an infinitely long time.

Assumes the $s(t)$ in a continuous function, thus the Langevin equation of the $s(t)$ can be referred in [9, Eq. 6.77]. The solution of the equation is [32]:

$$g_s(t) = \frac{2k_B T}{(N+1)\zeta_{1D}} t + \frac{b_{1D}^2}{3(N+1)} \sum_{p=2, \text{even}}^N \sin^{-2} \left(\frac{\pi p}{2(N+1)} \right) \left(1 - \exp \left(-\frac{t}{\tau_{p,1D}} \right) \right) \quad (4.3)$$

with $\tau_{p,1D} = \frac{\zeta_{1D} b_{1D}^2}{12k_B T} \sin^{-2} \left(\frac{\pi p}{2(N+1)} \right)$, $p = 1, \dots, N$ and $\tau_{R,1D} = \frac{b_{1D}^2 \zeta_{1D} N^2}{3\pi k_B T}$. In summary,

the $g_s(t)$ contain the two regimes:

$$g_s(t) \approx \begin{cases} \frac{2Nb_{1D}^2}{3\pi^{3/2}} \sqrt{\frac{t}{\tau_{R,1D}}}, & t \leq \tau_{R,1D} \\ \frac{2Nb_{1D}^2}{3\pi^2} \frac{t}{\tau_{R,1D}}, & t \geq \tau_{R,1D} \end{cases} \quad (4.4)$$

and the simpler empirical expression as follows:

$$g_s(t) = \frac{2Nb_{1D}^2}{3\pi^2} \sqrt{\frac{t}{\tau_{R,1D}}} \left(\pi^{3/2} + \left(\frac{t}{\tau_{R,1D}} \right)^{3/2} \right)^{1/3} \quad (4.5)$$

The $g_s(t)$ describes the one dimension motion of bead in the tube space. The motion of the real space is described in the following section.

4.4.1 Mean square displacement in real space

By assuming the $s(t)$ is a continuous function the probability distribution of $\Delta s(t)$ can be represented by Gaussian with zero mean:

$$P(\Delta s(t), g_s(t)) = \frac{1}{\sqrt{2\pi g_s(t)}} \exp\left(-\frac{\Delta s(t)^2}{2g_s(t)}\right) \quad (4.6)$$

The distribution of the separation between two beads in the real space r given their separation along the tube axis, Δs is

$$P(r, \Delta s) = \left(\frac{3}{2\pi|\Delta s|a} \right)^{3/2} 4\pi r^2 \exp\left(-\frac{3r^2}{2|\Delta s|a}\right) \quad (4.7)$$

where ' a ' is the tube Kuhn step.

The standard spherical symmetric Gaussian has $\langle r^2 \rangle = a\Delta s$. Thus, to obtain the mean square displacement in real space in this project, for the middle bead $g_{1,\text{mid}}(t)$,

we use:

$$g_{1,\text{mid}}(t) = \int_{-\infty}^{\infty} d\Delta s(t) P(\Delta s(t), g_s(t)) \int_0^{\infty} r^2 dr P(r, \Delta s) \quad (4.8)$$

The inner integral over r is $|\Delta s|a$ and the outer integral gives [72]:

$$g_{1,\text{mid}}(t) = 2a \int_0^{\infty} \Delta s d\Delta s P(\Delta s(t), g_s(t)) \quad (4.9)$$

$$= a \sqrt{\frac{2}{\pi} g_s(t)} \quad (4.10)$$

4.5 Results and discussions

4.5.1 Main results for the grid model

The main results for the different grid sizes and chain lengths for the grid model such as the mean square displacement of the middle bead, $g_{1,\text{mid}}(t)$, the end-to-end vector relaxation function, $\Phi(t)$ and the stress relaxation function, $G(t)$, are shown in Fig. 4.4. In this model, the CLF and the longitudinal relaxation due to redistribution of beads inside the tube are naturally included.

The $g_{1,\text{mid}}(t)$ shows three regimes as predicted by the tube theory, (see section 1.10.5). However, for the larger grid, there are negative slopes shown for the plot that are normalised by $t^{1/4}$ (see Fig. 4.4(a)). This shows that the bead moves slower than expected by the tube theory in which might be caused by the perpendicular motion of the bead inside the tube.

The $\Phi(t)$ shows that the terminal time, τ_d increases strongly with N for all grid sizes. The tube theory predicts that the τ_d scales with $N^3 - N^{3.4}$. Our analysis shows that τ_d increases faster than N^3 (see Fig. 4.5(b)) for all grid sizes.

The $G(t)$ consists of two stages of relaxation. The first stage occurs at $t \leq \tau_e$, where the $G(t)$ relaxes according to the unentangled Rouse chain $G(t) \sim t^{-1/2}$ and

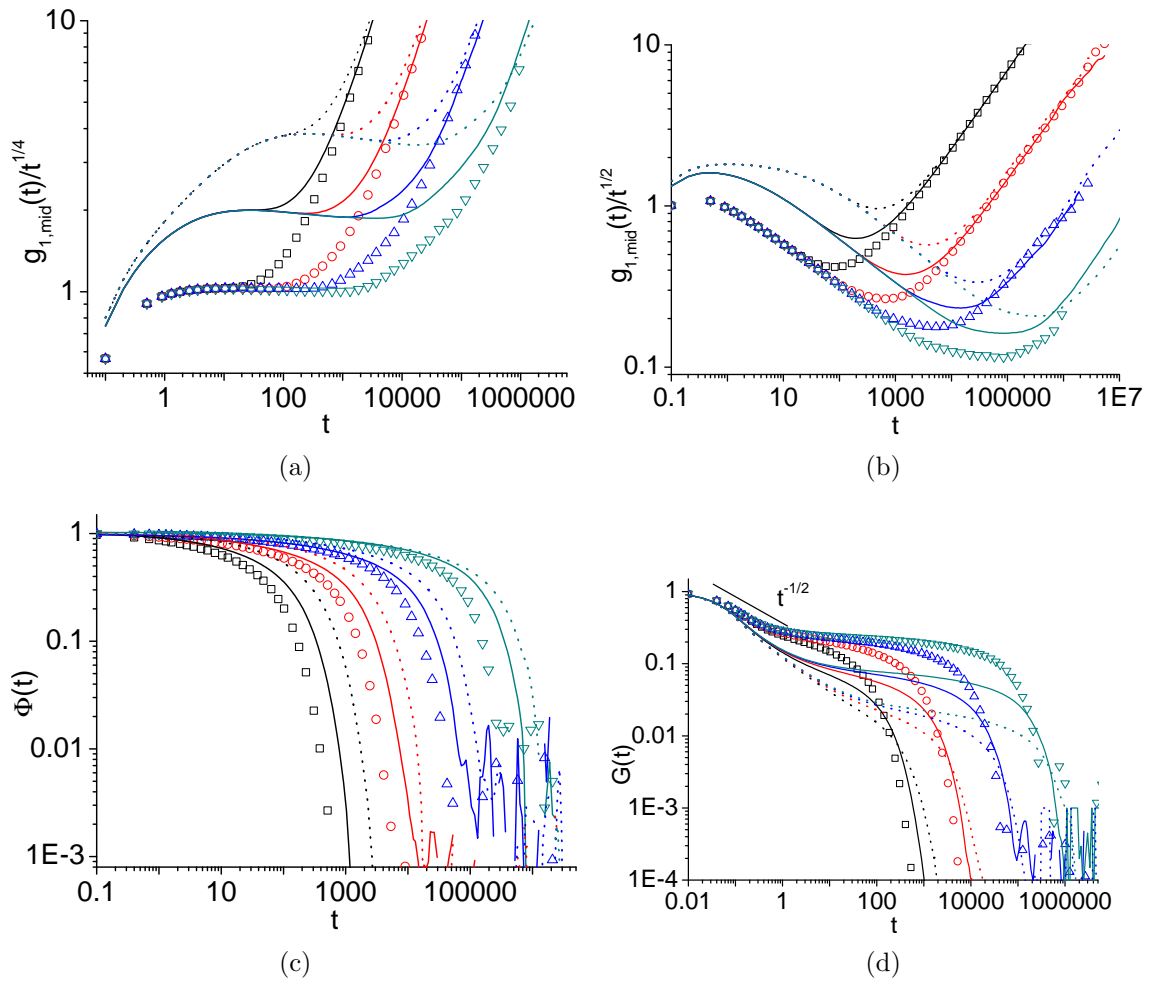


Figure 4.4: Main results for the grid model. Symbols correspond to $g = 1$ with $N = 16, 32, 64, 128$, lines for $g = 2$ with $N = 32, 64, 128, 256$ and the dotted lines for $g' = 4$ with $N = 64, 128, 256, 512$.

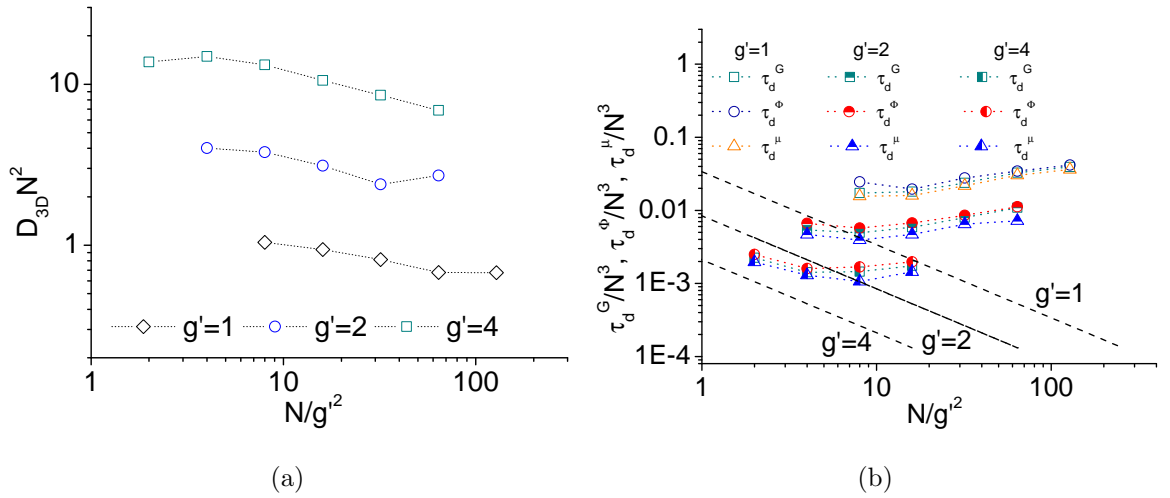


Figure 4.5: Diffusion coefficient in 3D space, D_{3D} normalised by N^2 as a function of N/g^2 for $g' = 1, 2$ and 4 in Fig. 4.5(a). The normalised disengagement time, τ_d by N^3 which is obtained from $G(t)$, $\Phi(t)$ and $\mu(t)$ for $g' = 1, 2, 4$ and the dashed lines are the Rouse time, τ_R for each grid size are shown in Fig. 4.5(b).

is independent of the chain lengths. The second regime occurs at $t \geq \tau_e$ which shows almost a plateau region especially for the longest chains. In comparison, the $G(t)$ in the tube model only has the second regime.

These results are quantitatively similar to the tube model, however at present there are no clear methods to obtain the tube parameters. An ideal analysis method would be a method which can be implemented into the other models and the results are model independent. In the following section, we attempt to obtain the tube parameters by using the dynamic properties of the tube.

4.5.2 The tube theory predictions

In the absence of CR, the tube theory predicts that $\Phi(t) = \mu(t)$ and $G(t) = G_0\mu(t)$ which will be examined in this section. The $\mu(t)$ and $\Phi(t)$ for all grid sizes are almost identical to each other (see Figs. 4.3(a) and 4.4(c)). However, the difference between them clearly appears in their derivative. The $\tilde{\mu}(t)$ (see Fig. 4.3(b)) shows

roughly a plateau region at an early time ($t < \tau_R$). On other hand, the normalised $\Phi'(t)$ by $-Nt^{3/4}$ shows a slow positive slope of 0.02 in all grid sizes (see Fig 4.6).

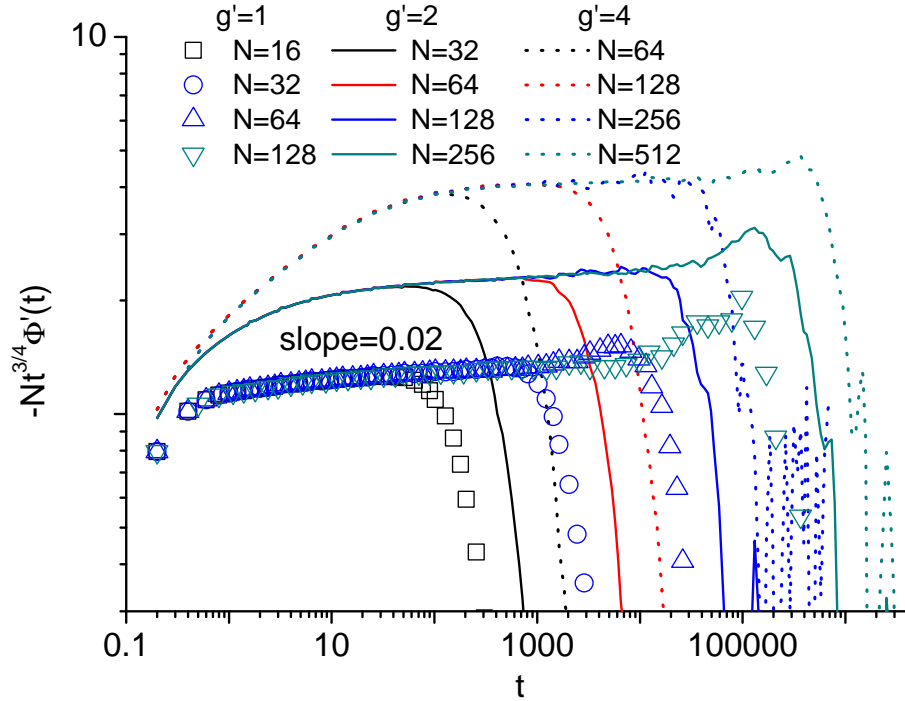


Figure 4.6: Normalised derivative of the end-to-end vector relaxation function, $-Nt^{3/4}\Phi'(t)$ for different g' and N .

The function of $G(t)$ for $g' = 2$ was shifted vertically until it agree with $\mu(t)$ and $\Phi(t)$, respectively, are shown in Fig. 4.7. The better agreement occurs, for the longer chain length but there is less agreement for the shorter chain.

The diffusion coefficient D_{3D} that normalised by N^2 is shown in Fig. 4.5(a). In each grid size, the D_{3D} almost scale with $1/N^2$ as predicted by the tube theory [9, Eq. 6.40]:

$$D_{3D} = \frac{k_B T a^2}{3N^2 \zeta_{3D} b_{3D}^2} \quad (4.11)$$

The distinct difference between $G(t)$, $\mu(t)$ and $\Phi(t)$ is obtained by comparing their relaxation time, τ_a which is shown in Fig. 4.5(b). The τ_a in Fig. 4.5(b) is obtained by fitting the results on $G(t)$, $\mu(t)$ and $\Phi(t)$ with the Maxwell modes by

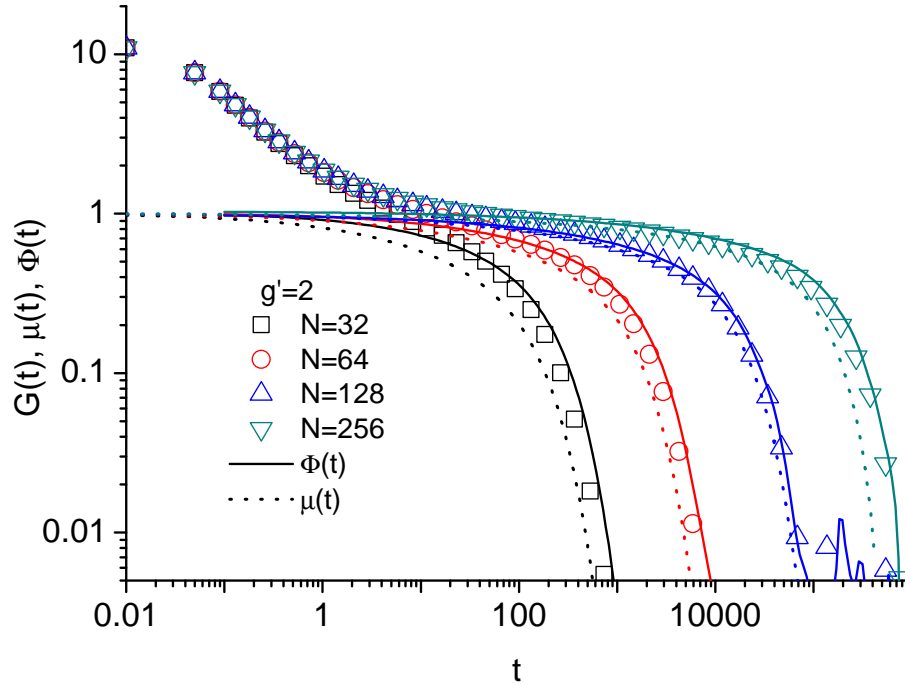


Figure 4.7: The vertically shifted $G(t)$ until they collapse upon $\mu(t)$ and $\Phi(t)$ for $g' = 2$ with $N = 32, 64, 128, 256$.

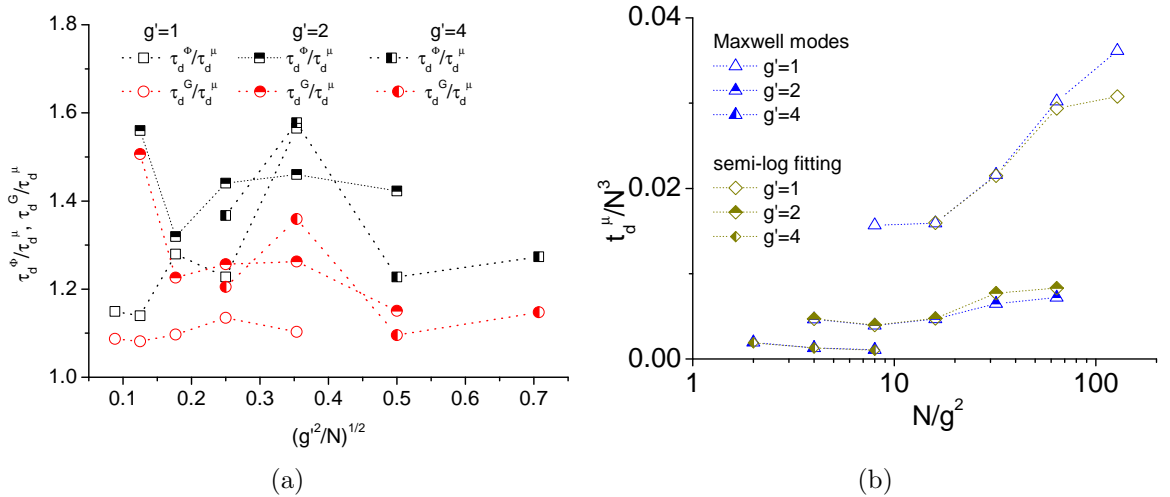


Figure 4.8: Ratio between τ_d from $\Phi(t)$ and $G(t)$ and τ_d from $\mu(t)$ in Fig. 4.8(a). The normalised disengagement time, τ_d by N^3 for $\mu(t)$ which are obtained by using the Maxwell modes and calculate the gradient of the semi-log plot in Fig. 4.8(b).

using Reptate software.

The other method to obtain τ_d is by fitting a semi-log plot at the late time region ($t \gg \tau_R$). The gradient of the fitting gives the inverse of τ_d . Fig 4.8(b) shows the τ_d from both methods for $\mu(t)$ which give approximately the same τ_d . As a result in the following analysis we use the first method (Maxwell modes) in obtaining the τ_d for $G(t)$, $\Phi(t)$ and $\mu(t)$.

The ratio of the relaxation time of $G(t)$ and $\Phi(t)$ with the $\mu(t)$ as a function to g^2/N is shown in Fig. 4.8(a). The sequence of the relaxation from the fastest to the slowest is $\mu(t)$, $G(t)$ and $\Phi(t)$, respectively.

4.5.3 Fitting with the tube theory

One of the methods to obtain the tube parameters is by fitting the simulation results with an adequate theory [45, 73]. Likhtman and McLeish updated the tube theory which we refer to as LM2002. The theory includes all length scales, counting CLF, CR and longitudinal modes as follows [45]:

$$G(t) = G_e \left(\frac{4}{5} \mu(t) R(t) + \frac{1}{5Z} \sum_{p=1}^{Z-1} \exp\left(-\frac{p^2 t}{\tau_R}\right) + \frac{1}{Z} \sum_{p=Z}^N \exp\left(-\frac{2p^2 t}{\tau_R}\right) \right) \quad (4.12)$$

Where $R(t) = 1$ for our case without CR. Details about Eq. 4.12 are available in [45, 70]. Fig. 4.9 shows the snapshot of the fitting for $g' = 2$ with $N = 32, 64, 128$ by using our in-house software, ‘Reptate’. The lines and squares are the theory and the simulation data, respectively. The parameters that are obtained in the fitting, N_e , τ_e and G_e are presented in Table 4.1.

In Fig. 4.9, the longer chain fits well with the theory. However, for the shorter chain and at high frequency, the fits are not really good. In addition, the N_e in Table 4.1 for all grid sizes are higher than the one obtained in the static analysis of

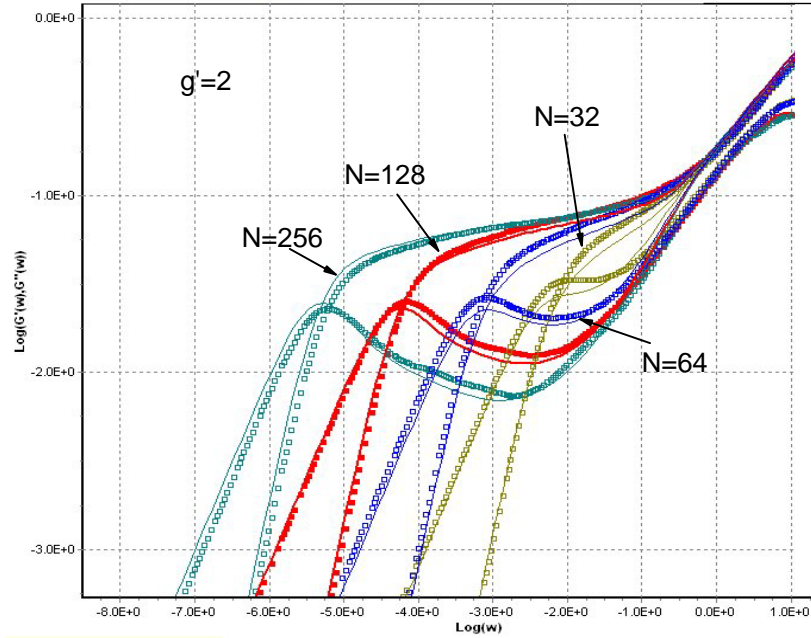


Figure 4.9: The $G'(\omega)$ and $G''(\omega)$ from the simulation results (symbols) and the tube theory, LM2002 (symbols) for $g' = 2$ with $N = 32, 64, 128, 256$.

Table 4.1: The tube parameters obtained from fitting the simulation results with the tube theory, LM2002.

g	Ne	τ_e	G_e
1	3	0.586	0.313
2	9	6.223	0.097
4	25	37.505	0.036
8	84	471.18	0.01

the tube, tube axis and primitive path (see Table 3.4). This disagreement indicates that the theory can't represent our model. In the next section, we study the effects which might contribute to the disagreement with the theory.

4.5.4 Bead diffusion inside the tube

The tube theory assumes that the bead inside the tube moves in 1D motion with the $g_s(t)$ scales with $t^{1/2}$ at $t \leq \tau_R$ and $g_s(t) \sim t$ at $t \geq \tau_R$. This is shown in Fig. 4.10(a) for $g' = 1, 2$ and 4 with various chain lengths. The first regime clearly shows at the longest chain lengths. The negative slope at an earlier time for $g' = 2$ and $g' = 4$ occurs because of the discretisation effects where the $g_s(t)$ is measured by the integer of the cell index. The other contribution might be the unentangled loops where the bead is stationary if the reference bead is in the unentangled loops.

To study the discreteness effects which occur at early time for $g_s(t)$ as shown in Fig. 4.10(a), we observe the mean square displacement of the middle bead in free space (Rouse model) using the discrete coordinate of the beads, rounded to the nearest integer. This is shown in Fig. 4.10(b) for $N = 16, 64$ and 256 where their negative slopes at early time $t \leq \tau_R$ are similar with the $g_s(t)/t^{1/2}$.

Fig. 4.11 shows the time normalised by τ_R in 3D for each chain length. The scaling of $\tau_R \propto N^2$ is shown in Fig. 4.5(b). The plots collapse onto each other at $t > \tau_R$ and the transition between the $g_s(t) \propto t^{1/2}$ and $g_s(t) \propto t$ regimes occur at a time later than τ_R . This gives the first sight that the $\tau_{R,1D}$ is greater than the Rouse time in 3D.

The simulation results for $g_s(t)$ are fitted with Eq. 4.5 to obtain the parameters, b_{1D} and ζ_{1D} . Having the b_{1D} and ζ_{1D} , we are able to predict the $g_{1,\text{mid}}(t)$ by using Eqs. 4.3 and 4.10, which is shown by the dotted lines in Fig. 4.12 for $g' = 1$ and $g' = 2$ with various chain lengths. The prediction fit very well with the simulation results

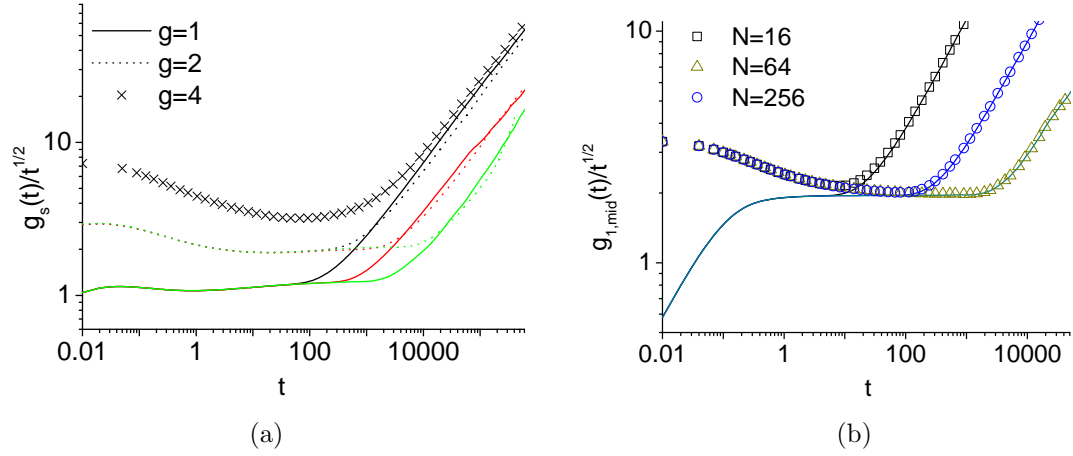


Figure 4.10: The normalised $g_s(t)$ by $t^{1/2}$ for $g' = 1$ with $N = 32, 64, 128$ are presented in solid lines, whereas the dashed lines for $g = 2$ with $N = 64, 128, 256$ and symbols for $g' = 4$ with $N = 128$ are shown in Fig. 4.10(a). The $g_{1,\text{mid}}(t)$ are based on the continuous (lines) and discrete (symbols) coordinate of the beads for $N = 16, 64$ and 256 for free Rouse chain is shown in Fig.4.10(b).

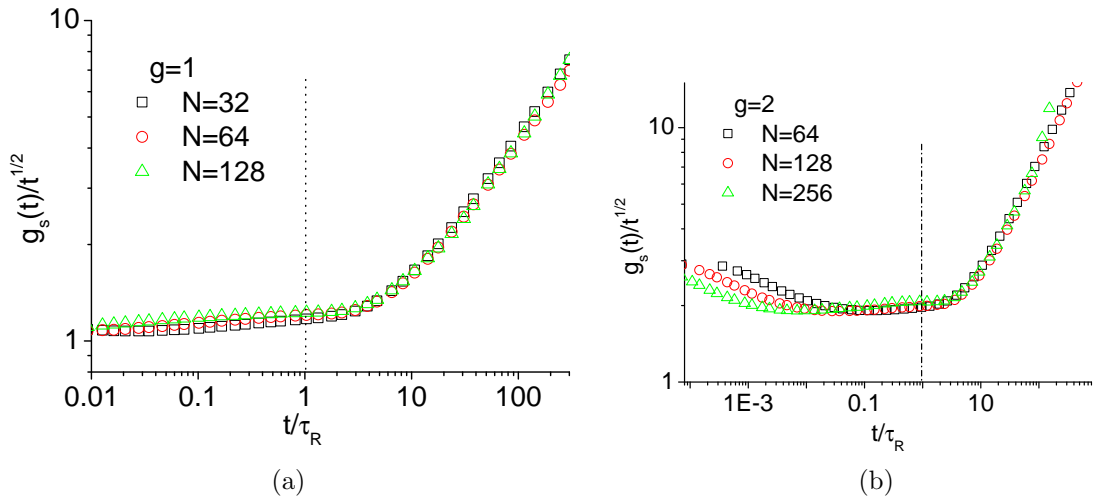


Figure 4.11: The time normalised by τ_R for $g' = 1$ and 2 are shown in Figs 4.11(a) and 4.11(b), respectively. The chain lengths are the same as shown in Fig. 4.10(a).

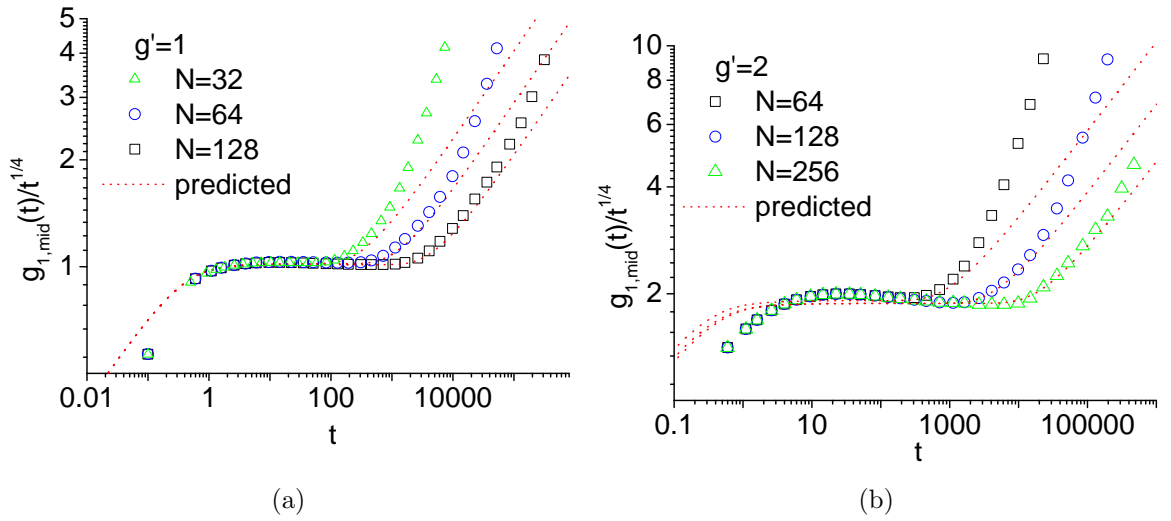


Figure 4.12: The normalised $g_{1,\text{mid}}(t)$ by $t^{1/4}$ from the simulation results (symbols) and predicted by Eq. 4.10 (dashed lines) for $g' = 1$ and $g' = 2$.

at $t \geq \tau_d$. In that plot, we use the parameter ‘ a ’ which was obtained from the static tube axis analysis. On the other hand, the tube Kuhn step, ‘ a ’ can be obtained by the following method. The procedure is plotting the $g_{1,\text{mid}}(t)$ and $\sqrt{(2/\pi)g_s(t)}$ and then $\sqrt{(2/\pi)g_s(t)}$ is vertically shifted until it collapses onto the $g_{1,\text{mid}}(t)$ (see Fig. 4.13(b) and 4.13(d) for $g' = 1$ and $g' = 2$, respectively). The agreement between them occurs at region $t \geq \tau_R$. The amount of the vertical shift gives the value ‘ a ’. The results from this analysis ‘ a ’ is compared with the static analysis (section 3.4.3). The comparison is shown in Fig. 4.14 for $g' = 1$ and $g' = 2$. The plot shows the value of ‘ a ’ are equal to each other with approximately less than 10% difference and nearly coincident for large N .

The drawback of $g_s(t)$ is that it requires the simulation to construct a tube-like region and do the tube mapping at every simulation step. These processes consume a lot of computational time, thus much more time is required to obtain better statistics especially for the longer chains. This is the reason why we have only managed to do the analysis of $g_s(t)$ up to $g' = 2$.

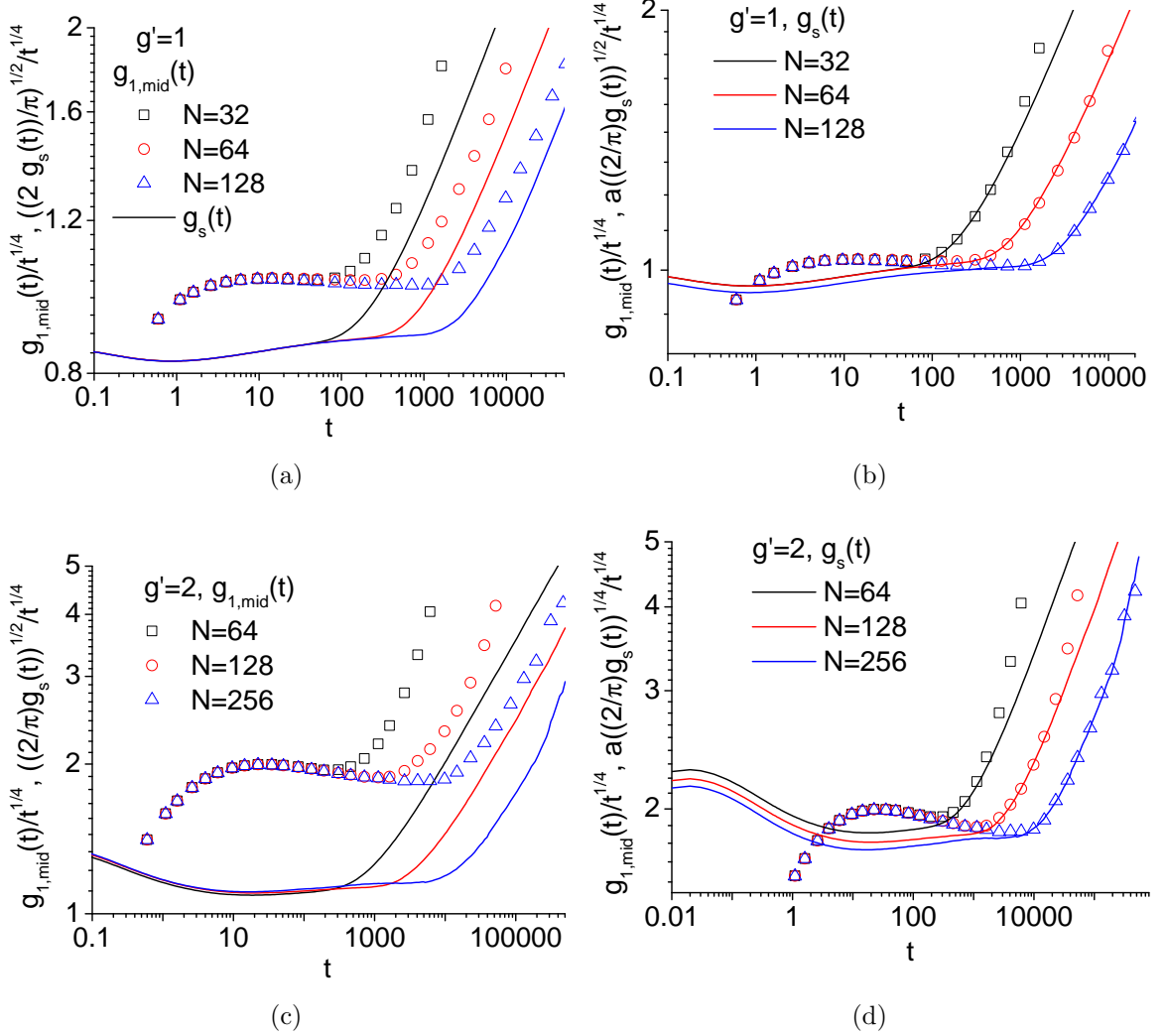


Figure 4.13: The $g_{1,\text{mid}}(t)$ and $\sqrt{2/\pi g_s(t)}$ for $g' = 1$ and $g' = 2$ are shown in Figs. 4.13(a) and 4.13(c). The vertical shifted of the $a\sqrt{2/\pi g_s(t)}$ in both grid sizes are shown in Figs. 4.13(b) and 4.13(d).

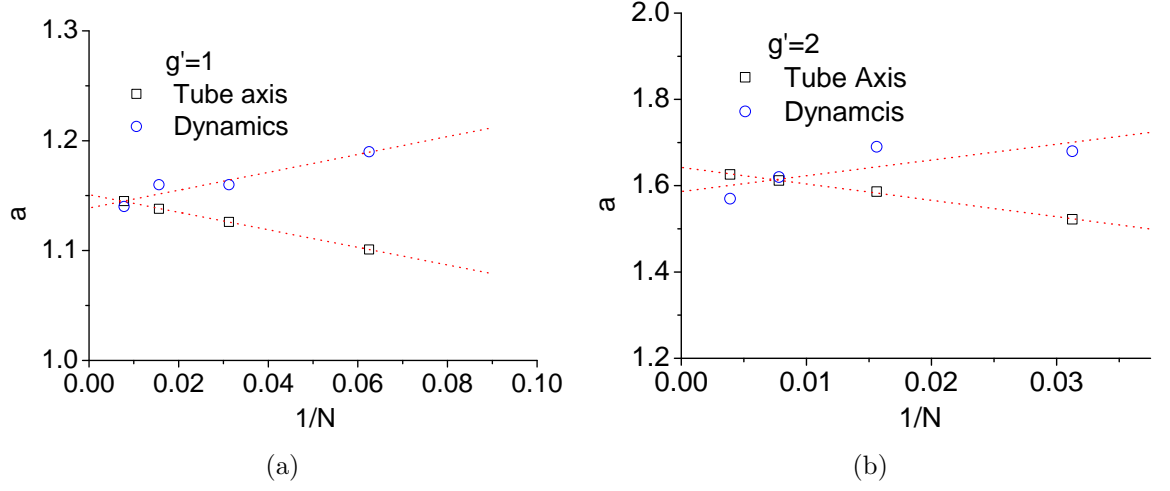


Figure 4.14: The tube Kuhn step, a which obtained from the tube axis and dynamics fitting (as in Fig. 4.13) for $g' = 1$ and 2.

Since the $g_{1,\text{mid}}(t)$ agrees very well with $g_s(t)$ as shown in Fig. 4.13, thus we can use $g_{1,\text{mid}}(t)$ to obtain the tube parameters. The expression for $g_{1,\text{mid}}(t)$ in Eq. 4.13 is obtained by substituting Eq. 4.3 into Eq. 4.10.

$$g_{1,\text{mid}}(t) = ab_{1\text{D}} \left(\frac{3\pi^2 t}{b_{1\text{D}}^2 \zeta_{1\text{D}}} \right)^{1/4} \sqrt{\frac{4}{3\pi^3}} \left(\left(\frac{3\pi^2 t}{N^2 b_{1\text{D}}^2 \zeta_{1\text{D}}} \right)^{3/2} + \pi^{3/2} \right)^{1/6} \quad (4.13)$$

Fitting the simulation data with Eq. 4.13, we obtain two combinations of the tube parameters, $ab_{1\text{D}}$ and $b_{1\text{D}}^2 \zeta_{1\text{D}}$. The $ab_{1\text{D}}$ from the static analysis (tube axis and primitive path) and this analysis (dynamics) are plotted as a function of $1/N$ as shown in Fig. 4.15. In the limit of $N \rightarrow \infty$, the $ab_{1\text{D}}$ in each method agrees with each other within about 10% difference. The difference is attributed to the accuracy of the fitting and the use of fewer data points in obtaining the extrapolated values.

In obtaining $\zeta_{1\text{D}}$, we require to use ' a ' and ' $b_{1\text{D}}$ ' either from the tube axis or primitive path. Fig 4.16(a) shows the $\zeta_{1\text{D}}$ derived from the parameters in the static analysis. $\zeta_{1\text{D}}$ from the primitive path is higher than the tube axis in all grid sizes.

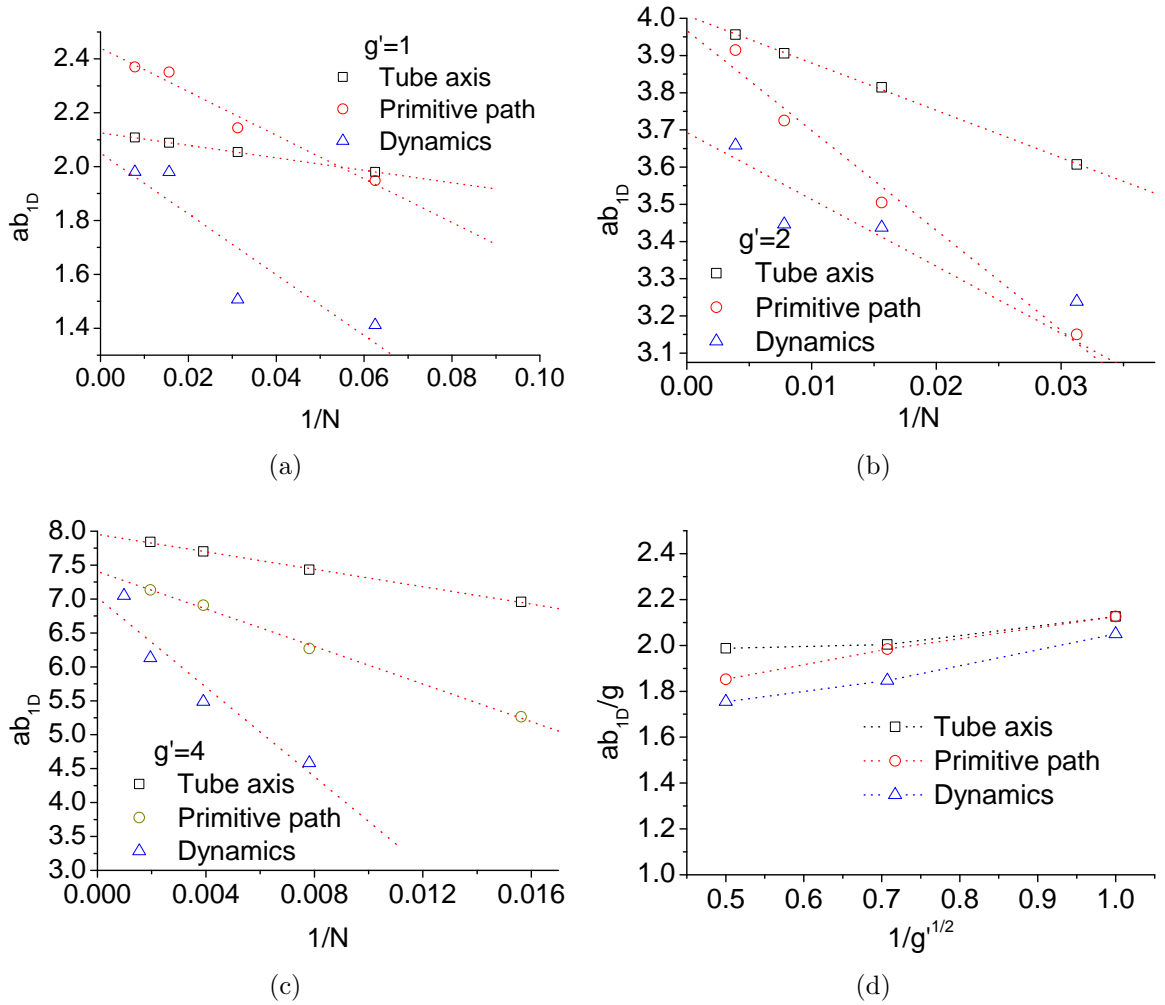


Figure 4.15: ab_{1D} obtained from the tube axis, primitive path and dynamics fitting for $g' = 1, 2$ and 4 . The extrapolated ab_{1D} from Figs. (a), (b) and (c) as a function of g' are shown in Fig. 4.15(d).

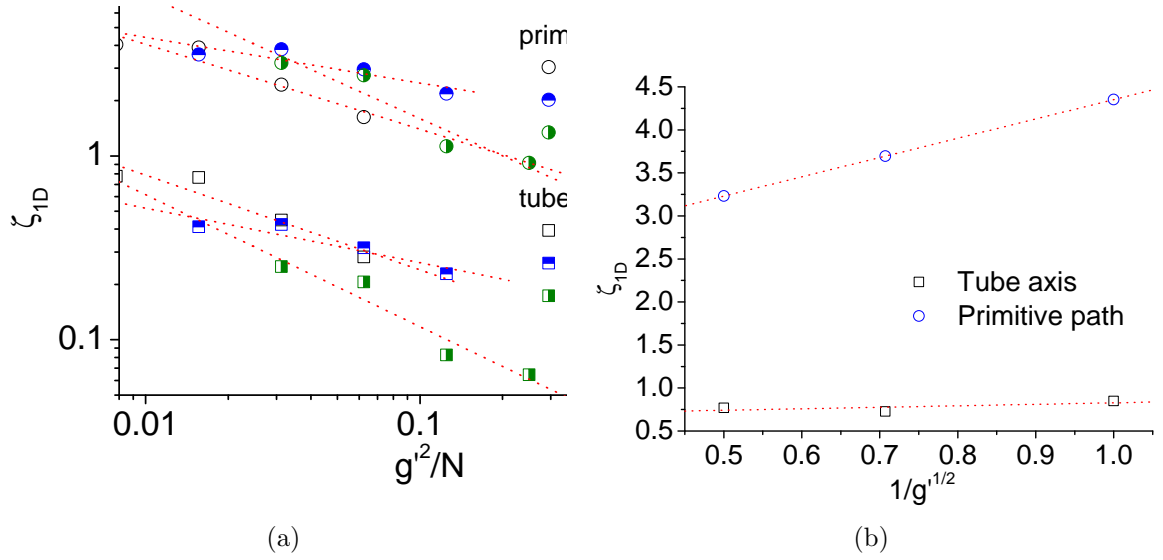


Figure 4.16: ζ_{1D} for $g' = 1, 2$ and 4 as a function of $(g')^2/N$ (Fig. 4.16(a)) and the extrapolated ζ_{1D} for each grid size is shown in Fig. 4.16(b).

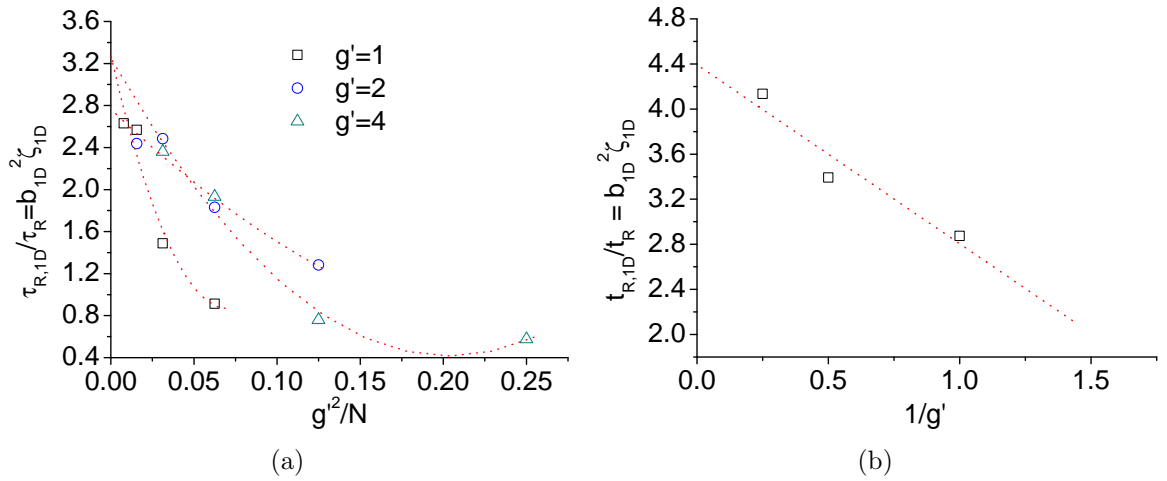


Figure 4.17: The ratio between the $\tau_{R,1D}$ from the tube axis and τ_R for each grid size as a function of $(g')^2/N$ is shown in Fig. 4.17(a). The extrapolated value of the ratio is presented in Fig. 4.17(b)

This is as expected because the contour length of the primitive path is shorter than the tube axis. The extrapolated ζ_{1D} is shown in Fig. 4.16(b) where it approaches 0.5 for the tube axis and 4.4 for the primitive path.

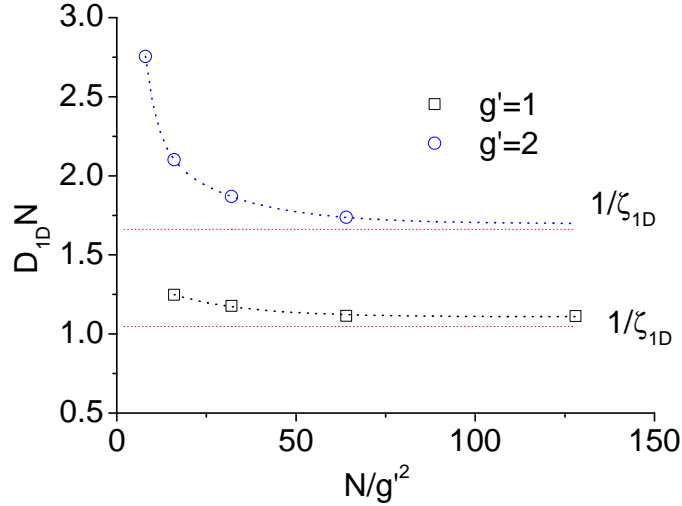


Figure 4.18: Diffusion coefficient of the 1D Rouse motion normalised by the chain length, N as a function of N/g'^2 . The dotted lines are the $1/\zeta_{1D}$ from the tube axis

Diffusion coefficient of the one dimensional Rouse chain $D_{1D} = \frac{k_B T}{N \zeta_{1D}}$ is observed in this simulation as shown in Fig. 4.18. The plots consist of $D_{1D}N$ which is proportional to $1/\zeta_{1D}$ where ζ_{1D} is obtained by using a^g from the tube axis and b_{1D} from fitting the results with $g_{1,\text{mid}}(t)$ (see Table 4.2).

The product between b_{1D} and ζ_{1D} gives the ratio between the τ_R and the $\tau_{R,1D}$ which is shown in Fig. 4.17 for the tube axis. We found that in all chain length and grid sizes, $\tau_{R,1D} > \tau_R$. The $\tau_{R,1D}$ for the limit of $N \rightarrow \infty$ shows it increases with the grid size and approach approximately 4.4 for $g \rightarrow \infty$.

4.6 Comparison with the tube simulation model

In this section, we compare our results with the tube simulation model. The comparison is conducted by using the simulation results from the tube and the grid

model. The tube simulation model is developed by using one-dimensional Rouse chain simulation which is projected into a three-dimensional freely-jointed random walk which represent the tube. The segments are independent of each other and the static properties of the model obey the Gaussian chain. The chain inside the tube moves in 1D motions with the end beads experience a hypothetical tensile force, $F_{eq} = \frac{3k_B T}{a}$ where a is the tube Kuhn segment. The motion is projected into 3D wheres the tube segments are deleted at the end when the bead does not occupy anymore. The segment are created when the chain sticks out of the tube. The observations are based on the 3D motion of the chain such as $g_{1,\text{mid}}(t)$, $G(t)$, $\Phi(t)$ and $\mu(t)$. The input parameters to the tube simulation model are N_e , a , b_{1D} and ζ_{1D} .

There are two sets of parameters; a , b_{1D} and ζ_{1D} that can be obtained from both the tube axis analysis and the primitive path analysis (see Table 4.2). The extrapolated values of the parameters ($N \rightarrow \infty$) are used as input into the tube model. We found that the set of parameters from the primitive path analysis produces the simulation results which are in better agreement with grid model if one includes stress relaxation function. Fig. 4.19 shows the main results for both simulations with the chain lengths of $N = 64, 128, 256$ where the parameters for the tube simulation model are $a = 4.812$, $b_{1D} = 0.833$ and $\zeta_{1D} = 3.964$. These parameters are based on the grid model with $g = 2$.

In $G(t)$, both models almost agree with each other after $\tau_e \approx 20$ (see Fig. 4.19(c)). The deviation at an earlier time is expected because their dynamics are different where at initial time, the beads in the tube simulation model are located along the tube segment and the beads motion are inside the tube. However, the disagreement in the normalised derivatives $\Phi(t)$ goes beyond τ_e which is approximately $t = 10^3$ (see Fig. 4.19(b)). The $g_{1,\text{mid}}(t)/t^{1/2}$ shows the tube model has a

slow transition between the first ($t \leq \tau_e$) and the third regimes ($t \geq \tau_{R,1D}$).

Generally, most of the plots are in good agreement with the grid model. The deviations are within the accuracy of the data (tube static analysis) and the fitting procedure. This analysis shows that determination of a , b_{1D} and ζ_{1D} is essential to predict the dynamics of the entangled polymer chains.

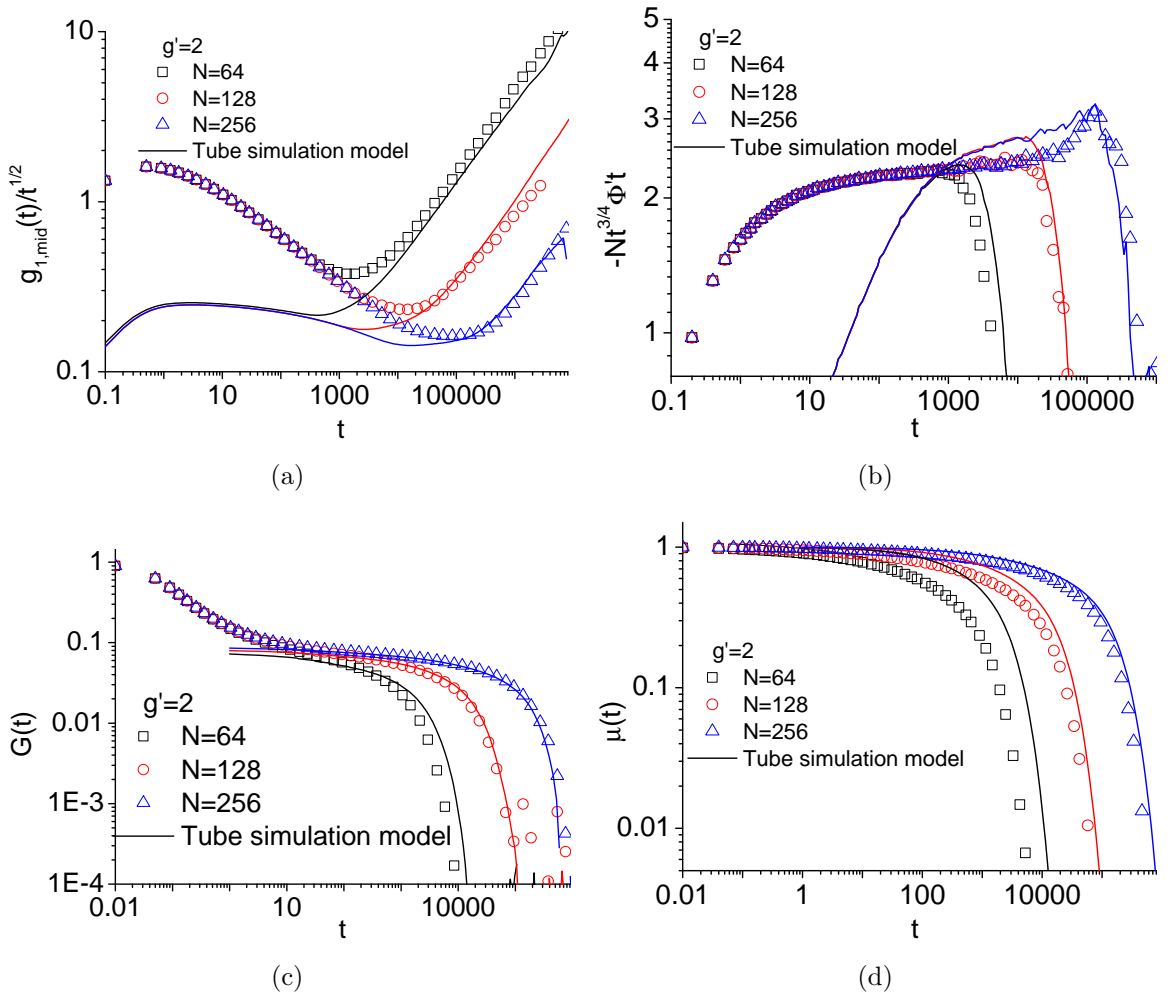


Figure 4.19: The comparison between the grid model (symbols) for $g' = 2$ with $N = 64, 128, 256$ and 512 and the tube simulation model (solid lines) where the input parameters are $a = 4.812$, $b_{1D} = 0.833$, $\zeta_{1D} = 3.964$.

4.7 Conclusions

The main results for the entangled polymer dynamics such as the properties of $G(t)$, $\Phi(t)$ and $g_{1,\text{mid}}(t)$ are compared to the tube theory. We found that $\mu(t) \neq \Phi(t)$ and $G(t) \neq G_0\mu(t)$. The mean square of the middle bead diffusion along the tube axis, $g_s(t)$ is observed and the pre-factor in Eq. 4.10 which gives the $g_{1,\text{mid}}(t)$ inside the tube is obtained. Fitting the simulation results with $g_{1,\text{mid}}(t)$ gives the parameters ab_{1D} and $b_{1D}^2\zeta_{1D}$. This shows that the combination of these two parameters contributes to the dynamics of the chain inside the tube. Table 4.2 presents the tube parameters which are obtained from $g_s(t)$ and $g_{1,\text{mid}}(t)$. In $g_{1,\text{mid}}(t)$ these parameters are calculated by using either a or a and b_{1D} from the static analysis as in Table 4.3.

Table 4.2: Extrapolated values of the tube parameters from the $g_s(t)$ and $g_{1,\text{mid}}(t)$

grid	$g_s(t)$		$g_{1,\text{mid}}(t)$					
	b_{1D}	ζ_{1D}	ab_{1D}	$b_{1D}^2\zeta_{1D}$	b_{1D}	ζ_{1D}	Tube Axis	Primitive path
							ζ_{1D}	ζ_{1D}
1	1.795	0.931	2.05	2.874	1.786	0.955	0.848	4.352
2	2.184	0.577	3.503	3.392	2.100	0.602	0.452	3.964
4			7.021	4.135	1.994	0.250	0.249	3.230

Table 4.3: Extrapolated values of the tube parameters from the static analysis

grid	Tube axis		Primitive path	
	a^g	b_{1D}^g	a^{PP}	b_{1D}^{PP}
1	1.151	1.848	2.997	0.828
2	1.646	2.433	4.812	0.833
4	2.586	3.09	8.702	0.846

Chapter 5

Conclusions

5.1 Conclusions

In this thesis we reported computer simulation of entangled polymer melts. The most successful model to represent the polymer melt is the tube theory. However the microscopic foundations of the tube are lacking in this theory and involved some assumptions which are investigated in this study. The simulation is developed for the Rouse chain in an array of obstacles which is based on the Brownian dynamics model with the implementation of the predictor-corrector algorithm. For the entanglement effects, the optimised uncrossability constraint is implemented to prevent the chain from violating the constraints. The CLF and longitudinal relaxation due to redistribution of segments inside the tube are naturally present. Standard parameters that are used; $\Delta t = 0.01$, $k_B T = 1$, $b_{1D} = 1$ and $\zeta_{3D} = 1$. The analysis of results was divided into two sections.

5.1.1 Static analysis of the tube

One of the static properties of the tube that we studied is the probability distribution of the tube length. The probability distribution shows that potential force acts on the chain ends is stronger than the potential predicted by the tube theory. The other property is the definitions of the tube length which are the tube axis a^g , b_{1D}^g and the primitive path a^{pp} , b_{1D}^{pp} . The tube length probability distribution is characterised by two parameters: tube Kuhn length (a), and the chain statistical segment length (b_{1D}) inside the tube. The results show that $a^g < a^{pp}$, $b_{1D}^g > b_{1D}^{pp}$ and in both definitions, $b_{1D} \neq b_{3D}$. However, the product of a and b_{1D} (ab_{1D}) produces almost the same value in both methods. The parameters a and b_{1D} from the tube axis are in good agreement with those in the lattice model in the limit of large grid size.

5.1.2 Dynamics analysis

In this analysis, we are interested to study the assumptions of the tube theory ($\zeta_{1D} = \zeta_{3D}$) and contributions of parameters a , b_{1D} towards the polymer chain dynamics. The main observations of the grid model are on $G(t)$, $g_{1,\text{mid}}(t)$, $\Phi(t)$ and $\mu(t)$, show quantitatively similar behavior to the tube theory. However, we found that the end-to-end relaxation function and the stress relaxation function are not equal with the tube segment occupation function, $\Phi(t) \neq \mu(t)$ and $G(t) \neq G_0\mu(t)$. The sequence of the relaxation from the fastest to the slowest is $\mu(t)$, $G(t)$ and $\Phi(t)$, respectively. In obtaining the tube parameters, we investigated the 1D bead diffusion along the tube axis, $g_s(t)$. From this observable we obtained tube Kuhn step as the pre-factor to map the $g_s(t)$ into real space $g_{1,\text{mid}}(t)$. Fitting the simulation results with the $g_{1,\text{mid}}(t)$, we obtained ab_{1D} and $b_{1D}^2\zeta_{1D}$. The analysis found that, ab_{1D} from this analysis is almost the same as those from the tube axis and the primitive path analysis. In obtaining the ζ_{1D} , we required a and b_{1D} from the tube

axis or primitive path analysis. To determine this, we compare our results with the tube simulation model. We found that the parameters from the primitive path is able to give a better agreement with the grid model in terms of their $G(t)$, $g_{1,\text{mid}}(t)$, $\Phi(t)$ and $\mu(t)$.

The drawback of the grid model is that it is not suitable for investigation of the non-linear experiments, where the large deformation or continuous shear deformations in 3D will result in the chains to align along the cubic lattice.

5.2 Future directions

5.2.1 Other architectures of polymer

This project can be extended further to study other branched architectures of polymer chains such as star, ring and comb. For example, the star polymer can be studied by using the grid model where one of the chain end is fixed in space. The dynamic properties of branched polymers can be observed similarly as in the linear chain.

5.2.2 Definition of $\mu(t)$

It is interesting to study different definitions of $\mu(t)$, for example to assume that the tube segment is relaxed when it moved out from its original tube which is implemented in [43]. Another definition will be to implement different weight factors for the tube segments, especially for the end segments.

5.2.3 Effects of CR

In this model, the CR was not introduced and we kept fixed position of the obstacles. However the obstacle can randomly appear and disappear to mimic other chains thus

representing the CR [41].

Appendix A

Monte Carlo simulation

A.1 Monte Carlo algorithm

The Monte Carlo simulation has been used widely in various types of polymer simulations [52, 74, 75]. The simulation implements an algorithm that consists of two independent steps. First, a trial move from state o to n is performed. The transition matrix that determines the probability to perform a trial move from an old position, \mathbf{R}_o to its new position, \mathbf{R}_n is denoted by $\alpha(\mathbf{R}_o \rightarrow \mathbf{R}_n)$. The α is referred to as the underlying matrix of a Markov chain [50]. The next step is the decision either to accept or reject the trial. The decision is made by using the Metropolis method. The method generates a random number, x , then the trial move is accepted if $x < \text{acc}(o \rightarrow n)$ and rejected otherwise [76]. The $\text{acc}(o \rightarrow n)$ is a matrix of the probability for accepting the trial moves. It is defined as [50]:

$$\text{acc}(o \rightarrow n) = \begin{cases} \exp[-\beta(U_{n,i} - U_{o,i})], & \text{for } U_{n,i} > U_{o,i} \\ 1, & \text{for } U_{n,i} \leq U_{o,i} \end{cases} \quad (\text{A.1})$$

with $U_{n,i}$ is the internal energy of the system when bead i is at position $\mathbf{R}_{n,i}$ and $\beta = 1/(k_B T)$.

A.1.1 Implementation of the Monte Carlo model

The implementation of the Monte Carlo model into our computer simulation is as follows [50, 77], for each ‘time’ step:

1. A bead is randomly selected from the total number of beads in the system. Each time step, not necessary all beads should be selected to move, the selection is based on a uniform distribution.
2. The selected bead, bead i which in position $\mathbf{R}_{o,i}$ with internal energy $U_{o,i}$ is then randomly moved into a new position, $\mathbf{R}_{n,i}$ by [53]:

$$\mathbf{R}_{n,i} = \mathbf{R}_{o,i} + \Gamma_i \tag{A.2}$$

where the properties of Γ_i are similar with one in Eq. 2.2. The position $\mathbf{R}_{n,i}$, has an internal energy of $U_{n,i}$

3. The total difference of its energy $\Delta U = U_{n,i} - U_{o,i}$ is calculated.
4. If $\Delta U \leq 0$, then the move is accepted and we move to step 7.
5. If $\Delta U \geq 0$, then generates a uniform distribution random number, x in the range $[0, 1]$. If $x < \exp(-\Delta U/k_B T)$ then go to step 6, otherwise the bead remains at it initial position $\mathbf{R}_{o,i}$.
6. The accepted bead $\mathbf{R}_{n,i}$ is checked whether it violates the obstacles by using the uncrossability constraints as in section 2.3. If the bead violated the constraint, then the motion is rejected.

7. The whole process is repeated N times.

A.1.2 Monte Carlo step

In the Monte Carlo simulation, the static properties are independent on the effective ‘time step’ determined by the maximum displacement of beads. Monte Carlo step does not reattempt the movement if any constraints are violated. In other words, the bead only moves into a new position if the movement was accepted by the Monte Carlo step and did not violate the uncrossability constraints.

The dynamics properties in a Monte Carlo simulation do depend on the effective time step. The chain moves slower with increasing maximum displacement of a bead where the movement has high rejection rate. This makes the data for Monte Carlo different from the Brownian dynamics simulation.

In this section, we are interested in obtaining the most effective time step for our Monte Carlo simulation. The procedure is by running the same simulations with $N = 32$, $g' = 1$ and various sizes of Δt . We begin with $\Delta t = 0.01$ and increase it by 0.025 which gives $\Delta t = 0.025, 0.05, 0.075, 0.1$ and 0.2 . For comparison, the similar configuration of simulation is used for the Brownian dynamics simulation with $\Delta t = 0.01$. The results are shown in Figs. A.1, A.3 and A.4 for $G(t)$, $g_{1,\text{mid}}(t)$ and $\Phi(t)$, respectively. The observation of $G(t)$ at $t = 32$ is shown in Fig. A.2(a) and for $g_{1,\text{mid}}(t)$ and $\Phi(t)$ are in the insets of Figs. A.3 and A.4, respectively. At small Δt , mostly all the dynamics observations show the Brownian dynamics and Monte Carlo are approximately equal to each other. This is because in both simulations, the beads do not reattempt its motion if constraint was violated. The dynamics observations from the Monte Carlo simulation show that increasing the Δt results in higher rejection rate, thus slower dynamics.

There is an optimal Δt that balances between the slowing down of the chain

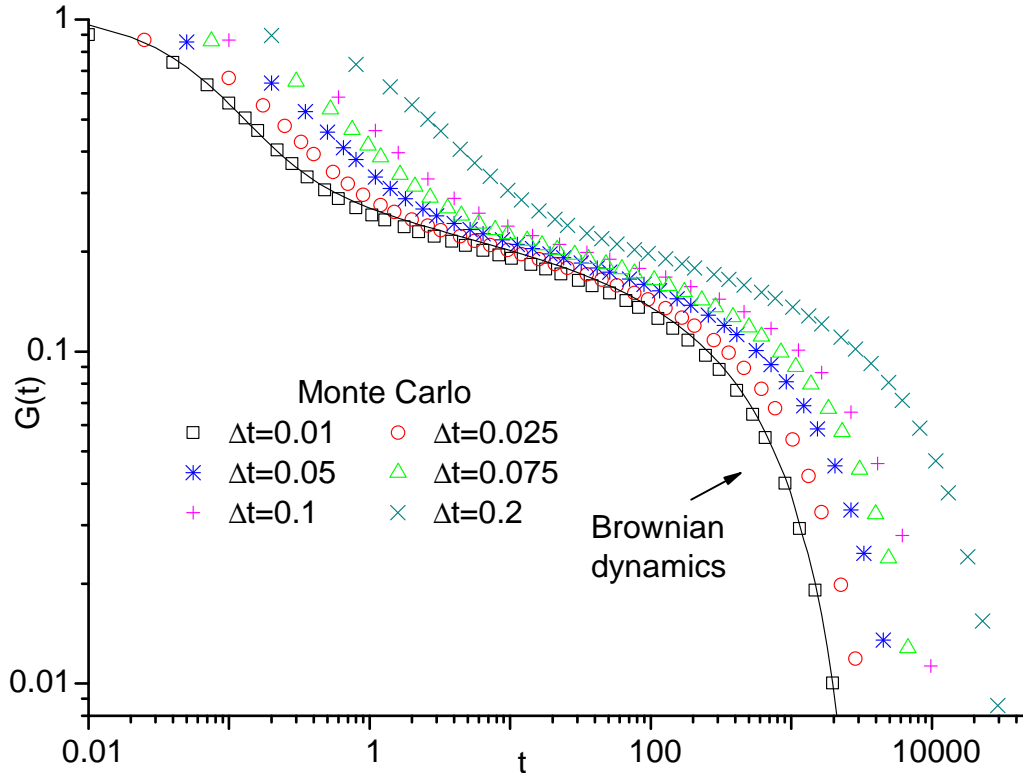


Figure A.1: The stress relaxation modulus, $G(t)$ from the Monte Carlo with $N = 32$, $g = 1$ and different sizes of the time step, Δt . The solid line and filled symbol (in the inset) are obtained from the Brownian dynamics simulation with the same parameters as in the Monte Carlo and $\Delta t = 0.01$.

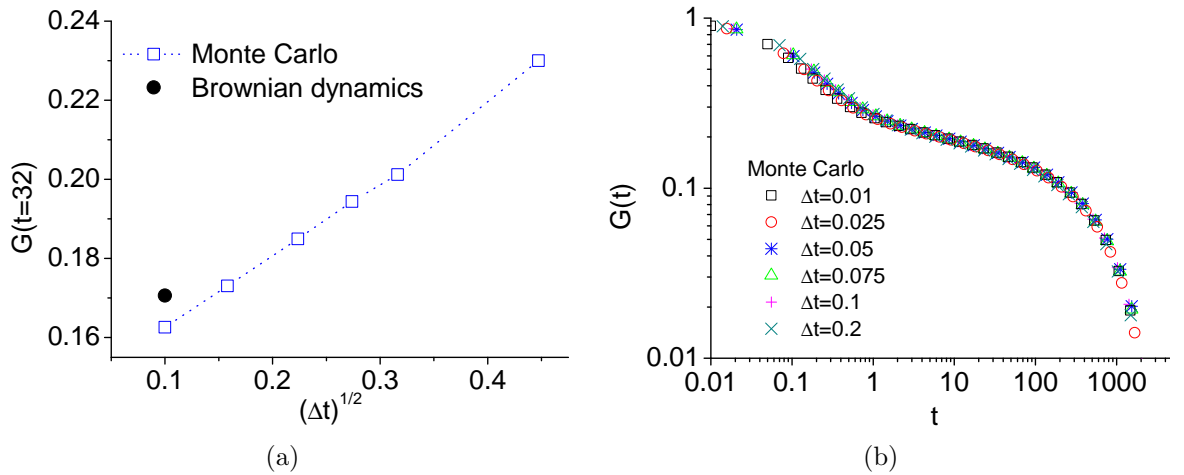


Figure A.2: The $G(t)$ at $t = 32$ from the Monte Carlo and Brownian dynamics with $N = 32$, $g' = 1$ as a function of $\sqrt{\Delta t}$ is shown in Fig. A.2(a). Fig. A.2(b) shows the horizontal shifted of the $G(t)$ in Fig. A.1 until they collapse upon each other.

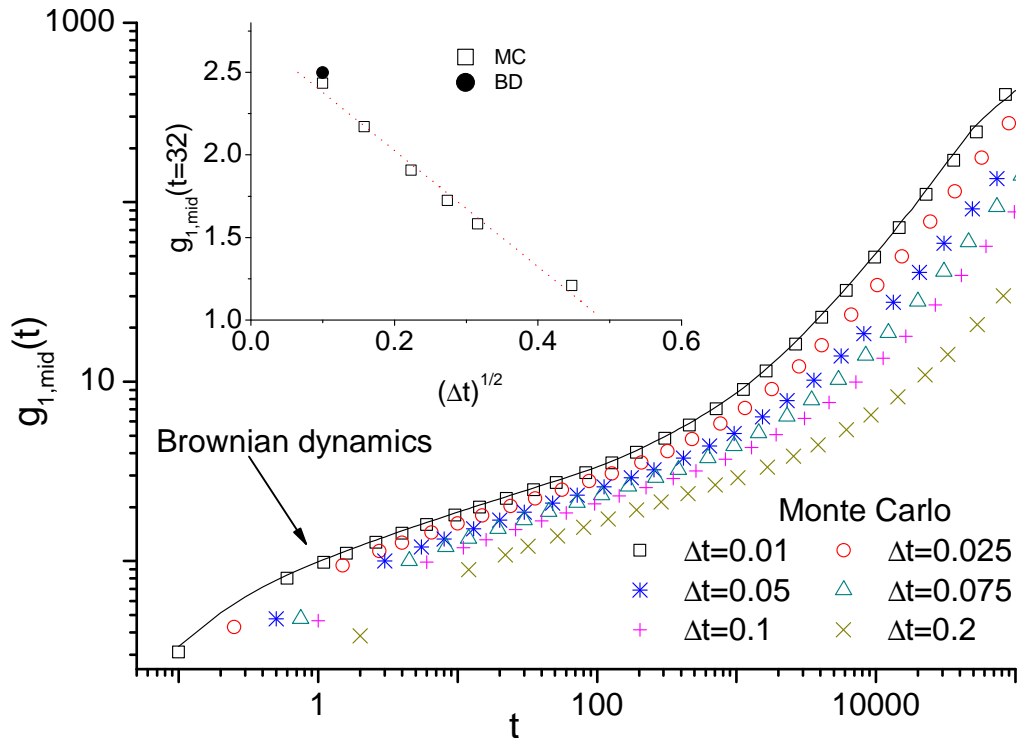


Figure A.3: The mean square displacement of the middle bead, $g_{1,\text{mid}}(t)$ from the MC simulation with $N = 32$, $g' = 1$ and different sizes of the time step, Δt . The inset presents the $g_{1,\text{mid}}(t)$ at $t = 32$ as a function of \sqrt{t} . The solid line and filled symbol (in the inset) are obtained from the Brownian dynamics simulation with the same parameters as in the Monte Carlo and $\Delta t = 0.01$.

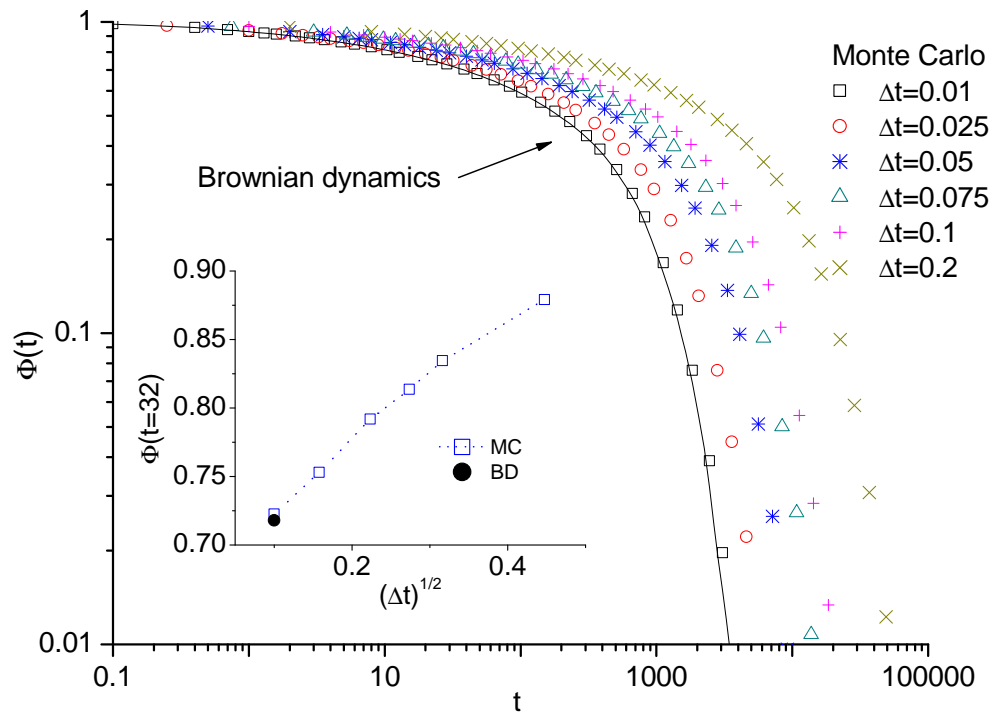


Figure A.4: The $\Phi(t)$ from the Monte Carlo with $N = 32$, $g' = 1$ and various time steps as indicated in the legend. The inset shows the $\Phi(t)$ at $t = 32$ over the Δt . The solid line and filled symbol (in the inset) are the data from the Brownian dynamics with the same parameters as in the Monte Carlo and $\Delta t = 0.01$

dynamics and efficiency of the system. Table A.1 presents the data obtained from the Monte Carlo with varying Δt . We begin with $\Delta t = 0.01$ and then increase it by 0.025 until $\Delta t = 0.1$. For comparison, we use the same input parameters for the Brownian dynamics with $\Delta t = 0.01$. Figs. A.1 and A.2(b) give a description about the values in Table A.1, such as the shift factor and how the observations change with time steps.

Table A.1: The efficiency analysis for the MC steps obtained from $N = 32$, $g' = 1$ and different sizes of the time step, Δt .

Δt	γ_{rej}	γ_{acc}	t_{eff}	Δt_{eff}	$S_{G(t)}$	$\Delta t \cdot S_{G(t)}$	$(\Delta t \cdot S_{G(t)})/t_{\text{eff}}$
0.01	41.6	58.4	1.971	0.0058	1.000	0.01	0.0051
0.025	57.3	42.7	1.850	0.0107	0.629	0.0157	0.0085
0.05	69.8	30.2	1.72	0.015	0.416	0.0213	0.0125
0.075	76.6	23.3	1.429	0.0175	0.276	0.0207	0.0145
0.1	81.1	18.9	1.362	0.019	0.192	0.0192	0.0141
0.2	89.8	10.2	1.199	0.02	0.072	0.0144	0.0120

Parameters of the analysis are:

1. Fraction of rejection γ_{rej} and fraction of attempted moves that are accepted of the Monte Carlo moves, $\gamma_{\text{acc}} = 1 - \gamma_{\text{rej}}$.
2. Efficiency of the computer simulations, t_{eff} , is the average time in micro seconds of the processor per particle to complete one simulation step. The t_{eff} is independent of the chain length.
3. Effective time steps denote as Δt_{eff} with $\Delta t_{\text{eff}} = \Delta t/\gamma_{\text{acc}}$ is the product of the time step and the fraction of acceptance ratio, where increasing the time steps makes the acceptance ratio decrease.
4. $S_{G(t)}$, is the time shift factor of $G(t)$ between data from the Monte Carlo and the Brownian dynamics.
5. $\Delta t \cdot S_{G(t)}$, is the relation between the time shift factor and the time step.

6. The $(\Delta t \cdot S_{G(t)})/t_{\text{eff}}$ is the effect of the shift factor and Δt towards the efficiency of the simulations.

As shown in Table A.1, all parameters change with time step. Increasing time step makes the percentage of acceptance rate decrease and efficiency of the system increase. The efficiency of the system increase with increasing Δt because the uncrossability algorithm require 3 steps of checking to accept the bead movement. However the movement is rejected if the algorithm failed in one of the cheks.

The larger time steps makes the Monte Carlo largely deviate from the Brownian dynamics simulation. The optimal time step that will be used in our Monte Carlo simulation is $\Delta t = 0.05$, because $\Delta t \cdot S_{G(t)}$ has a maximum there, meaning this time step provides most efficient simulations.

By using the optimal time step, we conducted comparison efficiency between the Brownian dynamics and Monte Carlo simulations. The analysis was conducted by running both simulations simultaneously and observing outputs of the simulations after specific real time running. The results are presented in Table A.2.

Table A.2: Comparison analyses of the MC and BD simulations for $N = 32$, $g' = 1$ with $\Delta t = 0.05$ and 0.01 , respectively. t_{eff} , is the efficiency of the simulation, t_{Sim} is the simulation time, τ_d is the disengagement time.

	unit time	BD	MC
Duration	real time	1 hour 51 minutes	1hour 51 minutes
Simulation running	simulation time	1.423e6	1.431e7
t_{eff}	computer time	1.432	0.7102
τ_d	simulation time	1239.08	3995.766
t_{Sim}/τ_d		1148.4	3581.29
$(t_{\text{Sim}}/\tau_d)\text{MC}/(t_{\text{Sim}}/\tau_d)\text{BD}$		1	3.11

The simulations of $N = 32$, $g' = 1$ with $\Delta t = 0.01$ and $t = 0.05$ for Brownian dynamics and Monte Carlo simulations, respectively, were run about 2 hours in real time on a similar computer with the processor Dual-Core AMD Optron @ 2.394 MHz. In Table A.2, the Monte Carlo was able to run up to 10 times longer (in

simulation time), more efficiency and was able to run approximately 3 times of its τ_d compared to the Brownian dynamics. As a result, we use the Monte Carlo steps simulation in the validation of our models and also for longer polymer chains.

Appendix B

Algorithm for tube mapping

The algorithm for tube mapping, involves:

1. The coordinate of vertices in the tube at its previous time step, \mathbf{V}^p is compared with the current tube, \mathbf{V}^c . The comparison is conducted by taking vertex i at tube $\mathbf{V}_i^p = \{\mathbf{V}_0^p, \dots, \mathbf{V}_{Z^p}^p\}$ and comparing it with all vertices in the current tube, $\mathbf{V}^c = \{\mathbf{V}_0^c, \dots, \mathbf{V}_{Z^c}^c\}$. Z^p and Z^c are the number of tube segments in the previous and current time steps, respectively. If the coordinate of vertex j of \mathbf{V}^c is the same with the coordinate of vertex i in \mathbf{V}^p then the index of vertex j is stored in array, $eS[i] = j$. $j = -1$ if no cell is found. This process is repeated until all vertices in \mathbf{V}^p are compared. The output in this step is $eS[i] = j_1, j_2, \dots, j_n$, $i = 1, \dots, Z^p$, where j_n is the number of indices in \mathbf{V}^c that is located in the same cell i in \mathbf{V}^p . For example, consider \mathbf{V}^p and \mathbf{V}^c as shown in Fig. B.1. After comparing all elements in \mathbf{V}^p then the $eS[i]$ is obtained as presented in Table B.1.
2. The array $eS[i]$ is analysed to determine the list of indices in \mathbf{V}^c that is mapped with \mathbf{V}^p . The ‘mapped’ element is defined as the relation between the index of \mathbf{V}^c with the index in \mathbf{V}^p where they are located in the same location. The

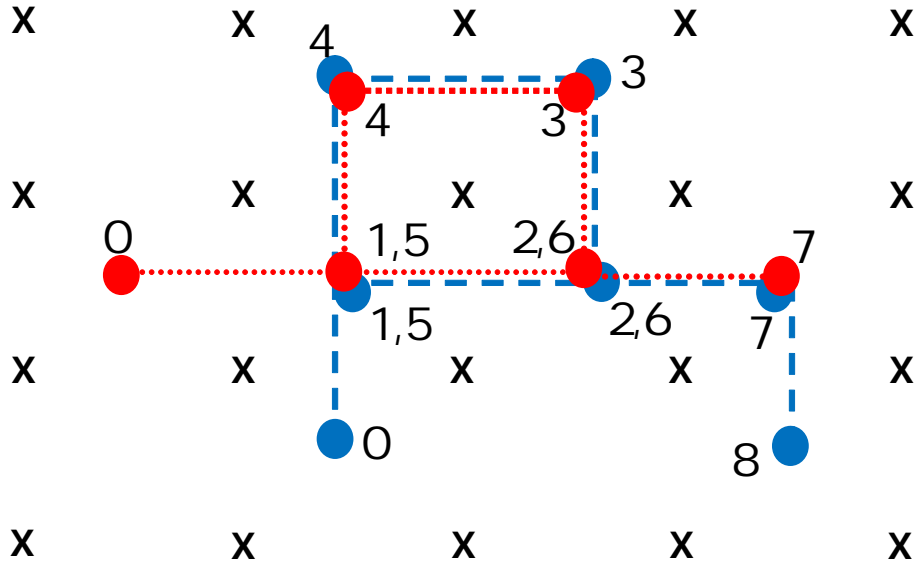


Figure B.1: Two dimensional view, the previous time step tube \mathbf{V}^p is denoted by a dotted line and the current tube \mathbf{V}^c by a dashed line. The circles show the index of cells for these tubes.

output from this analysis is stored in one dimensional array called $S[i]$. Firstly, in this procedure, the middle element of $eS[i]$ is determined. If $eS[\text{mid}] = j_1$ (only one integer, unique) then j_1 becomes a reference index. The middle element ($i = \text{mid}$) is selected because the middle cell moves slower than the end cells. Secondly, a sequence of integer (which represents the cell index) is constructed for $S[i]$. The construction of the sequence is by listing the

Table B.1: Elements of array eS , vertex 1, 2, 5 and 6. Consist two of tube's vertices are located in the same cell with the reference cell, i .

element array eS	mapped cell with \mathbf{V}^c
$eS[0]$	-1
$eS[1]$	1, 5
$eS[2]$	2, 6
$eS[3]$	3
$eS[4]$	4
$eS[5]$	1, 5
$eS[6]$	2, 6
$eS[7]$	7

smaller to the larger value than the reference index. The sequence in array $S[i]$ is used to determine which cells in \mathbf{V}^p are deleted or cells in tube \mathbf{V}^c are newly created. For example, referring to $eS[i]$ in Table B.1, the middle element $eS[4] = 4$ where $j_1 = 4$ (only has one value). The mapped sequence is constructed by using $j_1 = 4$ as a reference index as shown in Table B.2 (the integers are marked by the squared boxes). The sequence is stored in array $S[i]$ as shown in Table B.3.

Table B.2: List of indices

element array eS	mapped cell with \mathbf{V}^c
$eS[0]$	-1
$eS[1]$	1 , 5
$eS[2]$	2 , 6
$eS[3]$	3
$eS[4]$	4
$eS[5]$	1, 5
$eS[6]$	2, 6
$eS[7]$	7

Table B.3: The S of tube \mathbf{V}^p .

element array S	mapped cell with \mathbf{V}^c
$S[0]$	-1
$S[1]$	1
$S[3]$	3
$S[4]$	4
$S[5]$	5
$S[6]$	6
$S[7]$	7

3. If $eS[mid] = j_1, j_2, \dots$ (i.e., it is not unique in the middle element such as $eS[5] = 3, 7$ in Table B.4), then the next element in $eS[i]$ which have unique index is determined.

4. A validation is required for step 3 to ensure the correct sequence is obtained. This is conducted by comparing the content and the element index of array

$S[i]$, where $S[i] = j_i$. The difference is defined as $dj = |j_i - i|$ with $j_i \geq 0$. If $dj > 10$ in 3D or $dj > 6$ in 2D then step 5 is executed otherwise the procedure jumps to step 6. For example, \mathbf{V}^p and \mathbf{V}^c as in Fig. B.2 and its $eS[i]$ is shown in Table B.4. Only $eS[0] = j_1$ with $j_1 = 8$ (unique element) and the mapped element is shown in Table B.5. The series shows that cell 0 in \mathbf{V}^p has moved about 8 cells in one time step, $dj = 8$. As a result, the selected series is invalid.

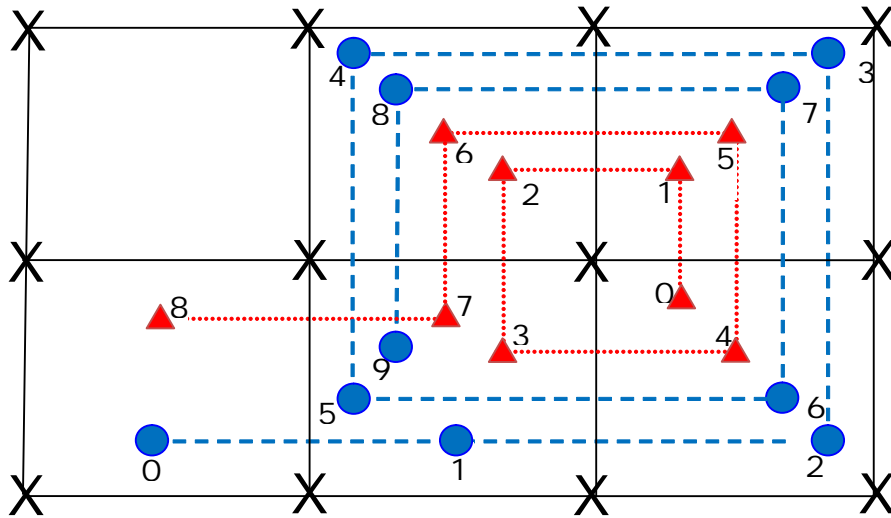


Figure B.2: Tube configuration, where the dashed line is the \mathbf{V}^p and dotted line is the \mathbf{V}^c .

Table B.4: Mapped element of tube \mathbf{V}^p with tube \mathbf{V}^c .

element array eS	mapped cell with \mathbf{V}^c
$eS[0]$	8
$eS[1]$	3, 7
$eS[2]$	0, 4
$eS[3]$	1, 5
$eS[4]$	2, 6
$eS[5]$	3, 7
$eS[6]$	0, 4
$eS[7]$	1, 5
$eS[8]$	6, 2
$eS[9]$	3, 7

5. By using each integer in the middle cell ($j_1 = 3$ and $j_2 = 7$, in the previous

Table B.5: Array S

element array S	mapped cell with \mathbf{V}^c
$S[0]$	8
$S[1]$	-1
$S[2]$	-1
$S[3]$	-1
$S[4]$	-1
$S[5]$	-1
$S[6]$	-1
$S[7]$	-1
$S[8]$	-1
$S[9]$	-1

example), the number of sequences are determined. The longest sequence is selected because the possibility for a large number of tube cells to disappear in one time step is likely. For example, as shown in \mathbf{V}^p and \mathbf{V}^c in Fig. B.2 and $eS[i]$ in Table B.4. The middle element is ‘mid= 5’. Thus, $eS[mid] = j_1$ and $eS[mid] = j_2$ with $j_1 = 3$ and $j_2 = 7$, respectively. The first series from $j_1 = 3$ gives 0, 1, 2, 3, 4, 5, 6 and the second series is 3, 4, 5, 6, 7. The longest series, which in this case is $j_1 = 3$ is saved in array $S[i]$.

Table B.6: Series of the mapped elements.

element array eS	mapped cell with \mathbf{V}^c
$eS[0]$	8
$eS[1]$	3,7
$eS[2]$	0 , 4
$eS[3]$	1 , 5
$eS[4]$	2 , 6
$eS[5]$	3 , 7
$eS[6]$	0, 4
$eS[7]$	1, 5
$eS[8]$	6 , 2
$eS[9]$	3, 7

6. Finally, the sequence in array $S[i]$ is analysed to determine the number of cells in \mathbf{V}^p to be added or deleted. The element in $S[i]$ which has a value of -1

means the cell in \mathbf{V}^p is removed. If $Z^c > Z^p$ then a new cell is added into \mathbf{V}^p .

B.0.1 Validation of the algorithm

The validation is conducted by observing the percentage of the types of obtaining the mapped segments. The parameters for validation as follows:

- **Middle Unique:** the unique element located in the middle cell of the tube.
- **Other Unique:** the unique element located in the other cells of the tube.
- **Longest:** no unique element found thus the selected series is based on the series which has the longest number of cells selected.
- **Equal:** when the series are equal length, then any of the series can be chosen.
- **Large Shift:** the tube has shifted a large number of cells at one time step.

Table B.7 present the percentage of some parameters listed above for $g = 1$ with various chain lengths. The analysis shows that the unique element that is located in the middle cell is the highest (about more than 80%). However, it decreases with the longer chains. This is caused by the higher probability of the chain to form entangled loops. This analysis shows our decision to use the middle cell as a reference cell in the mapping is acceptable.

Table B.7: Percentage of location the unique element of cells

Type	N=16	N=32	N=64	N=128
Middle unique	86%	79%	72%	69%
Other unique	14%	21%	28%	31%
Longest	0%	0%	0%	0%
Large shift	0%	0%	0%	0%

Bibliography

- [1] A. Grosberg and A. R. Khokhlov, *Giant molecules: here, there, and everywhere...* United States of America: Academic Press, 1997.
- [2] U. W. Gedde, *Polymer Physics*. Netherlands: Kluwer Academic Publishers, 1999.
- [3] K. Kremer and G. S. Grest, “Dynamics of entangled polymer melts: a molecular-dynamics simulation,” *J. Chem. Phys.*, vol. 92, no. 8, pp. 5057–5086, 1989.
- [4] A. E. Likhtman, “Single-chain slip-link model of entangled polymers: simultaneous description of Neutron Spin-Echo, rheology and diffusion,” *Macromolecules*, vol. 38, pp. 6128–6139, 2005.
- [5] A. Wischniewski, M. Monkenbusch, L. Willner, D. Richter, A. E. Likhtman, T. C. B. McLeish, and B. Farago, “Molecular observation of contour-length fluctuations limiting topological confinement in polymer melts,” *Phys. Rev. Lett.*, vol. 88, no. 5, pp. 058301–1, 2002.
- [6] B. A. Smith, E. T. Samulski, L. P. Yu, and M. A. Winnik, “Tube renewal versus reptation: polymer diffusion in molten poly(Propylene Oxide),” *Phys. Rev. Lett.*, vol. 52, no. 1, pp. 45–48, 1984.

- [7] R. S. Porter and J. F. Johnson, “The entanglement concept in polymer systems,” *Chem. Rev.*, vol. 29, no. 1, pp. 1–27, 1966.
- [8] N. Fatkullin and R. Kimmich, “Theory of field-gradient NMR diffusometry of polymer segment displacements in the tube-reptation model,” *Phys. Rev. E*, vol. 52, no. 3, pp. 3273–3276, 1995.
- [9] M. Doi and S. F. Edwards, *The theory of polymer dynamics*. Oxford, United Kingdom: Oxford University Press, 2007.
- [10] P. G. de Gennes, “Dynamics of entangled polymer solutions. I. the Rouse model,” *Macromolecules*, vol. 9, no. 4, pp. 587–593, 1976.
- [11] P. G. de Gennes, *Scaling concepts in polymer physics*. New York: Cornell University Press, 1979.
- [12] P. G. de Gennes, *Introduction to polymer dynamics*. Cambridge, Great Britain: Cambridge university press, 1990.
- [13] J. Ramírez, S. K. Sukumaran, and A. E. Likhtman, “Hierarchical modeling of entangled polymers,” *Macromol. Symp.*, vol. 126, pp. 094906,1–11, 2007.
- [14] A. E. Likhtman, “Whither tube theory: from believing to measuring,” *J. Non-Newton Fluid*, vol. 157, pp. 158–161, 2008.
- [15] S. K. Sukumaran and A. E. Likhtman, “Modeling entangled dynamics: comparison between stochastic single-chain and multichain models,” *Macromolecules*, vol. 42, pp. 4300–4309, 2009.
- [16] R. Evaraers, S. K. Sukumaran, G. S. Grest, C. Svaneborg, A. Sivasubramanian, and K. Kremer, “Rheology and microscopic topology of entangled polymer liquids,” *Science*, vol. 823, no. 303, pp. 823–826, 2004.

- [17] M. Kröger, “Shortest multiple disconnected path for the analysis of entanglements in two and three-dimensional polymeric systems,” *Comput. Phys. Commun.*, vol. 168, pp. 209–232, 2005.
- [18] S. Shanbhag and M. Kröger, “Primitive path networks generated by annealing and geometrical methods: insight into differences,” *Macromolecules*, vol. 40, pp. 2897–2903, 2007.
- [19] K. Foteinopoulou, N. Ch. Karayiannis, V. G. Mavrantzas, and M. Kröger, “Primitive path identification and entanglement statistics in polymer melts: results from direct topological analysis on atomic polyethylene models,” *Macromolecules*, vol. 39, pp. 4207–4216, 2006.
- [20] C. Baig and V. G. Mavrantzas, “From atomistic trajectories to primitive paths to tube models: linking atomistic simulations with the reptation theory of polymer dynamics,” *Soft Matter*, vol. 6, pp. 4603–4612, 2010.
- [21] C. Tzoumanekas and D. N. Theodorou, “Topological analysis of linear polymer melts: a statistical approach,” *Macromolecules*, vol. 39, no. 132, pp. 4592–4604, 2006.
- [22] F. Lahmar, C. Tzoumanekas, D. N. Theodorou, and B. Rousseau, “Onset of entanglements revisited. Dynamical analysis,” *Macromolecules*, vol. 42, pp. 7485–7494, 2009.
- [23] J. T. Padding and W. J. Briels, “Uncrossability constraints in mesoscopic polymer melt simulations: non-Rouse behavior of $C_{120}H_{242}$,” *J. Chem. Phys.*, vol. 115, no. 6, pp. 2846–2859, 2001.
- [24] J. T. Padding, *Computer simulation of entanglements in viscoelastic polymer melts*. PhD thesis, University of Twente, 2002.

- [25] S. P. Holleran and R. G. Larson, “Using spring repulsions to model entanglement interactions in Brownian dynamics simulations of bead-spring chains,” *Rheol. Acta*, vol. 47, pp. 3–17, 2008.
- [26] Z. Wang and R. G. Larson, “Constraint release in entangled binary blends of linear polymers: a molecular dynamics study,” *Macromolecules*, vol. 41, pp. 4945–4960, 2008.
- [27] S. Shanbhag and R. G. Larson, “Identification of topological constraints of entangled polymer melts using the bond-fluctuation model,” *Macromolecules*, vol. 39, no. 19, pp. 6737–6743, 2006.
- [28] J. des Cloizeaux and G. Jannink, *Polymers in solution: their modelling and structure*. Oxford, Great Britain: Oxford University Press, 1990.
- [29] G. R. Strobl, *The physics of Polymers: concepts of understanding their structures and behavior*. Berlin Germany: Springer-Verlag, 1996.
- [30] M. Rubinstein and R. H. Colby, *Polymer physics*. New York: Oxford University Press, 2003.
- [31] M. Doi, *Introduction to polymer physics*. Great Britain: Oxford University Press, 1996.
- [32] A. E. Likhtman, “Viscoelasticity and molecular rheology,” in *Polymer science: A comprehensive reference* (K. Matyjaszewski and M. Müller.(eds.), eds.), vol. 1, pp. 133–179, Amsterdam: Elsevier B.V., 2012.
- [33] P. E. Rouse, “A theory of the viscoelastic properties of dilute solutions of coiling polymers,” *J. Chem. Phys.*, vol. 21, no. 7, pp. 1272–1280, 1953.

- [34] W. Paul and G. D. Smith, "Structure and dynamics of amorphous polymers: computer simulations compared to experiment and theory," *Rep. Prog. Phys.*, vol. 67, pp. 1117–1185, 2004.
- [35] D. Ernst-Joachim, *Relaxation and thermodynamics in polymers: glass transition*. Berlin, Germany: Akademie Verlag, 1992.
- [36] A. N. Semenov, "Bond-vector correlation functions in dense polymer systems," *Macromolecules*, vol. 43, pp. 9139–9154, 2010.
- [37] Z. Wang, A. E. Likhtman, and R. G. Larson, "Segmental dynamics in entangled linear polymer melts," *Macromolecules*, vol. 45, pp. 3557–3570, 2012.
- [38] W. W. Graessley, "The entanglement concept in polymer rheology," *Adv. Polym. Sci.*, vol. 16, pp. 1–179, 1974.
- [39] W. W. Graessley, "Viscoelastic properties of entangled flexible polymers," *Faraday Symp Chem S*, vol. 18, pp. 7–27, 1983.
- [40] S. F. Edwards, "The statistical mechanics of polymerized material," *Proc. Phys. Soc.*, vol. 92, pp. 9–16, 1967.
- [41] M. Rubinstein and E. Helfand, "Statistics of the entanglement of polymers: concentration effects," *J. Chem. Phys.*, vol. 82, no. 5, pp. 2477–2843, 1985.
- [42] J. L. Viovy, M. Rubinstein, and R. H. Colby, "Constraint release in polymer melts: tube reorganization versus tube dilation," *Macromolecules*, vol. 24, pp. 3857–3896, 1991.
- [43] P. S. Stephanou, C. Baig, G. Tsolou, V. G. Mavrantzas, and M. Kröger, "Quantifying chain reptation in entangled polymer melts: topological and dynamical

- mapping of atomistic simulation results onto the tube model,” *J. Chem. Phys.*, vol. 123, pp. 124904(1)–124904(16), 2010.
- [44] H. Watanabe, “Viscoelasticity and dynamics of entangled polymers,” *Prog. Polym. Sci.*, vol. 24, pp. 1253–1403, 1999.
- [45] A. Likhtman and T. C. B. McLeish, “Quantitative theory for linear dynamics of linear entangled polymers,” *Macromolecules*, vol. 35, pp. 6332–6343, 2002.
- [46] M. Doi and N. Y. Kuzuu, “Rheology of star polymers in concentrated solutions and melts,” *J. Polym. Sci. Pol. Lett.*, vol. 18, no. 12, pp. 775–780, 1980.
- [47] S. Shanbhag and R. G. Larson, “Chain retraction potential in a fixed entanglement network,” *Phys. Rev. Lett.*, vol. 94, pp. 16001–1,4, 2005.
- [48] E. Helfand and D. S. Pearson, “Statistics of the entanglement of polymers: unentangled loops and primitive paths,” *J. Chem. Phys.*, vol. 79, no. 4, pp. 2054–2059, 1983.
- [49] E. A. Zheligovskaya, F. F. Ternovskii, and A. R. Khokhlov, “Random walks on a lattice of obstacles,” *Teoret. Mat. Fiz.*, vol. 7, pp. 644–653, 1988.
- [50] D. Frenkel and B. Smit, *Understanding molecular simulation, from algorithms to applications*. United States of America: Academic Press, Inc, 1996.
- [51] M. P. Allen and D. J. Tildesley, *Computer simulation of liquids*. Great Britain: Oxford University Press, 1989.
- [52] M. Müller and K. C. Daoulas, “Single-chain dynamics in a homogeneous melt and a lamellar microphase: a comparison between Smart Monte Carlo dynamics, slithering-snake dynamics, and slip-link dynamics,” *J. Chem. Phys.*, vol. 129, pp. 12906,1–18, 2008.

- [53] D. M. Heyes and A. C. Brańka, “Monte Carlo as Brownian dynamics,” *Mol. Phys.*, vol. 94, no. 3, pp. 447–454, 1998.
- [54] S. Kumar and R. G. Larson, “Brownian dynamics simulations of flexible polymers with spring-spring repulsions,” *J. Chem. Phys.*, vol. 114, no. 15, pp. 6937–6941, 2001.
- [55] P. M. Chaikin and T. C. Lubensky, *Prinsiples of condensed matter physics*. Cambridge, Great Britain: Cambridge University Press, 1995.
- [56] D. M. Heyes and A. C. Brańka, “More efficient Brownian dynamics algorithms,” *Mol. Phys.*, vol. 98, pp. 1949–1960, 2000.
- [57] A. C. Brańka and D. M. Heyes, “Algorithms for Brownian dynamics simulation,” *Phys. Rev. E*, vol. 58, no. 2, pp. 2611–2615, 1998.
- [58] A. C. Brańka and D. M. Heyes, “Algorithms for Brownian dynamics computer simulations: multivariable case,” *Phys. Rev. E*, vol. 60, no. 2, pp. 2381–2387, 1999.
- [59] L. E. Donald, “A computer simulation of charged particles in solution. I. technique and equilibrium properties,” *J. Chem. Phys.*, vol. 62, no. 10, pp. 4189–4196, 1975.
- [60] D. C. Lay, *Linear algebra and its applications*. United States of America: Pearson Addison Wesley, 2006.
- [61] S. F. Edwards and K. E. Evans, “Computer simulations of the dynamics of highly entangled polymers, part 1: equilibrium dynamics,” *J. Chem. Soc Farad. T 2*, vol. 77, no. 2, pp. 1981–1912, 1981.

- [62] S. F. Edwards and K. E. Evans, “Computer simulations of the dynamics of highly entangled polymers, part 2: static properties of the primitive chain,” *J. Chem. Soc Farad. T 2*, vol. 77, no. 2, pp. 1913–1927, 1981.
- [63] J. D. Ferry, *Viscoelastic properties of polymers*. United States of America: John Wiley & Sons, Inc., 1980.
- [64] K. Kremer, S. K. Sukumaran, R. Everaers, and G. S. Grest, “Entangled polymer systems,” *Comput. Phys. Commun.*, vol. 169, pp. 75–81, 2005.
- [65] C. Tzoumanekas, F. Lahmmar, B. Rousseau, and D. N. Theodorou, “Onset of entanglements revisited. Topological analysis,” *Macromolecules*, vol. 42, pp. 7474–7484, 2009.
- [66] Y. Masubuchi, T. Uneyama, H. Watanabe, G. Ianniruberto, F. Greco, and G. Marrucci, “Structure of entangled polymer network from primitive chain network simulations,” *J. Chem. Phys.*, vol. 132, pp. 134902,1–8, 2010.
- [67] Y. Masubuchi, J. Takimoto, and K. Koyama, “Brownian simulations of a network of reptating primitive chains,” *J. Chem. Phys.*, vol. 115, pp. 4387–4394, 2001.
- [68] T. Yaoita, T. Isaki, Y. Masubuchi, H. Watanabe, G. Ianniruberto, F. Greco, and G. Marrucci, “Statics, linear and nonlinear dynamics of entangled polystyrene melts simulated through the primitive chain network model,” *J. Chem. Phys.*, vol. 128, pp. 154901,1–11, 2008.
- [69] H. Guo, “A simple algorithm for fitting a Gaussian function DSP tips and tricks,” *IEEE Signal Proc Mag*, vol. 28, no. 5, pp. 134–137, 2011.

- [70] T. C. B. McLeish, “Tube theory of entangled polymer dynamics,” *Adv. Phys.*, vol. 51, no. 6, pp. 1379–1527, 2002.
- [71] A. Mehta, R. J. Needs, and D. J. Thouless, “A statistical theory of entangled lattice polymers,” *Europhys Lett.*, vol. 14, pp. 113–117, 1991.
- [72] A. E. Likhtman, “Monomer displacement in the tube model.” <http://www.personal.reading.ac.uk/~sms06a12>, 2011.
- [73] A. E. Likhtman and S. K. Sukumaran, “Comment on Entangled polymer melts: relation between plateau modulus and stress autocorrelation function,” *Macromolecules*, vol. 43, pp. 3980–3983, 2010.
- [74] G. Subramanian and S. Shanbhag, “On the relationship between two popular lattice models for polymer melts,” *J. Chem. Phys.*, vol. 129, pp. 144904,1–9, 2008.
- [75] M. Schulz, R. G. Winkler, and P. Reineker, “Reptation of polymer chains: a combined Monte Carlo and molecular-dynamics study,” *Phys. Rev. B*, vol. 48, no. 1, pp. 581–584, 1993.
- [76] J. Baschnagel, J. P. Wittmer, and H. Meyer, “Monte Carlo simulation of polymers: coarse-grained models,” in *Computational Soft Matter: from Synthetic Polymers to Protein* (N. Attig., K. Binder, H. Grubmüller, and K. Kremer, eds.), vol. 23, pp. 83–140, Jülich, Germany: John von Neumann Institute for Computing, 2004.
- [77] T. M. Beardsley, *The effect of polydispersity in diblock copolymer melts*. PhD thesis, The University of Reading, 2010.